Alma Mater Studiorum – Università di Bologna

DOTTORATO DI RICERCA IN

CHIMICA

Ciclo XXXI

Settore Concorsuale: 03/B1

Settore Scientifico Disciplinare: CHIM/03

DESIGN, SYNTHESIS AND CHARACTERIZATION OF NEW LUMINESCENT CRYSTALLINE MATERIALS

Presentata da: Chiara Cappuccino

Coordinatore Dottorato **Supervisore**

Prof. Aldo Roda **Prof.ssa Lucia Maini**

Esame finale anno 2019

TABLE OF CONTENTS

一聯の露りんりんと糸芒

Crystal beads

shining on the silver grass

looks fragile

Haiku by Kawabata Bosha

ABSTRACT

My PhD project was focused on the structural characterization of crystalline molecular materials and on the synthesis and structural determination of coordination polymers that are interesting for electronic and optoelectronic applications.

The reserch project could be divided in two main topics: (i) the structural and thermal characterization and the polymorph screening of a specific class of semiconducting organic materials: the 2,3-thienoimide (TI) based oligothiophenes; (ii) the synthesis and characterization of new luminescent coordination polymers based on d10 metal halides. The crystal structure determination was carrie out both by Single Crystal X-ray diffraction and Powder X-ray diffraction.

A great number of TBI derivates were studied, focusing the attention on the polymorph screening, thermal and, specially, structural characterization, since from information of packing it is possible to model the charge transport. It was discovered that this family of molecules possesses a well defined polymorphic behaviour, with two main type of molecular arrangements: one which present a columnar π-π stacking and a second which is characterized by a wafer-like structure. The wafer-like structure is characterized by the presence of a long axis and the molecules can adopt different dispositions generating several polymorphs. Herein, I present the case of NTA molecule which forms 5 different polymorphs with dramatic differences in the photophysical and conductive properties. Due to the intrinsic low crystallinity of these materials only two crystal structure were determined. Second project involved the Cn-NT4N molecules which present only two polymorphs and their structure was determined, one of them by XRPD. To confirm the molecular conformation for the structure determined by XRPD the powders were characterized by Raman spectroscopy which allowed unambiguous assignment of the molecular conformation.

These moelcues were also studied for devices application and I was involved in the determination of the polymorph in the device's active layers or on the thin-film deposition. It was discovered that the deposition technique could efficiently control the polymorphism, permitting to obtaining pure crystal phases and to tune the deposited crystal phase. Moreover, a new polymorph was detected and confirmed by Raman and UV spetroscopy.

In order to improve the crystallinity and the self-orientation of the crystal domains during the deposition I also investigated the effect of a strong external magnetic field during the crystal growth and deposition. The magnetic field improves the crystallinity and dimensions of the single crystals, and also can induce orientation of the crystallites during the deposition.

Part of my PhD reseach consisted in the synthesis and characterization of new luminescent coordination polymers (CP) based on Cu(I) and Ag(I) halides. The coordination polymers were obtained by solvothermal reaction, synthesis in solution and by direct grinding of the reagents. The mechanochemistry permits to perform the reaction directly in solid state, overcoming the intrinsic low solubility of Cu(I) and Ag(I) halides, and can yield crystal forms that are not obtainable in solution. Herein I reported the crystal structure of $[(CuI)_2(pyz)_2]_n$, an isomer of the published $[Cu_2I_2(pyz)]_n$, which can be obtain in absence of solvent. The stability and possibility of conversion among the three CPs of CuI and pyrazine ($[Cu_2I_2(pyz)]_n$, $[CuI(pyz)]_n$ and $[(CuI)_2(pyz)_2]_n$) is also described.

I explored the reactivity of the AgBr and AgI with the 2, 3 and 4 (aminomethyl)pyridine (hereafter pica). Most of the coordination polymers were obtained by direct contact of the powder with the liquid ligand and all the CPs are characterized by the same metal/ligan ratio (AgX:pica = 1:1), but in the case of AgBr with 3-pica and 4-pica it was possible to obtain by grinding CPs with two Silver atom for ligand (AgBr:Ligand = 2:1). The structure was determined for all the CPs and most of them present strong argentophilic interaction. The photophisical porperties of AgBr compounds are also reported.

LIST OF ABBREVIATIONS

TI: 2,3-Thienoimide

MCE: Molecular Crystal Engineering

SCXRD: Single-Crystal X-ray Diffraction

XRPD: Powder X-ray Diffraction

VT-XRPD: Variable Temperature Powder X-ray Diffraction

OLED: Organic Light-Emitting Diode

OLET: Organic Light-Emitting Transistor

OFET: Organic Field-Effect Transistor

OPV: Organic Photovoltaic Cell

TTI: Time-Temperature Integrator

TGA: Thermogravimetric Analysis

DSC: Differential Scanning Calorimetry

HSM: Hot-Stage Microscopy

DFT: Density Functional theory

CP: Coordination Polymer

pyz: pirazine

4CN-py: 4-cyanopyridine

CSD: Crystal Structural database

DABCO: 1,4-Diazabicyclo[2.2.2]octane

MeCN: acetonitrile

npica: n-picolylamine [(n-aminomethyl)pyridine]

CHAPTER 1: INTRODUCTION

CRYSTAL STRUCTURE RESOLUTION

The core of crystallography and crystal engineering is the determination of the crystal structure of new compounds, solid-state chemists know how important is the crystal structure for a complete knowledge of the chemical and photophysical properties. Knowing the importance of this data, the experimental techniques and the computational algorithms dedicated to the structural resolution of crystals are improving constantly.

This odyssey has been started in 1913 with the contribution of Bragg, that in his paper showed how to solve the crystal structure of NaCl-type crystals and diamond from single crystal data.[1] From that point, the single crystal X-ray diffraction technique (SCXRD) remains the main method for crystallographers to determine the position of atoms inside a crystal. Only three years later, Debye and Scherrer developed X-ray powder diffraction technique (PXRD)[2], and even if from the beginning it was used for the structural resolution (Debye and Sherrer solved the structure of LiF and silicon in the 1916[2] and graphite in the 1917[3]) its use was almost entirely dedicated to qualitative and semi-quantitative phase analysis for more than 50 years.

The reason for the resilience in the diffusion and improvement of structure determination from powder could be found in some intrinsic problems that affect the powder diffraction. The diffraction pattern from polycrystalline materials can be described as one-dimensional projection of three-dimensional diffraction data, this could imply a complete or partial overlap of some diffraction peaks, hence a loss of information on the position (i.e. the 2θ value) and the intensity of each peak in the powder XRD pattern. Some improvement can be achieved by collecting “high-resolution” PXRD pattern, thanks to synchrotron facilities available for scientists; however, while peak overlap may be reduced by appropriate optimization of experimental conditions, it will never completely be eliminated.[4]

The necessity to developed and improve the potential of XRPD arises from some key points that can not be found in the SCXRD and that demonstrate the power of the powder diffraction as a tool for the structural resolution. First is important to underline that the SCXRD does not provide information of the bulk material, the single crystals chosen for the analysis normally are the biggest and the most perfect crystals of the sample but not always the most representatives. Furthermore, the SCXRD is not a routine technique and in many cases is not always available. Another strength of XRPD is the fast data acquisition, especially *via* synchrotron, that permits to follow the variation in the structural parameters during a transformation or a solid-state reaction, or for studies *in situ* of materials under certain condition.

A big challenge in the use of powder diffraction resolution is doing it from lab diffraction data. Poor quality diffraction patterns are characterized by low intensity of the diffraction peaks and often a visible broadening that increases the effect of the peak overlap. The effect is very important for large crystalline cells and low symmetry systems, such as most molecular solids, whose diffractograms are characterized by a high density of peaks in the powder pattern that makes the peak overlap particularly problematic.

The nature of microcrystalline powders can be described as a myriad of small crystals, ideally with random orientation. Because of the randomly oriented nature of the crystallites within the powder the lattices of every crystal domains possess a different orientation, this means that the diffracted signal comprises a set of coaxial cones of diffracted radiation (called Debye-Scherrer cones) that appear as circle on a 2D detector; in contrast to the typical SCXRD patterns constitute by sharp beams of diffracted radiation (figure 1).

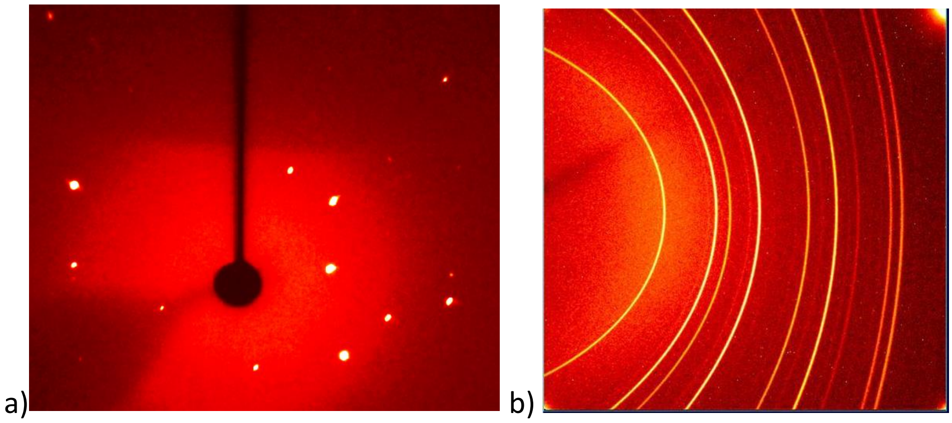

Figure 1. difference between a diffraction pattern of a single crystal (a) and a polycrystalline sample (b) by single crystal x-ray diffraction

For SCXRD it is known that the positions of the spots are determined by the size and shape of the unit cell and the symmetry while the intensities of the spots are determined by the arrangement of the atoms within the crystal. The intensity is proportional to "Structure Factor" F(hkl), a quantity that contains all the information about the position of the atoms and is described by a module |F(hkl)| (the real part) and a phase ϕ(hkl) (the imaginary part). Unfortunately, all the information about phase are lost in the process of recording the diffraction pattern and since the measured intensities are proportional to the square of the structure factor.

$$I(hkl) \propto |F(hkl)|^2$$

The consequence is the "Phase Problem", which does not allow the direct calculation of the electron density form the diffraction pattern.

However, the possibility to know position and intensity of a large number of peaks permits to overcome the phase problem and permits to solve the structure from the reciprocal space. The first method developed is the Patterson method: it uses a function that considers the square of the structure factor in order to identify not the atomic position but the interatomic vectors; it can be used only in presence of heavy atoms. The direct methods, instead, that are based on the estimation of the phase directly from the structure factor magnitude using a probabilistic approach and do not need the presence of a heavy atom. The Charge-Flipping method[5] is also called *dual-space algorithm* and it uses alternating modifications in direct and reciprocal space to find a solution to the phase problem.

The methods developed for the structure determination form single crystal X-ray diffraction can rarely be used for the powder X-ray diffraction because the intensities of the peaks are extracted with difficulties.

The typical process for a structural solution of an unknown structure from powder data consists of a series of steps, which are not always easy to overcome and require information about the geometry of the molecule. A generic scheme of the resolution path follows these steps:

(1) Indexing of the powder pattern and the determination of the unit cell
(2) Profile refinement
(3) Structure solution
(4) Structure refinement

The first step of the solution of an unknown structure is always the indexing of the powder pattern, that is the crystal cell parameters of the unit cell is determined, which is followed by the determination of the space group. It is a crucial step during the structural resolution and required the utmost attention in order to avoid the association of the wrong space group, a mistake that makes impossible to find the correct crystalline structure. The position of each peak is correlated to the interplanar distance thanks to the equation (derived from the Bragg law):

$$Q_{obs} = \frac{1}{d^2} = \left[\frac{2sen\theta}{\lambda}\right]^2$$

(where Q_{obs} is a parameter derived to the experimental peak position), and it means that is necessary to use a list of position as accurate as possible.

A wide range of different computational algorithms have been developed for the indexing procedure, some of the most used are: ITO[6], DICVOL[7], TREOR[8], MCMAILLE[9], SVD[10]. The reliability of the cell is given by the figure of merit and by the cell volume. In fact, it is expected that the volume of the correct cell is a multiple of the molecular volume of the species to be determined. The next step is the extraction of the peak intensities that is fundamental for the determination of the amplitudes of the structure factors |F(hkl)|. The most modern procedures, called “Whole Powder Profile Fitting” (WPPF), consider each peak position strictly constrained to the cell parameters and create a model of the entire powder pattern; subsequently the model’s parameters are optimized using specific mathematical algorithms. The WPPF techniques used for the profile refinement are the Pawley[11] and Le Bail[12] methods. These methods are called cell-restrained WPPF, because each peak position is strictly calculated from the chosen crystal cell: the Pawley method consists in a least square refinement of the individual intensities for every Bragg peak through the use of a generic Intensity vector $\mathbf{I}=(I_1, I_2, \ldots I_N)$ for N reflexes; in Le Bail method the intensities are calculated from an arbitrary value, obtained *via* a mathematical function, that in any new cycle is re-injected in the function in an iterative process, while the crystal cell, the peak shape and instrumental parameters are refined by a least-squares procedure.

In the case of PXRD the quantity of information is less than in the case of SCXRD and this makes difficult the use of the reciprocal space and the Direct methods. There were developed some other methods focused on the direct space instead of the reciprocal space. The aim of these procedures is to fit the complete experimental powder XRD pattern *via* the refinement of the variables associated to: (i) the peak positions (include the unit cell parameters, the zero-point error and, eventually, the specimen displacement), (ii) the background, (iii) the peak widths, (iv) the peak shapes and (v) the peak intensities. The peak shape is an indication of different characteristic of the sample both instrumental and real-sample, Furthermore, the profile refinement permits to validate the choice of the space group, as it allows to highlight anomalies in the overlap of the peaks which could derive from systematic absences related to particular symmetry elements. Once the refinement is acceptable it is possible to proceed to the structure solution.[13]

Techniques for structure solution from powder XRD data can be subdivided into two categories: the *ab initio* and the direct-space strategies. The *ab initio* methods are those developed for single-crystal XRD data and they require the extraction of the diffracted intensities to reconstruct the amplitude of the structure factors |F(hkl)|. The intensities extraction could be unreliable due to the peak overlap, especially in the case of large unit cells and/or low symmetry (for which the extent of peak overlap is extensive); it makes the *ab initio* methods to be rarely used, even if the are the only strategy in those case it isn't possible to hypothesize a reasonable structural model (such as in the inorganic compounds) and the diffractogram is the only information available.

In contrast, the direct-space strategies do not require the powder XRD pattern decomposition and they use a global optimization procedure to determine the best orientation and location of a given structural model. For this reason, it can be used only if information about the molecular geometry or the connectivity of atoms is available, that is for organic or organometallic compounds. The starting structural model, chemically reasonable, is described by the internal coordinates (bond lengths, angles and torsional) in the form of a Z-Matrix. The model is moved in the direct space and its diffraction pattern is calculated. This strategy uses a large number of trial crystal structure generated by computational procedures and the powder pattern for each trial structure is overlapped to the experimental pattern in an iterative process designed to minimize differences between the two diffractograms, the goodness of the overlap is described by the "Cost Function". The aim of the procedure is finding the trial structure associated with the lowest cost function, that corresponds to the best overlap between the calculated and the experimental diffraction pattern. Grid search, Monte Carlo, simulated annealing and genetic algorithms are the search methods most commonly used for this purpose.[14]

One of the most important contributions in the development of the modern methods for the XRPD structural solution was introduced by Rietveld in the 1969.[15] He proposed a new method for analyzing complex patterns characterized by low symmetry using a curve fitting procedure. It is a least-square refinement directed to minimize the differences between the observed and calculated profile to refine the crystalline structure, exploiting the reverse procedure of calculating the diffraction pattern from a given crystal structure by the position of the atoms in the crystal cell .[16]

Unlike the Pawley and Le Bail techniques in the pure Rietveld method the intensity of the diffraction is not a parameter to refine, but it is calculated, based on the position and the structure factor of the atoms present in the crystal cell. Usually the refinement process starts with a Pawley or Le Bail procedure for the optimization of instrumental and crystallographic parametrs, followed by a Rietveld refinemet dedicated to the improvement of the structural model.

The initial model proposed by Rietveld describes the diffraction pattern as a simple combination of common functions: a gaussian for the peak shape and a polynomial for the background. The evolution and the development of new diffraction techniques and the necessity of analyse complex structure necessitated to implement new and more elaborate functions. The more modern models include instrumental (axial divergence, tube tails, anisotropic peak shape) and sample-related (preferred orientation, sample tit, crystal size) factors, in order to adapt the technique to a large number of geometries and different type of radiations.

The Rietveld method established the foundations for the development of also other procedures, dedicated to the extraction of information from the powder diffractograms, like the model for the calculation of the relative percentage by weight of different phases in a mixture[17], or the microstructural and texture characterization.

It is clear how crucial is the powder diffraction for the characterization of materials, and thanks to the fast improvement in the instrumentation, methods, data analysis and modeling become more widespread and powerful. Certainly, Dr. Hugo Rietveld gave one of the most important and more effective contributions to the modern crystallography; to this day, almost fifty years after its original formulation, the technique that bears his name remains the most used and powerful instrument in the analysis of the powder diffraction data.

ORGANIC SEMICONDUCTORS

The growing demand for increasingly efficient and performing semiconductor materials has led to a considerable increase in scientific research dedicated to the production and optimization of new compounds. Most of the semiconductor technology is based on inorganic materials, especially the silicon that remains the most widely used in electronic devices thanks to the combination of cost, performance and stability. These aspects make it currently the best compromise among the various competing materials. Nowadays the evolution of the technology requires materials with increasing performances, often unreachable by the most common and widely used semiconductors. The performances achievable from silicon are reaching an unsurpassable physical limit[18,19] and for this reason the attention of the research has gradually shifted towards different options.

With the synthesis of the first fully organic semiconductor, the polyacetylene, by Shirakawa et al. in 1977[20], it was demonstrated that even molecular materials could act as active layer in electronic devices. This discovery established the starting point of a new research topic that continues to evolve and draw the attention of the scientific community, and, it has experienced an extraordinary development thanks to the improvement in the synthesis methods and analytical techniques.

At present, it may be too early to consider organic semiconductors as competitors to silicon in terms of sheer performance, but even if transport efficiency is usually less favorable than their silicon counterparts[21], there are some other advantages:

- they could be more easily made (and therefore are less expensive);
- they could be highly flexible;
- it is easier to tune their properties (such as band gap or fluorescence) by modifying their chemical structure and/or the crystal packing;
- thanks to the low-temperature solution processing, it is possible to expand the repertoire of accessible substrates and processing options, allowing flexible plastics or fabrics to be used in conjunction with methods such as spin coating, stamping, or inkjet printing.[22–24]

For these reasons, the organic semiconductors have become widely used in the optoelectronic, and the preparation of OLEDs (Organic Light-Emitting Diodes) is now relatively common and widespread; other technologies are experiencing great development, like light emitting transistors (OLETs), photovoltaic cells (OPVs) and organic field-effect transistors (OFETs). OFETs are devices consisting of an organic semiconducting layer, a gate insulator layer and three terminals (drain, source and gate electrodes).[25] As normal transistor is now the fundamental building block of any electronic devices, the OFETs could be in the future the base for the next generation of organic circuits and this is the reason of the increasing interest in this research field.[26] The OLET is obtained combining the switching function of a transistor with the light emission capability, this is a new kind of transistor device that from a single electrical input can create two output (one electrical and one optical). OPVs utilize the photoelectrical effect of organic semiconductors to convert light in electricity; at the present the most common organic photovoltaic cells are based on polymer, but a recent development of hybrid organic-inorganic perovskites for photovoltaic applications has attracted extensive attention.[27,28]

In classical inorganic semiconductors such as silicon, atoms are held together with strong covalent forming a highly crystalline three-dimensional solid, with the result of a strong overlapping of the atomic orbitals. This strong interaction permits the charge transport in highly delocalized bands that is mainly limited by defects, lattice vibrations, or phonon scattering in the solid. In contrast, organic semiconductors are composed of individual molecules that are only weakly bound together through van der Waals, hydrogen-bonding, and π-π interactions and typically produce disordered, polycrystalline films that possess discrete ‘‘energy levels’’, consisting of molecular orbitals. Charge transport depends on the ability of the charge carriers to pass from one molecule to another, therefore, charge transport in organic materials is thought to rely on charge hopping from these localized states.[21] This is closely related to bonding orbitals and quantum mechanical wavefunction overlap, namely, the energy levels of the highest occupied molecular orbital (HOMO), the lowest unoccupied molecular orbital (LUMO) and the energy band gap between the HOMO and LUMO energy levels (ΔEg).

Among all organic molecules the conjugated systems have proved to be the best candidate for semiconducting applications. The unique electronic properties or conjugated molecules originate from a system of π-electrons extended over a large number of sp^2 carbons. The charge transfers in organic semiconductors, the hole transport takes place in the HOMO, which is formed by overlapping molecular π-orbitals, therefore it acts like the valence bond of the inorganic semiconductors. Similarly, the electron transport results from the overlap between anti-bonding π-orbitals (π*) and occurs in the LUMO, thus corresponds to the conductive band of inorganic semiconductors. So, the energy required to pump an electron from the HOMO to the LUMO (ΔEg) is analogous to the valence-conduction band gap in an inorganic semiconductor.[29,30] In the case of conjugated systems a higher delocalization of the π-electrons means a progressive closure of the HOMO-LUMO gap, improving the semiconductive properties. The value of the energy gap can be also modulated by appropriate functionalization of the conjugated backbone, with the inclusion of appropriate electron donating and electron withdrawing substituents.

However, the conjugated organic molecules usually act as excellent hole-transport (p-type) semiconductors whereas electron transporting (n-type) organic semiconductors are rarer and, in general, still lag behind p-type organic semiconductors in terms of carrier mobility and air stability.[31] An ideal n-type semiconductor required that its LUMO energy level is close to the work function of the drain and source electrodes, in this way electrons can easily inject from the source into the organic layer and flow out of the semiconductor to the drain electrode efficiently. However, the work function of the most common electrode materials (like Au and Pt) is very high and is more suitable for the injection of holes into the HOMO rather than electrons into the LUMO of the organic semiconductor. In order to match the energy of the LUMO of the organic material with the work function of the electrode, it is possible to include electron withdrawing groups in the conjugated core, such as halogen, cyano or carbonyl.

The molecular tailoring also permits to design and synthesized innovative materials that could act both as p-type and n-type semiconductors, the ambipolar semiconductors, implementing n-type charge transport moieties inside a p-type conjugated material. The possibility to obtain both p- and n-channel efficient materials are required in the fabrication of new logic circuits and solar cell.

To achieve acceptable performance, organic semiconductors must satisfy also some criteria related to the structure and the mutual orientation of the individual molecules, and that is why the crystallography and solid state characterization has an important role in this field.

Since the HOMO and LUMO energies are perturbated by the packing in the solid, it is important to have a crystal structure that provides a good overlap of the frontier orbitals.

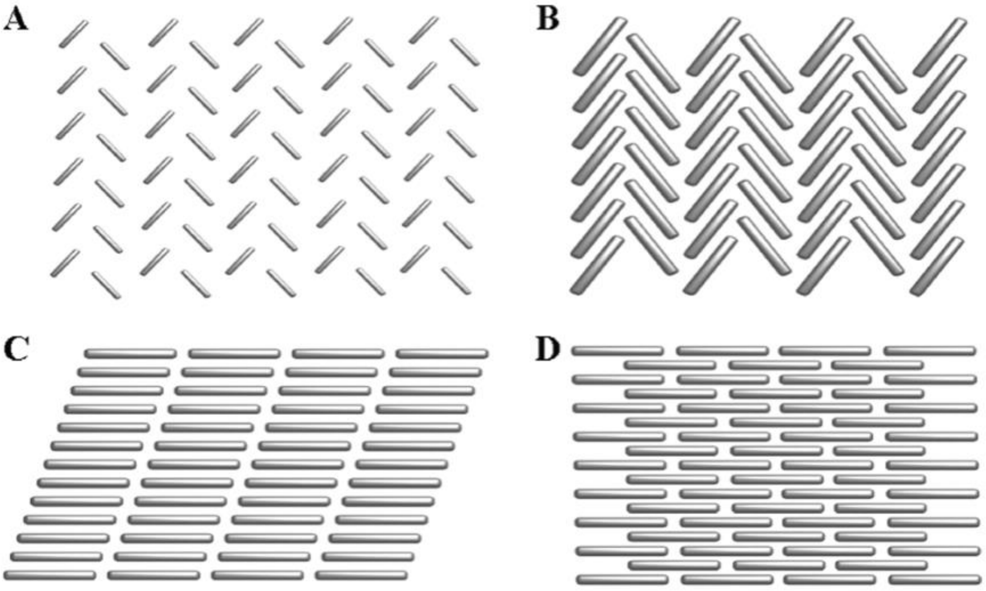

Figure 2. Typical crystal packings in organic crystalline semiconductors: A) Herringbone without π-π overlap; B) Herringbone with π-π overlap; C) Lamellar motif with 1-D π-π stacking; D) Lamellar motif with 2-D π-π stacking (courtesy of the paper, Chem. Rev. 2012, 12, 2208).

In the figure 2 are represent the most relevant molecular packing motifs for semiconductors, divided in four main groups: (A) the herringbone packing without π-π overlap (face-to-face) between adjacent molecules (for example, pentacene[32]); (B) herringbone packing with π-π overlap between adjacent molecules (for example, rubrene[33]); (C) lamellar packing with one dimensional (1D) π-π stacking (example: hexyl substituted naphtalene diimide[34]); (D) lamellar packing with two dimensional (2D) π-π stacking (example: PDIF-CN_2[35]). Theoretically the packing motifs that increase the π-π stacking are considered the most efficient for transporting charge carriers, as they allow delocalization of the π-electrons across all the aligned π-orbitals of the molecules, incrementing the charge transport (that occurs along the direction of the intermolecular π-π stacking) that occurs through an almost straight line (the shortest route possible). In order to increase a good π-π stacking is also important to have the molecular conjugated backbone as planar as possible, a feature typical of aromatic molecules.[36]

The molecular packing is the result of the minimization of lattice energy through the cooperative effect of π-π stacking, electrostatic interactions, dispersion interaction and others; and it is well known that the molecular compound can reach different relative minima, hence it crystallizes as different polymorphs. The control of the different polymorphs can be achieved by the crystallization technique, while the packing can be designed by crystal engineering.

In conclusion, the research on organic semiconductors has grown exponentially in the last decades, reveling that the organic semiconductors represent a powerful competitor for the next generation of electronic devices. However, some key challenges for further advancement remain, the low mobility and stability of organic semiconductors, the lack of deep knowledge regarding structure-property relationships. For the last point, the theoretical model requires the knowledge of the crystal structure to provide basic information between packing arrangement and charge transport mechanism.[26]

2,3-thienoimide (TI) based oligothiophenes

Among all the possible organic molecules interesting for semiconducting applications, aromatic compounds, specially acenes[37], have a highly extended and dislocated π-system, and possess some of the highest mobility achievable by organic semiconductors.[26,36] Polymers and oligomers based on thiophene rings are remarkable representatives of aromatic semiconductors, and in fact, the first material used in an OFETs device was the polythiophene.[38,39] The success of the sulphur-containing heterocyclic semiconductors is due to some particular features of these materials. The thiophene possesses a high aromaticity, similar to the ones of the benzene, and a high planarity of the aromatic core, plus, the introduction of heteroatoms induced a higher stability, due to the absence of a Diels-Alder cyclization center.[40] Finally, the presence of the S atoms could induce more intermolecular interactions (like S···S, S···H and S···π) that can be exploited to modulate the crystal packing.[41–43]

Among the recently emerged building blocks, the electron deficient 2,3-thienoimide group is gaining increasing attention due to the promotion of n-type and ambipolar charge transport properties in the resulting N-ended oligomers, like oligothiophene; in fact, the conjugated thiophenic core permits the p-type semiconduction, while the thieno-imide moiety permits the n-type charge transport.[44]

Thienopyrrolyl dione end-capped oligothiophene, for simplicity thienoimide (TI) based oligothiophenes, (NTxN, where x=number of thiophene rings) (figure 3) displayed ambipolar charge transport with major n-type behavior combined in most cases to electro-luminescence[45–48], making these materials potential candidates to realize field effect transistors (OFETs)[45,49] and single layer ambipolar light emitting transistor devices (OLETs).[46]

Due to its peculiar electron deficient feature, the thienoimide group strongly influences also the optoelectronic properties of the final oligomers, also because could influence molecular conformation and solid state packing, properties that are intimately related to optical and charge transport functionalities as well as to the final device performances.

The ambipolar charge transport, characterized by high n-type mobilities, combined with electroluminescence make TI materials an exceptional case of studies for the innovative design of multifunctional semiconductors.

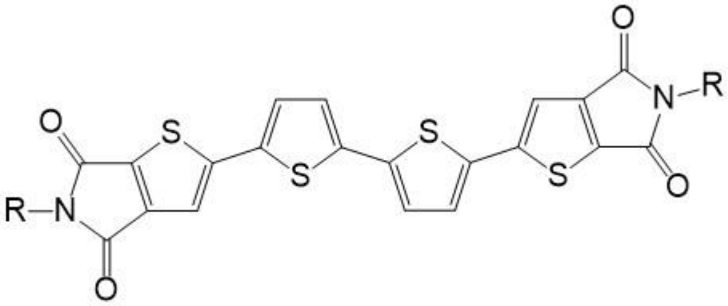

Figure 3. Generic molecular structure of a TI based oligothiophenes

Thanks to the presence of the functionalizable pirrolidine, it is possible to insert suitable moieties, like alkyl or heteroalkyl chains, in order to increase the solubility and so, to make the molecule appropriate for deposition methods from solution. It was also observed that the end substitution of the conjugated core is accompanied by a modification in the solid-state organization and a variation on the charge transport ability.[50] The role of the chain has been extensively studied, molecules with linear, branched, or asymmetric chain have been synthesized[50], as well as molecules with a different number of thiophene rings[45] or with a different bridge between oligothiophene rings.[48] The crystal structures were determined only for a small number of molecules which do not allow a comprehensive study on these compounds. However, some common behaviors have been found, which enable some general consideration.

It was observed that in the crystal state they commonly adopt a slipped π-π stacking packing mode, instead of the herringbone structure that is more common for oligothiophenes.[51,52] This result is probably due to the presence of the thienopyrrollyl-dione function, which, for steric effect, drive the molecules to a more coherent and compact piling; which results in a closer intermolecular packing distance. Furthermore, these molecules have the attitude to crystallize in different crystal forms and usually present a liquid crystal state at high temperature.

The structural study on the polymorphism of 2,3-thienoimide (TI) based oligothiophenes brought to the classification of two main groups of crystal forms:

- Form A, in which the molecules are piled in columnar stack and each aromatic core strongly interacts through π- π stacking interactions with one molecule of the upper and lower layers. The interdigitation of these columns is favored by the presence of C–H···O intermolecular interactions occurring between the thienoimide oxygen and one hydrogen of the alkyl layer of an adjacent molecule.
- Form B, in which each molecule interacts with four differrent close molecules (two below and two above), creating a bidimensional π- π stacking. In this motif it can be observed a lower degree of interdigitation of the alkyl chain, and the structure can be described as a wafer with layers containing only the aromatic cores and layers containing only the alkyl chains. It worth noting that this molecular arrangement allows small difference in the disposition of the molecules, without a substantially change of the crystal packing.

It was observed that the sulfur atoms of the thiophene and thienimide rings can display the *anti*, as well as the *syn* conformation, while the thiophene rings are always in *anti* conformation. Further studies discovered that, in the case of NT4N, form A and Form B are related with the number of the carbon atoms of the terminal alkyl chains: odd chain ended C3- and C5-NT4N display exclusively the *syn–anti–syn* conformation and B-type packing only, while end-chains with an even number of atoms could form both phase A and phase B.[53]

It was observed that, form A is characterized by the presence of alkyl chain almost perpendicular to the aromatic core, no long cell axes and close packing, while form B is identified by the presence of a long cell axis due to the elongation of the molecules next to each other; which allows a certain degree of freedom. In fact, the molecule can assume various conformation or orientations, with the possibility to generate polymorphs with a quite similar packing. For example, non-planar aromatic core or herringbone packing motif can be easily described within the form B family.

In most of the cases, the polymorphism is associated with visible differences in the photophysical and charge transport properties. The possibility to exploit different properties from a single molecule could be an interesting way for the creation of new devices that required a different type of response in different conditions. An example could be the TTI devices (time temperature integrator), devices that are capable to record the thermal history of a system, an essential feature for the control and the storage of perishable products.[54–58] A TTI based on a polymorphic compound could exploit a thermal polymorph transition between two crystal forms with different colour or emission.[59]

As it is well known the charge transport ability is highly dependent on the molecular packing, and it means that different molecular packing could possess different conducibility, such as the rubrene .[60,61] In this case is necessary to understand all the relationship between the different crystal forms and find a way to obtain the pure desired crystal phase.

Since the synthesis of these new molecules was focused for the preparation of new materials for innovative electronic devices, most of the compounds were also tested as active layers in thin film devices for electronic and optoelectronic application.

C4-NT4N and C6-NT4N have been deposited with different techniques and it has been found that the deposition process has a great influence on the molecular packing and crystal morphology and could permit to control the formation of different crystal forms, in order to tune the photophysical and conduction properties. Furthermore, it was discovered that in some cases, like with the Supersonic Molecular Beam Deposition (SuMBD), the process promotes the formation of an elusive crystal forms, unreachable pure *via* standard conditions, but obtainable uncontaminated in thin film.[49]

The versatility of the molecular skeleton which allowed the design and synthesis of a large number of different TI based oligothiophenes, as well as, the structure determination of several polymorphs gave highlight on the structure-properties relationship.[45,48]

While the study directly on the device as made possible to relate the process of deposition with the final properties and crystal structure. The deposition technique as proved to be a valuable and effective way to control the polymorphism and morphology and could permits to tune the electrical and photophysical properties of 2,3-thienoimide-ended materials. One of the key points of this research is certainly the structural study that has permitted to obtain essential information for the optimization of the material, this knowledge of the crystal state is also extremely useful as a starting point for quanto-mechanical calculations and simulations.

COORDINATION POLYMERS

In recent years, the synthesis of coordination polymers and organic-inorganic hybrid materials has had a remarkable development, in view of their potential application as multifunctional and multi-responsive materials.[62–68] The interest arises form the possibility to combine the properties typical of inorganic compounds (high thermal mechanical stability, efficient electrical conductivity) with those typical of organic system (such as structural flexibility, high molecular versatility, low cost), and often the synergic combination of the different properties leads to new features.[69–71]

It is worth noting that coordination polymers and hybrid material are two different families, although in some cases the classification in ambiguous. The coordination polymers are characterized by a structure with a virtually infinite expansion in the direction of the metal-ligand connection, leading one-, two-, three- dimensional network (figure 3d).[72] They are usually described by the nodes (the metal ions or polynuclear metal clusters) of a certain geometry that are connected by multidentate organic ligands.

The organic-inorganic hybrid materials are characterized by an infinite 1-D, 2-D or 3-D network based on the inorganic part. The organic molecules are embedded in the structure but do not form strong interaction with the inorganic part (figure 3a).

One of the most interesting and notable example of organic-inorganic hybrid materials came from the hybrid perovskite (especially those based on lead or tin halides), known for their application in the organic photovoltaic cells.[73–75]

Some structures are not easily classified since they present at the same time the characteristic of a coordination polymer and an organic-inorganic hybrid material. In these examples, the inorganic part form 1D or 2-D network and the organic ligand is involved in the coordination of the metal atoms, as a terminal ligand that does not take part to the polymer expansion (figure 3b), or by bridging infinite inorganic part thus creating more complex structures. (figure 3c).[76,77]

The IUPAC recommendations on the nomenclature of the CP do not cover these cases which are described as coordination polymer or as hybrid material depending on the author.[72]

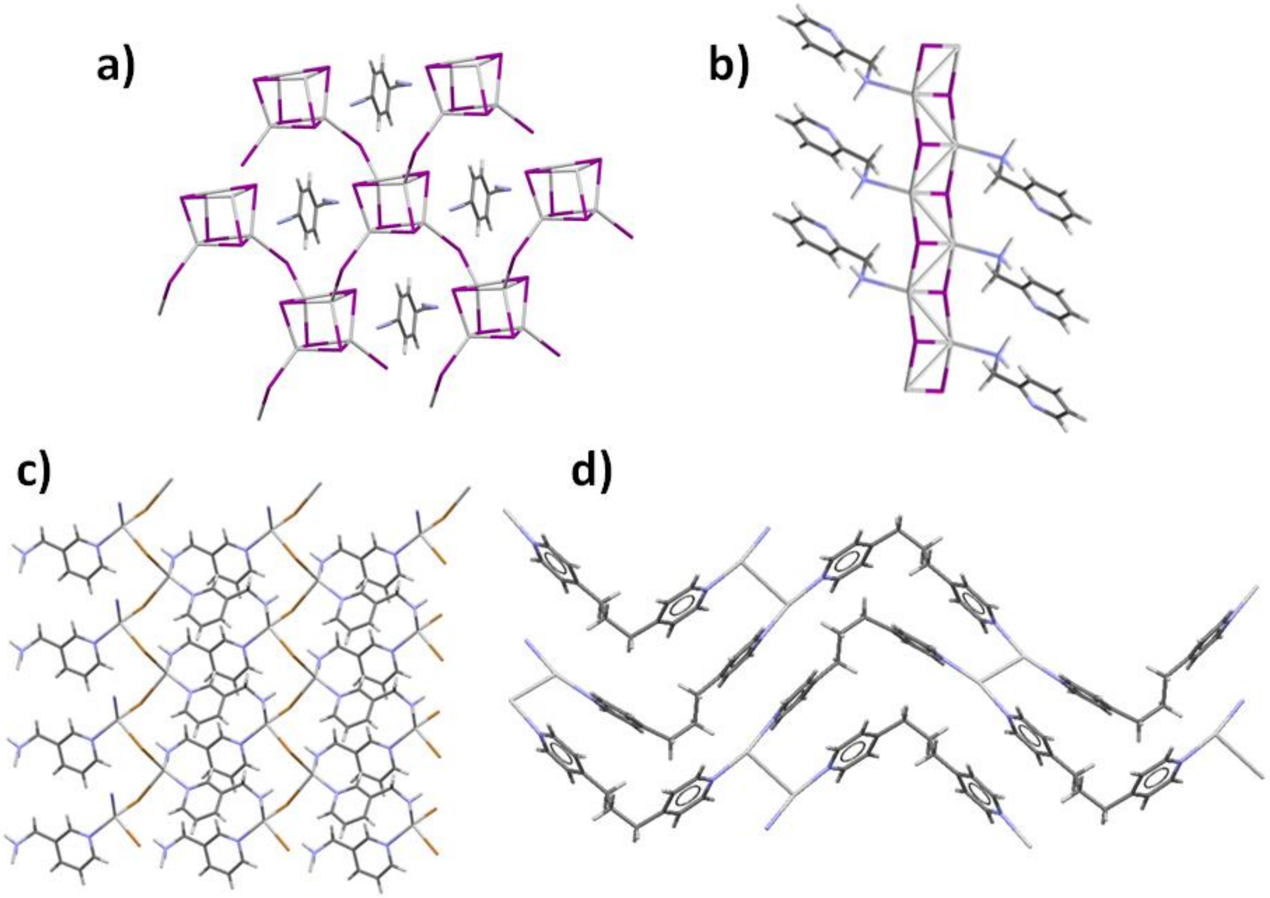

Figure 4. example of different type of metal-organic material based on silver. a) pure Organic-Inorganic Hybid Matrial (example:[(N-methyl-4-cyanopyridinium)(Ag_2I_3)]$_n$[78]); b) Organic-Inorganic Coordination Material with inorganic polymer expansion (example: [AgI(2pica)]$_n$); c) Organic-Inorganic Coodination Polymer with 2-D expansion (example: [AgBr(3pica)]$_n$); d) Pure Coordination Polymer (example: [Ag(BS)(BPP)$_2$][79])

What have in common CP and HM is the synthetic procedure. In fact hydrothermal and solvothermal reactions have been extensively applied to the synthesis of CPs and HMs. In contrast to other synthesis methods, the hydrothermal and solvothermal synthetic methods have the ability to increase the solubility and the reactivity of reagents, through the creation of an environment characterized by high-temperature and high-pressure. This technique permits to grow big and almost perfect crystals and could lead to precipitation of phases which are impossible to obtain by conventional reactions.[71,80–82]

In the recent year, with necessity of “green” and ideally solvent-free synthetic procedure, the mechanochemistry experienced an increasing success. The use of an appropriate mechanical stress could enhance the reactivity of reagents in solid state, in this kind of reaction the energy released by a mechanical stimulation is exploited for synthesis of new products.[83,84]

During my research, I focused my attention on d^{10} metal as precursors of coordination polymers, specifically Cu(I) and Ag(I), as halogenated salts.

Among the Cu(I) derivates the copper halides attract the attention due to their stability, the low cost and their safety compared to the metals widely used for electronic and optoelectronic applications (Pt, Pd, Ir, Rh, Ru). The coordination complexes based on Cu(I) halides have been subjects of study for years. The Cu(I) halide aggregates are characterized by an extensive structural diversity, due to the labile coordination numbers and geometry of both copper(I) and halide ions, which allow to obtain polynuclear inorganic cluster, with the bridging halide that connect metals atoms. The presence of the negative halides permits also to balance the metal charge in order to create a neutral inorganic cluster, in this way the organic ligand can be neutral and exploit the coordination bond with the metal without the use of counterions.[85]

The simplest inorganic cluster based on metals halides is the dimer, a zero-order aggregate (figure 5a). The combination of more dimers leads different and more complicated structures, for example cubanes (figure 5b) or double chains (figure 6b). Howevere it is possible to have very different geometry fro the single chains up to 4 or 6 metal clusters linked in 1-d to 2 d networks (figure 7). [85]

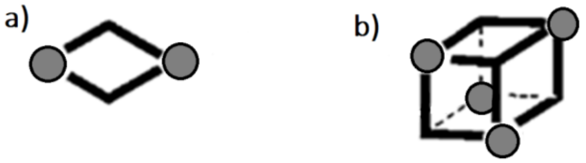

Figure 5. Zero-order aggregates. a) Dimer; b) Cubane.

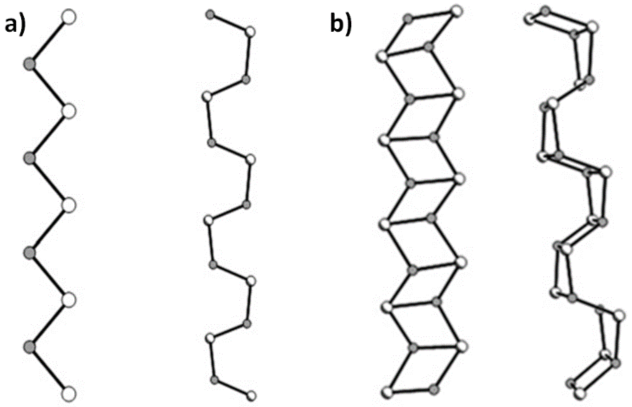

Figure 6. First-order aggregates.

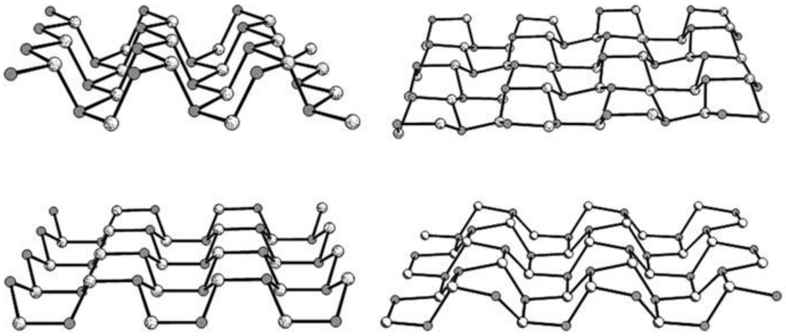

Figure 7. Second-order aggregates.

The presence of metallic cluster is probably favored by the formation of “Cuprophilic interactions” infact Cu-Cu distances, shorter that the sum of the Van der Wals radii, are observed in several cases and they are associated to particular emissive state.[88–91]

The luminescent properties of copper(I) halides have captured the attention of researchers because of their varied emissive nature.[87] They could present two distinct emission bands, one at high-energy attributed to halide-to-ligand charge transfer (^{3}XLCT), and the other at low-energy attributed to a triplet Cu–X Cluster-Centered (^{3}CC) excited state with the excitation localized in the copper-halogen core. This behavior is only possible in the presence of interactions between the metal centers. Moreover copper complexes are prone to present thermal activated delayed fluorescence (TADF).[86] In addition, they are charaterized by a high quantum yield in solid state that make them potential candidates for optoeltronic devices.

In a similar way to Cu(I), Ag(I) halides complexes present an intense luminescence in the solid state, especially at low temperature, the same structural variability and a potentially charge transport behaviour.[92,93] This phenomenon has proved to be particularly evident in crystalline structures with short Ag-Ag contacts, that in some silver compounds could be shorter than 3.44Å, effect known as “argentophilic interaction”.[93] The various possible structures of silver(I) halides are typically produced by the condensation of tetrahedral units of $[AgX_4]^{3-}$ that can share corners, sides of faces and form structures from 0 to 3 dimensions. The use of silver(I) halides in the fabrication of coordination polymers at the present time, is a research field almost unexplored.

REFERENCES

(1) Bragg, W. L. The Structure of Some Crystals as Indicated by Their Diffraction of X-Rays. *Proc. R. Soc. A Math. Phys. Eng. Sci.* **1913**, *89* (610), 248–277.

(2) Debye, P.; Scherrer, P. Interferenzen an Regellos Orientierten Teilchen Im Röntgenlicht. I. *Phys. Zeitschrift* **1916**, *17*, 277–283.

(3) Debye, P.; Scherrer, P. Ueber Die Konstitution von Graphit Und Amorpher. *Phys. Zeitschrift* **1917**, *18*, 291–301.

(4) *Structure from Diffraction Methods : Inorganic Materials Series.*; Bruce, D. W., O'Hare, D., Walton, R. I., Eds.; Wiley, **2014**.

(5) Oszlányi, G.; Sütő, A. Ab Initio Structure Solution by Charge Flipping. *Acta Crystallogr. Sect. A Found. Crystallogr.* **2004**, *60* (2), 134–141.

(6) Visser, J. W. A Fully Automatic Program for Finding the Unit Cell from Powder Data. *J. Appl. Crystallogr.* **1969**, *2* (pt 3), 89–95.

(7) Boultif, A.; Loueer, D. Indexing of Powder Diffraction Patterns for Low-Symmetry Lattices by the Successive Dichotomy Method. *J. Appl. Crystallogr.* **1991**, *24* (pt 6), 987–993.

(8) Werner, P. E.; Eriksson, L.; Westdahl, M. TREOR, a Semi-Exhaustive Trial-and-Error Powder Indexing Program for All Symmetries. *J. Appl. Crystallogr.* **1985**, *18* (5), 367–370.

(9) Le Bail, A. Monte Carlo Indexing with McMaille. *Powder Diffr.* **2004**, *19* (03), 249–254.

(10) Coelho, A. A. Indexing of Powder Diffraction Patterns by Iterative Use of Singular Value Decomposition. *J. Appl. Crystallogr.* **2003**, *36* (1), 86–95.

(11) Pawley, G. S. Unit-Cell Refinement from Powder Diffraction Scans. *J. Appl. Crystallogr.* **1981**, *14* (6), 357–361.

(12) Le Bail, A.; Duroy, H.; Fourquet, J. L. Ab-Initio Structure Determination of LiSbWO6by X-Ray Powder Diffraction. *Mater. Res. Bull.* **1988**, *23* (3), 447–452.

(13) Le Bail, A. Whole Powder Pattern Decomposition Methods and Applications: A Retrospection. *Powder Diffr.* **2005**, *20* (04), 316–326.

(14) *Powder Diffraction: Theory and Practice*; Dinnebier, R. E., Billinge, S. J. L., Eds.; RSC Publishing, 2008.

(15) Rietveld, H. M. A Profile Refinement Method for Nuclear and Magnetic Structures. *J. Appl. Crystallogr.* **1969**, *2* (2), 65–71.

(16) *Structure Determination from Powder Diffraction Data*; David, W. I. F., Shankland, K., McCusker, L. B., Bärlocher, C., Eds.; Oxford University Press, **2006**.

(17) Hill, R. J.; Howard, C. J. Quantitative Phase Analysis from Neutron Powder Diffraction Data Using the Rietveid Method Theory. *J. Appl. Crystallogr.* **1987**, *20*, 467–474.

(18) Keyes, R. W. Physical Limits of Silicon Transistors and Circuits. *Reports Prog. Phys.* **2005**, *68* (12), 2701–

2746.

(19) Thompson, S. E.; Parthasarathy, S. Moore's Law: The Future of Si Microelectronics. *Mater. Today* **2006**, *9* (6), 20–25.

(20) Chiang, C. K.; Fincher, C. R.; Park, Y. W.; Heeger, A. J.; Shirakawa, H.; Louis, E. J.; Gau, S. C.; MacDiarmid, A. G. Electrical Conductivity in Doped Polyacetylene. *Phys. Rev. Lett.* **1977**, *39* (17), 1098–1101.

(21) Murphy, A. R.; Fréchet, J. M. J. Organic Semiconducting Oligomers for Use in Thin Film Transistors. *Chemical Reviews*. **2007**, pp 1066–1096.

(22) Jiang, C. Y.; Chellappan, V.; Goh, W. P.; Zhang, J. Investigating Coating Method Induced Vertical Phase Distribution in Polymer-Fullerene Organic Solar Cells. *Sol. Energy Mater. Sol. Cells* **2018**, *179*, 241–246.

(23) Li, Y.; Sun, H.; Shi, Y.; Tsukagoshi, K. Patterning Technology for Solution-Processed Organic Crystal Field-Effect Transistors. *Science and Technology of Advanced Materials*. **2014**.

(24) Sanda, S.; Nagase, T.; Kobayashi, T.; Takimiya, K.; Sadamitsu, Y.; Naito, H. High-Performance Didodecylbenzothienobenzothiophene-Based Top-Gate Organic Transistors Processed by Spin Coating Using Binary Solvent Mixtures. *Org. Electron. physics, Mater. Appl.* **2018**, *58*, 306–312.

(25) *Organic Field-Effect Transistors*; Bao, Z., Locklin, J., Eds.; CRC Press, **2007**.

(26) Wang, C.; Dong, H.; Hu, W.; Liu, Y.; Zhu, D. Semiconducting π-Conjugated Systems in Field-Effect Transistors: A Material Odyssey of Organic Electronics. *Chem. Rev.* **2012**, *112* (4), 2208–2267.

(27) Mitzi, D. B.; Wang, S.; Feild, C. A.; Chess, C. A.; Guloy, A. M. Conducting Layered Organic-Inorganic Halides Containing 〈110〉-Oriented Perovskite Sheets. *Science (80-.).* **1995**, *267* (5203), 1473–1476.

(28) Burschka, J.; Pellet, N.; Moon, S. J.; Humphry-Baker, R.; Gao, P.; Nazeeruddin, M. K.; Grätzel, M. Sequential Deposition as a Route to High-Performance Perovskite-Sensitized Solar Cells. *Nature* **2013**, *499* (7458), 316–319.

(29) *Organic Light-Emitting Diodes (OLEDs) : Materials, Devices and Applications*; Buckley, A., Ed.; Woodhead Publishing, **2013**.

(30) Zoppi, L.; Baldridge, K. K. From Charge-Transfer Excitations to Charge-Transport Phenomena in Organic Molecular Crystals. *International Journal of Quantum Chemistry*. **2018**.

(31) Quinn, J. T. E.; Zhu, J.; Li, X.; Wang, J.; Li, Y. Recent Progress in the Development of N-Type Organic Semiconductors for Organic Field Effect Transistors. *J. Mater. Chem. C* **2017**, *5* (34), 8654–8681.

(32) Mattheus, C. C.; De Wijs, G. A.; De Groot, R. A.; Palstra, T. T. M. Modeling the Polymorphism of Pentacene. *J. Am. Chem. Soc.* **2003**, *125* (20), 6323–6330.

(33) Sundar, V. C.; Zaumseil, J.; Podzorov, V.; Menard, E.; Willett, R. L.; Someya, T.; Gershenson, M. E.; Rogers, J. A. Elastomeric Transistor Stamps : Reversible Probing Charge Transport in Organic Crystals. *Science (80-.).* **2004**, *303* (March), 1644–1646.

(34) Briseno, A. L.; Mannsfeld, S. C. B.; Reese, C.; Hancock, J. M.; Xiong, Y.; Jenekhe, S. A.; Bao, Z.; Xia, Y. Perylenediimide Nanowires and Their Use in Fabricating Field-Effect Transistors and Complementary

Inverters. *Nano Lett.* **2007**, *7* (9), 2847–2853.

(35) Jones, B. A.; Ahrens, M. J.; Yoon, M. H.; Facchetti, A.; Marks, T. J.; Wasielewski, M. R. High-Mobility Air-Stable n-Type Semiconductors with Processing Versatility: Dicyanoperylene-3,4:9,10-Bis(Dicarboximides). *Angew. Chemie - Int. Ed.* **2004**, *43* (46), 6363–6366.

(36) Wang, C.; Dong, H.; Jiang, L.; Hu, W. Organic Semiconductor Crystals. *Chemical Society Reviews*. **2018**, pp 422–500.

(37) Würthner, F.; Schmidt, R. Electronic and Crystal Engineering of Acenes for Solution-Processible Self-Assembling Organic Semiconductors. *Chemphyschem* **2006**, *7* (4), 793–797.

(38) Tsumura, A.; Koezuka, H.; Ando, T. Macromolecular Electronic Device: Field-Effect Transistor with a Polythiophene Thin Film. *Appl. Phys. Lett.* **1986**, *49* (18), 1210–1212.

(39) Koezuka, H.; Tsumura, A.; Ando, T. Field-Effect Transistor with Polythiophene Thin Film. *Synth. Met.* **1987**, *18* (1–3), 699–704.

(40) Laquindanum, J.; Katz, H. Morphological Origin of High Mobility in Pentacene Thin-Film Transistors. *Chem. Mater.* **1996**, *8* (11), 2542–2544.

(41) Gleiter, R.; Haberhauer, G.; Werz, D. B.; Rominger, F.; Bleiholder, C. From Noncovalent Chalcogen-Chalcogen Interactions to Supramolecular Aggregates: Experiments and Calculations. *Chemical Reviews*. American Chemical Society, **2018**, pp 2010–2041.

(42) Bai, M.; Thomas, S. P.; Kottokkaran, R.; Nayak, S. K.; Ramamurthy, P. C.; Guru Row, T. N. A Donor-Acceptor-Donor Structured Organic Conductor with S⋯S Chalcogen Bonding. *Cryst. Growth Des.* **2014**, *14* (2), 459–466.

(43) Brammer, L. Halogen Bonding, Chalcogen Bonding, Pnictogen Bonding, Tetrel Bonding: Origins, Current Status and Discussion. *Faraday Discuss.* **2017**, *203*, 485–507.

(44) Melucci, M.; Zambianchi, M.; Favaretto, L.; Gazzano, M.; Zanelli, A.; Monari, M.; Capelli, R.; Troisi, S.; Toffanin, S.; Muccini, M. Thienopyrrolyl Dione End-Capped Oligothiophene Ambipolar Semiconductors for Thin Film- and Light Emitting Transistors. *Chem. Commun.* **2011**, *47* (43), 11840–11842.

(45) Durso, M.; Gentili, D.; Bettini, C.; Zanelli, A.; Cavallini, M.; De Angelis, F.; Grazia Lobello, M.; Biondo, V.; Muccini, M.; Capelli, R.; et al. π-Core Tailoring for New High Performance Thieno(Bis)Imide Based n-Type Molecular Semiconductors. *Chem. Commun. (Camb).* **2013**, *49* (39), 4298–4300.

(46) Melucci, M.; Favaretto, L.; Zambianchi, M.; Durso, M.; Gazzano, M.; Zanelli, A.; Monari, M.; Lobello, M. G.; De Angelis, F.; Biondo, V.; et al. Molecular Tailoring of New Thieno(Bis)Imide-Based Semiconductors for Single Layer Ambipolar Light Emitting Transistors. *Chem. Mater.* **2013**, *25* (5), 668–676.

(47) Durso, M.; Bettini, C.; Zanelli, A.; Gazzano, M.; Lobello, M. G.; De Angelis, F.; Biondo, V.; Gentili, D.; Capelli, R.; Cavallini, M.; et al. Synthesis, Size-Dependent Optoelectronic and Charge Transport

Properties of Thieno(Bis)Imide End-Substituted Molecular Semiconductors. *Org. Electron. physics, Mater. Appl.* **2013**, *14* (11), 3089–3097.

(48) Zambianchi, M.; Favaretto, L.; Durso, M.; Bettini, C.; Zanelli, A.; Manet, I.; Gazzano, M.; Maini, L.; Gentili, D.; Toffanin, S.; et al. Synergic Effect of Unsaturated Inner Bridges and Polymorphism for Tuning the Optoelectronic Properties of 2,3-Thieno(Bis)Imide Based Materials. *J. Mater. Chem. C* **2015**, *3* (1), 121–131.

(49) Benvenuti, E.; Gentili, D.; Chiarella, F.; Portone, A.; Barra, M.; Cecchini, M.; Cappuccino, C.; Zambianchi, M.; Lopez, S. G.; Salzillo, T.; et al. Tuning Polymorphism in 2,3-Thienoimide Capped Oligothiophene Based Field-Effect Transistors by Implementing Vacuum and Solution Deposition Methods. *J. Mater. Chem. C* **2018**, *6* (21), 5601–5608.

(50) Melucci, M.; Durso, M.; Bettini, C.; Gazzano, M.; Maini, L.; Toffanin, S.; Cavallini, S.; Cavallini, M.; Gentili, D.; Biondo, V.; et al. Structure–property Relationships in Multifunctional Thieno(Bis)Imide-Based Semiconductors with Different Sized and Shaped N-Alkyl Ends. *J. Mater. Chem. C* **2014**, *2* (17), 3448.

(51) Mishra, A.; Ma, C. Q.; Bäuerle, P. Functional Oligothiophenes: Molecular Design for Multidimensional Nanoarchitectures and Their Applications. *Chemical Reviews*. **2009**, pp 1141–1176.

(52) Barbarella, G.; Melucci, M.; Sotgiu, G. The Versatile Thiophene: An Overview of Recent Research on Thiophene-Based Materials. *Advanced Materials*. Wiley-Blackwell, **2005**, pp 1581–1593.

(53) Maini, L.; Gallino, F.; Zambianchi, M.; Durso, M.; Gazzano, M.; Rubini, K.; Gentili, D.; Manet, I.; Muccini, M.; Toffanin, S.; et al. Chemical Design Enables the Control of Conformational Polymorphism in Functional 2,3-Thieno(Bis)Imide-Ended Materials. *Chem. Commun.* **2014**, *51* (11), 2033–2035.

(54) Lee, J. H.; Harada, R.; Kawamura, S.; Koseki, S. Development of a Novel Time-Temperature Integrator/Indicator (TTI) Based on the Maillard Reaction for Visual Thermal Monitoring of the Cooking Process. *Food Bioprocess Technol.* **2018**, *11* (1), 185–193.

(55) Wang, S.; Liu, X.; Yang, M.; Zhang, Y.; Xiang, K.; Tang, R. Review of Time Temperature Indicators as Quality Monitors in Food Packaging. *Packaging Technology and Science*. Wiley-Blackwell, **2015**, pp 839–867.

(56) Welt, B. A.; Sage, D. S.; Berger, K. L. Performance Specification of Time-Temperature Integrators Designed to Protect against Botulism in Refrigerated Fresh Foods. *Journal of Food Science*. Wiley/Blackwell, **2003**, pp 2–9.

(57) de Boer, R. W. I.; Gershenson, M. E.; Morpurgo, A. F.; Podzorov, V. Organic Single-Crystal Field-Effect Transistors. *Phys. Status Solidi* **2004**, *201* (6), 1302–1331.

(58) Rahman, A. T. M. M.; Kim, D. H.; Jang, H. D.; Yang, J. H.; Lee, S. J. Preliminary Study on Biosensor-Type Time-Temperature Integrator for Intelligent Food Packaging. *Sensors* **2018**, *18* (6), 1949.

(59) Gentili, D.; Durso, M.; Bettini, C.; Manet, I.; Gazzano, M.; Capelli, R.; Muccini, M.; Melucci, M.; Cavallini,

M. A Time-Temperature Integrator Based on Fluorescent and Polymorphic Compounds. *Sci. Rep.* **2013**, *3*, 2581.

(60) El Helou, M.; Medenbach, O.; Witte, G. Rubrene Microcrystals: A Route to Investigate Surface Morphology and Bulk Anisotropies of Organic Semiconductors. *Cryst. Growth Des.* **2010**, *10* (8), 3496–3501.

(61) Jurchescu, O. D.; Mourey, D. A.; Subramanian, S.; Parkin, S. R.; Vogel, B. M.; Anthony, J. E.; Jackson, T. N.; Gundlach, D. J. Effects of Polymorphism on Charge Transport in Organic Semiconductors. *Phys. Rev. B* **2009**, *80* (8), 085201.

(62) Hu, Z.; Deibert, B. J.; Li, J. Luminescent Metal-Organic Frameworks for Chemical Sensing and Explosive Detection. *Chemical Society Reviews*. The Royal Society of Chemistry, **2014**, pp 5815–5840.

(63) Wenger, O. S. Vapochromism in Organometallic and Coordination Complexes: Chemical Sensors for Volatile Organic Compounds. *Chemical Reviews*. American Chemical Society, **2013**, pp 3686–3733.

(64) Park, H.; Kwon, E.; Chiang, H.; Im, H.; Lee, K. Y.; Kim, J.; Kim, T. H. Reversible Crystal Transformations and Luminescence Vapochromism by Fast Guest Exchange in Cu(I) Coordination Polymers. *Inorg. Chem.* **2017**, *56* (14), 8287–8294.

(65) Hayashi, T.; Kobayashi, A.; Ohara, H.; Yoshida, M.; Matsumoto, T.; Chang, H. C.; Kato, M. Vapochromic Luminescence and Flexibility Control of Porous Coordination Polymers by Substitution of Luminescent Multinuclear Cu(I) Cluster Nodes. *Inorg. Chem.* **2015**, *54* (18), 8905–8913.

(66) Benito, Q.; Le Goff, X. F.; Maron, S.; Fargues, A.; Garcia, A.; Martineau, C.; Taulelle, F.; Kahlal, S.; Gacoin, T.; Boilot, J. P.; et al. Polymorphic Copper Iodide Clusters: Insights into the Mechanochromic Luminescence Properties. *J. Am. Chem. Soc.* **2014**, *136* (32), 11311–11320.

(67) Benito, Q.; Maurin, I.; Cheisson, T.; Nocton, G.; Fargues, A.; Garcia, A.; Martineau, C.; Gacoin, T.; Boilot, J. P.; Perruchas, S. Mechanochromic Luminescence of Copper Iodide Clusters. *Chem. - A Eur. J.* **2015**, *21* (15), 5892–5897.

(68) Benito, Q.; Baptiste, B.; Polian, A.; Delbes, L.; Martinelli, L.; Gacoin, T.; Boilot, J. P.; Perruchas, S. Pressure Control of Cuprophilic Interactions in a Luminescent Mechanochromic Copper Cluster. *Inorg. Chem.* **2015**, *54* (20), 9821–9825.

(69) Zhang, X.; Wang, W.; Hu, Z.; Wang, G.; Uvdal, K. Coordination Polymers for Energy Transfer: Preparations, Properties, Sensing Applications, and Perspectives. *Coord. Chem. Rev.* **2015**, *284*, 206–235.

(70) Batten, S. R.; Chen, B.; Vittal, J. J. Coordination Polymers/MOFs: Structures, Properties and Applications. *Chempluschem* **2016**, *81* (8), 669–670.

(71) Hong, M. C.; Chen, L. *Design and Construction of Coordination Polymers*; Hong, M.-C., Chen, L., Eds.; John Wiley & Sons, Inc.: Hoboken, USA, **2009**.

(72) Batten, S. R.; Champness, N. R.; Chen, X.-M.; Garcia-Martinez, J.; Kitagawa, S.; Öhrström, L.; O'keeffe,

M.; Suh, M. P.; Reedijk, J. Terminology of Metal-Organic Frameworks and Coordination Polymers (IUPAC Recommendations 2013)*. *Pure Appl. Chem* **2013**, *85* (8), 1715–1724.

(73) Zhou, R.; Yang, Z.; Xu, J.; Cao, G. Synergistic Combination of Semiconductor Quantum Dots and Organic-Inorganic Halide Perovskites for Hybrid Solar Cells. *Coordination Chemistry Reviews*. Elsevier, **2018**, pp 279–313.

(74) Ma, S.; Cai, M.; Cheng, T.; Ding, X.; Shi, X.; Alsaedi, A.; Hayat, T.; Ding, Y.; Tan, Z.; Dai, S. Two-Dimensional Organic-Inorganic Hybrid Perovskite: From Material Properties to Device Applications. *Science China Materials*. Science China Press, **2018**, pp 1257–1277.

(75) Liu, X.; Yu, D.; Song, X.; Zeng, H. Metal Halide Perovskites: Synthesis, Ion Migration, and Application in Field-Effect Transistors. *Small*. Wiley-Blackwell, **2018**, p 1801460.

(76) Troyano, J.; Perles, J.; Amo-Ochoa, P.; Zamora, F.; Delgado, S. Strong Luminescent Copper(i) Halide Coordination Polymers and Dinuclear Complexes with Thioacetamide and N,N′-Donor Ligands. *CrystEngComm* **2016**, *18* (10), 1809–1817.

(77) Amo-Ochoa, P.; Hassanein, K.; Gómez-García, C. J.; Benmansour, S.; Perles, J.; Castillo, O.; Martínez, J. I.; Ocón, P.; Zamora, F. Reversible Stimulus-Responsive Cu(i) Iodide Pyridine Coordination Polymer. *Chem. Commun.* **2015**, *51* (76), 14306–14309.

(78) Shen, J.; Zhang, C.; Yu, T.; An, L.; Fu, Y. Structural and Functional Modulation of Five 4-Cyanopyridinium Iodoargentates Built up from Cubane-like Ag4I4 Nodes. *Cryst. Growth Des.* **2014**, *14* (12), 6337–6342.

(79) Zhang, X. L.; Tang, G. M.; Wang, Y. T. A Set of Ag-Based Metal Coordination Polymers with Sulfonate Group: Syntheses, Crystal Structures and Luminescent Behaviors. *Polyhedron* **2018**, *148*, 55–69.

(80) Zhao, Y.; Li, K.; Li, J. Solvothermal Synthesis of Multifunctional Coordination Polymers. *Zeitschrift fur Naturforschung - Section B Journal of Chemical Sciences*. Verlag der Zeitschrift für Naturforschung, **2010**, pp 976–998.

(81) Forster, P. M.; Thomas, P. M.; Cheetham, A. K. Biphasic Solvothermal Synthesis: A New Approach for Hybrid Inorganic-Organic Materials. *Chem. Mater.* **2002**, *14* (1), 17–20.

(82) Pal, S.; Pal, T. K.; Bharadwaj, P. K. Solvothermal Synthesis of Coordination Polymers at Different Temperatures and Their Luminescence Studies. *CrystEngComm* **2016**, *18* (10), 1825–1831.

(83) Braga, D.; Grepioni, F.; Maini, L.; D'Agostino, S. From Solid-State Structure and Dynamics to Crystal Engineering. *European Journal of Inorganic Chemistry*. Wiley-Blackwell, **2018**, pp 3597–3605.

(84) Quaresma, S.; André, V.; Fernandes, A.; Duarte, M. T. Mechanochemistry – A Green Synthetic Methodology Leading to Metallodrugs, Metallopharmaceuticals and Bio-Inspired Metal-Organic Frameworks. *Inorganica Chimica Acta*. **2017**, pp 309–318.

(85) Peng, R.; Li, M.; Li, D. Copper(I) Halides: A Versatile Family in Coordination Chemistry and Crystal Engineering. *Coordination Chemistry Reviews*. Elsevier, **2010**, pp 1–18.

(86) Yersin, H.; Czerwieniec, R.; Shafikov, M. Z.; Suleymanova, A. F. TADF Material Design: Photophysical

Background and Case Studies Focusing on CuIand AgIComplexes. *ChemPhysChem*. **2017**, pp 3508–3535.

(87) Graham, P. M.; Pike, R. D.; Sabat, M.; Bailey, R. D.; Pennington, W. T. Coordination Polymers of Copper(I) Halides. *Inorg. Chem.* **2000**, *39* (22), 5121–5132.

(88) Nitsch, J.; Lacemon, F.; Lorbach, A.; Eichhorn, A.; Cisnetti, F.; Steffen, A. Cuprophilic Interactions in Highly Luminescent Dicopper(i)-NHC-Picolyl Complexes-Fast Phosphorescence or TADF? *Chem. Commun.* **2016**, *52* (14), 2932–2935.

(89) Hermann, H. L.; Boche, G.; Schwerdtfeger, P. Metallophilic Interactions in Closed-Shell Copper(I) Compounds - A Theoretical Study. *Chem. - A Eur. J.* **2001**, *7* (24), 5333–5342.

(90) Zhang, J. P.; Wang, Y. B.; Huang, X. C.; Lin, Y. Y.; Chen, X. M. Metallophilicity versus π-π Interactions: Ligand-Unsupported Argentophilicity/Cuprophilicity in Oligomers-of-Dimers [M2L2]n(M = CuIor AgI, L = Tridentate Ligand). *Chem. - A Eur. J.* **2005**, *11* (2), 552–561.

(91) Claveria-Cadiz, F.; Arratia-Perez, R.; Guajardo-Maturana, R.; Muñoz-Castro, A. Survey of Short and Long Cuprophilic D10-D10contacts for Tetranuclear Copper Clusters. Understanding of Bonding and Ligand Role from a Planar Superatom Perspective. *New J. Chem.* **2018**, *42* (11), 8874–8881.

(92) Di Motta, S.; Siracusa, M.; Negri, F. Structural and Thermal Effects on the Charge Transport of Core-Twisted Chlorinated Perylene Bisimide Semiconductors. *J. Phys. Chem. C* **2011**, *115* (42), 20754–20764.

(93) Schmidbaur, H.; Schier, A. Argentophilic Interactions. *Angewandte Chemie - International Edition*. Wiley-Blackwell, **2015**, pp 746–784.

CHAPTER 2: PROJECT OVERVIEW

The aim of my PhD project was the synthesis, characterization and crystal structure determination both from single crystal and powder X-ray diffraction, of organic molecular materials and coordination polymers.

The first part of the project was dedicated to the structural characterization of 2,3-thienoimide (TI) based oligothiophenes, a family of organic semiconductors. The study was carry out in collaboration with the CNR, and the molecules had been synthesized by the group of Dr. Manuela Melucci at ISOF-CNR. These molecules present different crystalline forms that can be obtained by changing the solvent of recrystallization or combining deposition and annealing processes, so part of the work was also dedicated to the study of polymorphism and the analysis of the solid state transition between the different crystal phases (see chapter 4)

The thermal analysis dedicated to detect the polymorphs conversion was investigated mainly *via* hot-stage microscopy and variable temperature X-ray diffraction, while the structural characterization was performed via Single Crystal X-ray diffraction and Powder X-ray diffraction. Due to the complexity of the systems, we also decided to validate and confirm the structure obtained by XRPD with the support of other techniques, such as the Raman spectroscopy as presented in chapter 3.

These molecules are characterized by a strong luminescence which dramatically changes depending on the polymorph, this behaviour makes the molecule interesting fo potential application in OFET, OLET or TTI. Particular efforts were made by us to determine the crystal structure to have more insight on structure–properties relationship (see results in chapter 6).

The challenging characterization of these materials persuades us to also to follow unconventional method to determine the crystal structure. Inspired by the work of Prof. Tsunehisa Kimura on the magnetic alignment of diamagnetic materials *via* an external magnetic field and thanks to the Marco Polo project, I had the opportunity to spend four months in the group of Prof. Kimura at the Kyoto University.

During my visit in Japan I performed various experiment to align my crystalline powder to reproduce a single crystal, without obtain crystal data usable for structure determination. However, I tried also several crystallization experiments in presence of strong magnetic fields, which clearly influence the rate of crystallization and the crystallinity of the final product. The results of the crystallization in presence of magnetic field are reported in chapter 5.

Part of my thesis also cover the study of new luminescent materials based on coordination polymers, deepening a research previously started by the MCE group on luminescent complexes based on d10 metal halides.

New coordination compounds based on CuI and AgX (X= I and Br) were synthesized. These new compounds are characterized by a 1-D or 2-D expansion as required for the coordination polymers. However, in several cases the 1-D chain is due to the formation of infinite chain of CuI or AgX which make these compounds closer to the hybrid material than to coordination polymers.

Given the nature of the reagents used, the main synthetic methods were the solvothermal reaction and the mechanochemical reaction. The drawback of the mechanochemistry is that the final product, in form of a microcrystalline powder, is unsuitable for the SCXRD, so the structural characterization was carried out *via* XRPD. The presence of the heavy atoms such as metal and Iodide could make difficult the precise determination of the ligand position, due to the higher contribution of the heavy atoms to the diffraction with respect than the organic part. However, it was possible to determine the structure of an elusive new coordination polymer of CuI obtained only by mechanochemisirty (chapter 7).

We synthesis different new coordination polymers based on AgX which show excellent luminescence properties. Their structures were determined by SCXRD or XRPD; and moreover, in one case the structure presents a particular conformation were the metal atoms are located in an infinite chain with very short metal-metal distances, a feature often connected with the charge transport ability (see chapter 8) Further photophyisical and electrical characterization is needed to testify their applicability in electronic or optoelectronic devices.

CHAPTER 3: A SYNERGIC APPROACH OF X-RAY POWDER DIFFRACTION AND RAMAN SPECTROSCOPY FOR CRYSTAL STRUCTURE DETERMINATION OF 2,3-THIENOIMIDE CAPPED OLIGOTHIOPHENES

The study is focused on the structural characterization of two TI compounds, named C6-NT4N and C8-NT4N by X-ray powder diffraction.

I performed the crystallization experiments and the preliminary powder X-ray analysis. Higher quality powder diffraction data have been later obtained at the synchrotron facility of the PSI institute in Villigen, Switzerland, with the assistance of Dr. Paolo Mazzeo. I was able to solve the structure of the two compounds form the high quality data.

To confirm the molecular conformation in the crystal that we found via a simulated annealing method, Dr. Tommaso Salzillo and prof. E. Venuti (Dipartimento di Chimica Industriale Toso Montanari) performed micro Raman spectroscopy analysis on the crystalline sample. From the Raman measurement and the diffraction analysis we developed a Raman based approach for the rapid identification of the molecular conformation, helping to discern between different conformers of the aromatic core.

The results were also validated via some calculation dedicated to the optimization of the molecular geometry and simulation of theoretical Raman spectra, performed by Dr. Raffaele Guido della Valle.

Issue 5, 2018

From the journal:
Physical Chemistry Chemical Physics

A synergic approach of X-ray powder diffraction and Raman spectroscopy for crystal structure determination of 2,3-thienoimide capped oligothiophenes

C. Cappuccino,[a] P. P. Mazzeo,[bc] T. Salzillo,*[d] E. Venuti,[d] A. Giunchi,[d] R. G. Della Valle,[d] A. Brillante,[d] C. Bettini,[e] M. Melucci[e] and L. Maini*[a]

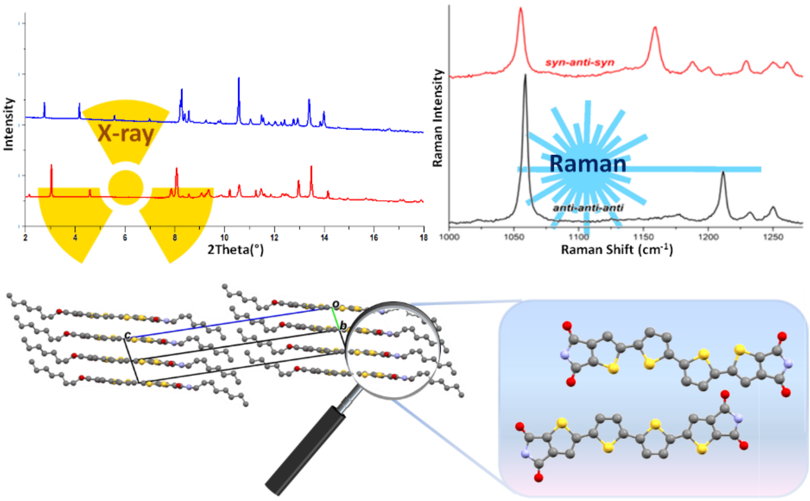

For copyright reasons only the link to the original article is reported here:

https://pubs.rsc.org/en/content/articlelanding/2018/cp/c7cp06679a#!divAbstract

CHAPTER 4: TUNING POLYMORPHISM IN 2,3-THIENOIMIDE CAPPED OLIGOTHIOPHENE BASED FIELD-EFFECT TRANSISTORS BY IMPLEMENTING VACUUM AND SOLUTION DEPOSITION METHODS

The present work was a part of the PhD project of Dr. Emilia Benvenuti, from the group of Dr. Stefano Toffanin at ISMN-CNR in Bologna. It was focused on the polymorphic control of TI materials into the active layer of OFET devices by the deposition technique.

Our contribution to this project was limited to the structural analysis and characterization by X-ray diffraction of the deposited thin film, a not easy task due to the small thickness of the analyzed thin films (30 nm). However, our work permitted to determine the presence of a new crystal phase, passed unnoticed until then. The mentioned polymorph was previously detected in bulk sample of the same materials, as a small impurity concomitant with the known crystal phases. During the deposition it was possible to obtain pure the new phases under appropriate conditions. With the cooperation of the Prof. Venuti group it was possible to partially determine the molecular conformation of the new polymorph via Raman Spectroscopy, using the procedure described in the previous chapter.

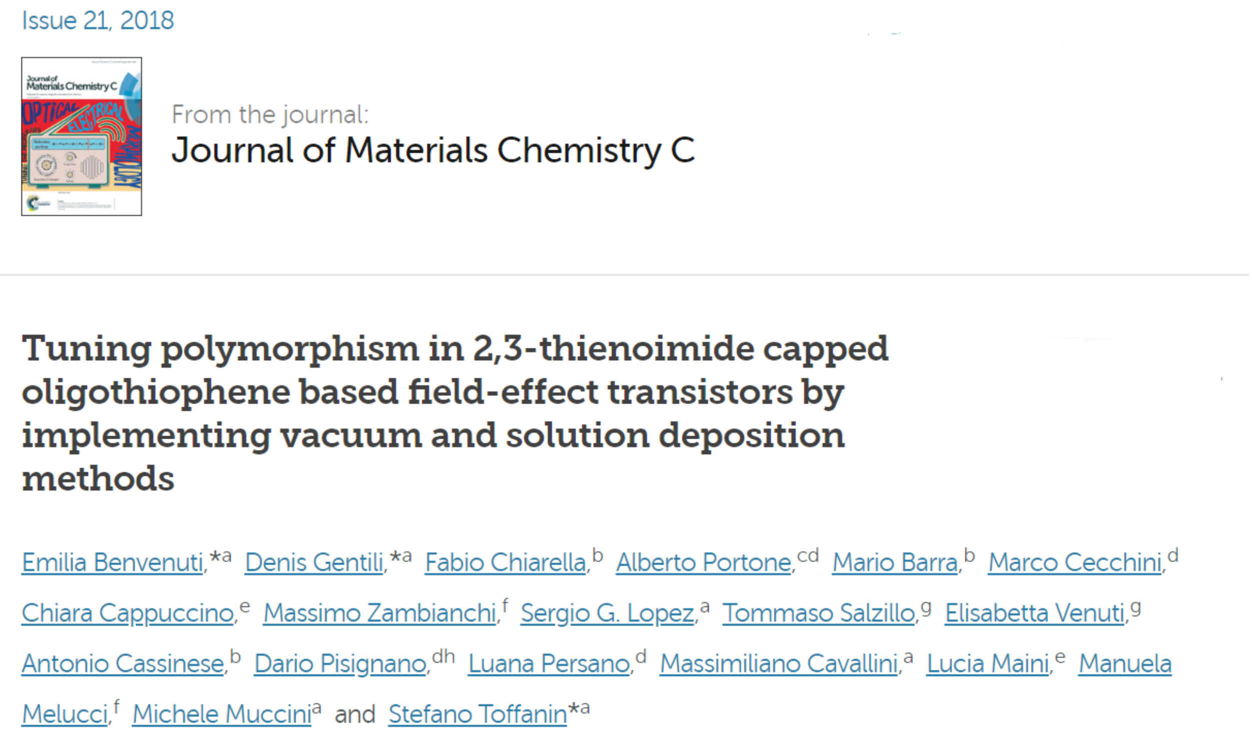

Issue 21, 2018

From the journal:
Journal of Materials Chemistry C

Tuning polymorphism in 2,3-thienoimide capped oligothiophene based field-effect transistors by implementing vacuum and solution deposition methods

Emilia Benvenuti,*[a] Denis Gentili,*[a] Fabio Chiarella,[b] Alberto Portone,[cd] Mario Barra,[b] Marco Cecchini,[d] Chiara Cappuccino,[e] Massimo Zambianchi,[f] Sergio G. Lopez,[a] Tommaso Salzillo,[g] Elisabetta Venuti,[g] Antonio Cassinese,[b] Dario Pisignano,[dh] Luana Persano,[d] Massimiliano Cavallini,[a] Lucia Maini,[e] Manuela Melucci,[f] Michele Muccini[a] and Stefano Toffanin*[a]

For copyright reasons only the link to the original article is reported here:

https://pubs.rsc.org/en/content/articlelanding/2018/tc/c8tc00544c#!divAbstract

CHAPTER 5: HIGH MAGNETIC FIELD INDUCES HIGHER CRYSTALLINITY OF 2,3-THIENOIMIDE ENDED OLIGOTHIOPHENE PHASES AND PERMITS THE DETECTION OF AN ELUSIVE POLYMORPH

The project arose from a collaboration between the group of prof Kimura (Kyoto University) and the Molecular Crystal Engineering group.

I was in charge of the structure determination and polymorph characterization. The thieno(bis)imide oligothiophenes present several problems: they hardly form crystals suitable for SCXRD and the microcrystalline powder is affected by a strong inhomogeneity in crystallite size which makes really challenging the structure determination.

Conventional crystallization techniques are not able to grow powders with a proper crystallinity, or crystals big enough for SCXRD analysis, so alternative approaches have been searched to boost the crystallization.

The group of prof. Kimura has also developed a pioneering technique which allows to obtain, from a multicrystalline powder, a composite single crystal-like material in which microcrystals are oriented three-dimensionally in a polymer matrix. The composite material obtained, called MOMA (Magnetically Oriented Microcrystal Array), possesses an X-ray diffraction pattern equivalent to those obtained from a single crystal.[1–3]

I spent four months in the Prof. Kimura laboratory (Fibrous Biomaterials Laboratory, faculty of Agriculture, Kyoto University) trying to apply the MOMA technique to the TBO crystalline powder without success. In the meantime, I also studied the effect of a strong external magnetic field on the crystallization and deposition of TI material. Prof. Tsunehisa Kimura an Dr. Fumiko Kimura assisted my work during my permanence in the Kyoto University.

(1) Kimura, F.; Mizutani, K.; Mikami, B.; Kimura, T. Single-Crystal X-Ray Diffraction Study of a Magnetically Oriented Microcrystal Array of Lysozyme. *Cryst. Growth Des.* **2011**, *11* (1), 12–15.

(2) Kimura, F.; Oshima, W.; Matsumoto, H.; Uekusa, H.; Aburaya, K.; Maeyama, M.; Kimura, T. Single Crystal Structure Analysis via Magnetically Oriented Microcrystal Arrays. *CrystEngComm* **2014**, *16* (29), 6630–6634.

(3) Kimura, F.; Kimura, T.; Matsumoto, K.; Metoki, N. Single-Crystal Neutron Diffraction Study of Pseudo Single Crystal Prepared from Microcrystalline Powder. *Cryst. Growth Des.* **2010**, *10* (1), 48–51.

ABSTRACT

The crystals of a diamagnetic 2,3-thienoimided molecular material growth in presence of an external magnetic field presented an improvement of the crystallinity of the material and it was also observed the presence of an unidentified crystal phase heighten by the magnetic field.

INTRODUCTION

The study of organic semiconductors is experiencing a period of great development where scientists are attempting to design new materials capable to replace the traditional silicon as active material in electronic and optoelectronic devices. One of the most evident advantages that draw the attention on organic materials is the possibility to engineer new molecules with tailored properties, like luminescence or ambipolar charge transport.[1]

It is well known that the molecular packing, as well as morphology and crystallinity of the organic material packing has a great influence on the finals properties of the material. Hence, control of the polymorphism and the increasing of the crystallinity are pursued for the fabrication of organic devices with enhanced performances.[2,3]

It is important to say that deposition methods influence the crystallinity as well as the final crystal form this is why an in-depth knowledge of structures and thermodynamic relationships of the polymorphs are advocated for the analysis of the charge transport and control of the device. Therefore, the polymorphism potentially could be a problematic feature, so it is really fundamental to find an efficient way to control the polymorphism during the deposition and the thin film formation.

Several studies have suggested various techniques which allow to control the polymorphism during the deposition.[4]

In some cases the crystallinity has been enhanced by the presence of external electrical[5] or magnetic field,[6] but in the last case the molecules presented in most cases paramagnetic metals.[7] It has been observed that thin film of pentacene presents and improved of crystallinity when grown under a magnetic field.[8]

Recently, crystallization of coronene in a magnetic field lead to the determination of a new polymorph.[9] Some experiment of crystal growth of protein inside a magnetic field were performed to increase the crystallinity in order to make easier the diffraction analysis of these systems.[10,11,12]

The effect of strong magnetic field on diamagnetic materials was also investigated by T. Kimura, who showed how an appropriate magnetic field can align a suspension of microcrystals in order to produces XRD images comparable to those obtained from real single crystal.[13,14,15]

However, except these sporadic examples, the influence of external magnetic field of adequate magnitude on the crystallization of organic diamagnetic molecules is almost unexplored.

RESULTS AND DISCUSSION

Here, aiming at a fine control of crystalline phase and crystal orientation in thin deposits, we explore the effect of an external magnetic field on the crystal packing and self-assembly of a model multifunctional molecular material namely (E)-2,2’-(5,5’-(Ethene-1,2-diyl)bis(5-hexyl-4H-thieno[2,3-c]pyrrole-4,6(5H)-dione), hereafter NTE.[16]

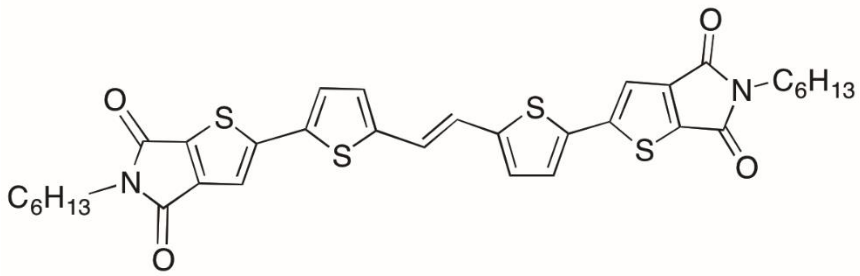

Figure 1. Schematic structure of NTE molecule.

This compound, belongs to the family of 2,3-thienoimide ended oligothiophenes, a class of ambipolar and electroluminescent semiconductors suitable as active layers of different types of thin film organic devices.[16,17] NTE material, is characterized by the capability of crystallizing into different phases and by polymorphism-driven fluorescent emission this enabling also its exploitation for the fabrication of time temperature integrator devices able to monitor temperature evolution through fluorescence changes.[18]

To fully understand the thermodynamic relationship of the polymorphs the molecule was recrystallized in different solvents to be able to obtain pure phases and/or single crystals suitable for single-crystal X-ray diffraction. The red phase I is favored by solvent evaporation of high boiling point solvents, like toluene, and presents a needle-like morphology which are characterized by a red emission. Phase II is obtained by evaporation low boiling point solvents, especially dichloromethane and chloroform. The crystals present a plate-like morphology with an orange emission. By differential scanning calorimetry (DSC) and hot-stage microscopy (HSM) it is clear that phase I converts into phase II at 142°C as confirmed also by XRPD at variable temperature. The endothermic phase transition is consistent with an enantiotropy relation of the two polymorphs, with phase I stable at RT and phase II at HT. The cooling curve shows the recrystallization and a second weak exothermic event at 103°C which cannot be ascribable to the conversion phase II to phase I and this new transition is completely reversible since it is also visible during the second heating ramp (see figure 6). The presence of this phase transition suggests the existence of two polymorphs with close structure which are fully reversible by varying the temperature, which we called phase II^{LT} (low-temperature) and phase II^{HT} (high-temperature). The XRPD collected at VT confirmed the presence of two polymorphs with close crystal structure.

Crystals suitable for SCXRD were obtained only by vapour diffusion technique (acetonitrile in a solution of NTE in toluene) or slow evaporation of toluene which took about a week. The structure was resolved in the triclinic space group P-1 with half molecule of NTE in the asimmetric unit (table 1); the double bond is located on the inversion centre. The molecular core is planar as observed in the majority of thiophenic compounds. The sulphur position of the thienimide group is disordered in the syn/anti and it was refined for 66% in anti conformation and for 34% in syn conformation (figure 2a). In the 3D packing the molecules are piled in columnar stack linked together through π-π stacking interactions with one molecule of the upper and lower layers as shown in figure 2b.

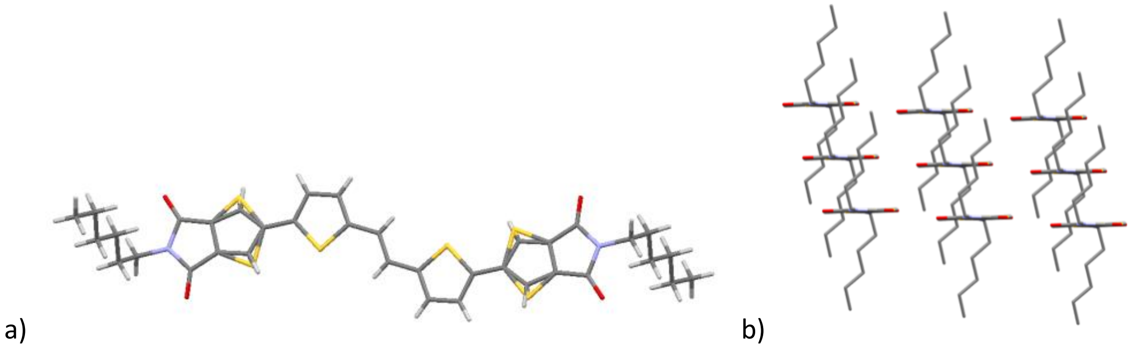

Figure 2. Crystal structure of NTE phase I, a) molecular conformation, b) π-π stacking direction.

All attempts to obtain SC of Phase II failed and it was characterised only by PXRD collected at PSI centre (Villigen, Switzerland). From the VT-XRPD it was possible to index the pattern (crystal cells in table 6) with a monoclinic cell with volume consistent with one molecule in the asymmetric unit. The cell presents a long axis (a= 33.814(4) and 33.325(1)Å respectively for phase II^{LT} and II^{HT}) which suggests a dramatic different packing respect of phase I. In recent studies on polymorphism of 2,3-thienoimide ended oligothiophenes we observed that structures with short axes (phase A) are characterized by a molecular packing similar to phase I, while structures with long axes (phase B) presented a brick wall arrangement of the molecule with the formation of a bidimensional π-π stacking between the aromatic cores of the molecules.[19,20] It worth noting that columnar packing (phase A) is characterized by a red emission which shifts to higher energy when converted into phase B. Similarly, NTE, after the thermal annealing conversion of phase I to II shows a blue shifted emission this suggesting that phase II presents a brick wall arrangement.

We explored the effect of an high magnetic field on the growth of the NTE crystals with several possible results: a) obtain crystals of phase II suitable for SCXRD, b) to limit or even remove the disorder of the thienoimide group, and c) to align the orientation of the crystals during the deposition of the material.

The crystallization of NTE was performed by solvent evaporation inside an electromagnet with a magnetic field of 2T of magnitude. Approximately 3 mL of a saturated solution of NTE in toluene or dichloromethane were prepared and filtered, the vial containing the solution was placed opened inside the magnet so that the solvent could evaporate. While the crystallization in CH_2Cl_2 leads only to crystalline powders, after approximately 3 hours some visible crystals appeared inside the vial with toluene. After a total time of 5 hours the vial was removed from the magnetic field and the crystals inside the solution have been recovered and analysed by SCXRD. Comparing the crystallization processess inside and outside the magnetic field it was observed that inside the magnet the precipitation was faster than outside: crystals suitable for diffraction were obtained after only 5 hours from a simple solvent evaporation inside the magnet, while outside it took about a week. Both crystals of NTE phase I obtained inside and outside the magnetic field were collected. Although in both cases the best crystal was chosen, the collection data show remarkably differences. The R_{int} for the crystal grown inside the magnetic field is lower than the one grown outside (R_{int}=0,070 and 0,099 respectively) as well as the mosaicity whose parameter e_3, that represent the mosaicity in the scanning direction, change from a value of 1.77° to 2.55°. It means that the crystalline domains that make up the single crystal possess a better alignment in the sample grown at 2T. Besides these aspects, no differences were observed in the conformational disorder that maintains the same percentage for the syn and the anti conformations.

The depositions were performed by drop-casting method, using toluene, and by antisolvent vapour diffusion. In this technique the substrate with the NTE solution (in toluene) was positioned inside a sealed container in presence of acetonitrile; the slow migration of the antisolvent inside the solution permits a slower and more controlled crystallization. In both cases the same deposition was carried out inside and outside a magnetic field of 8T and was achieved in less than twenty minutes.

In the drop casting deposition, it was observed that inside the magnetic field the crystals are aligned perpendicularly to the direction of the magnetic field despite the fast crystallization. The distribution of crystals also appears more uniform and regular on the surface, moreover they tend to form less clusters (see figure 9).

Depositions by antisolvent vapor diffusion emphasize what observed before. The size of the crystals seems affected by the magnetic field as they appear bigger and longer than the ones obtained outside the magnetic field, and also the morphology tend to be more homogeneous and regular (see figure 3). The coherent orientation of the crystals in the samples deposited inside the magnetic field can be easily appreciated using the polarized light since most of the deposited crystals extinguish and transmit the polarized light at the same angle (figure 4), that means that the exposed crystal faces are the same and oriented on the same direction.

The depositions obtained were analyzed by XRPD to characterise the crystal phases present. The use of high boiling solvent, as expected, favoured the deposition of mainly phase I even if phase II was always present (see figure 13). These preliminary studies suggest that the solvent has more effect on the polymorphic modification than the magnetic field. However, the diffraction patterns of the samples obtained inside the magnetic field possess a higher crystallinity (FWHM=0.05° inside the magnetic field, FWHM=0.06° outside) and higher intensity (see figure 5 and figure 12). Moreover, the better crystallinity allowed us to observe the presence of a crystalline form characterized by the peaks at 3.05° and 3.91° (see figure 5). Careful inspection of experimental diffractograms of different samples of NTE, the peak at 3.91° was observed also as polymorphic impurity in a bulk sample of phase II (see figure 11).

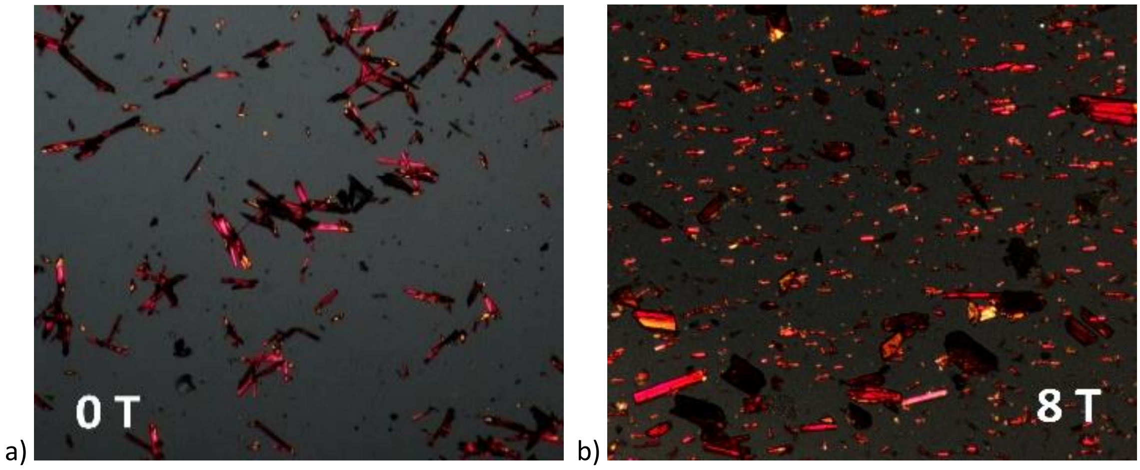

Figure 3. Comparison between the samples prepared by antisolvent vapour diffusion, outside (a) and inside (b) an 8T magnetic field; (photos taken with a 40x of magnification).

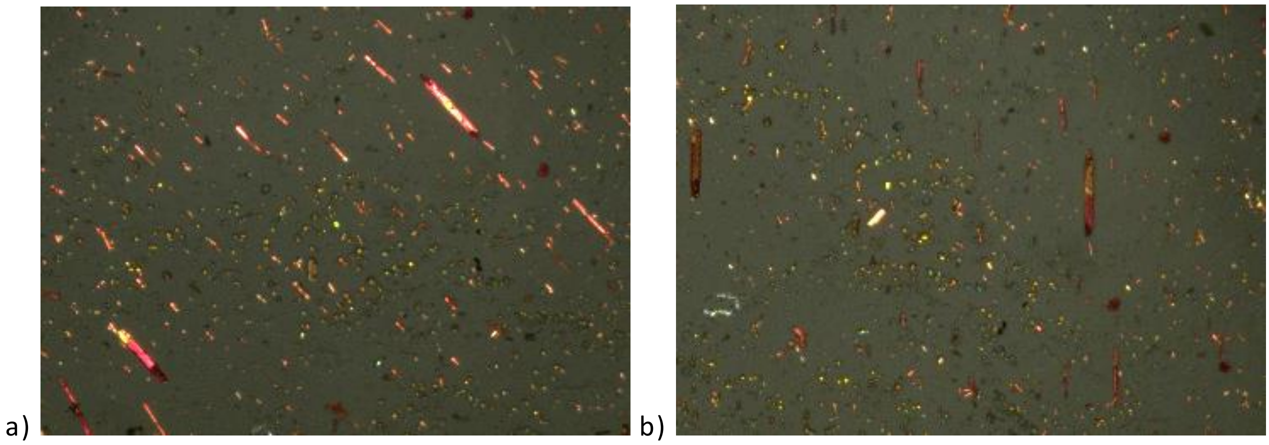

Figure 4. variation Variation of the transmitted light, a) starting position, b) rotation by 45°.

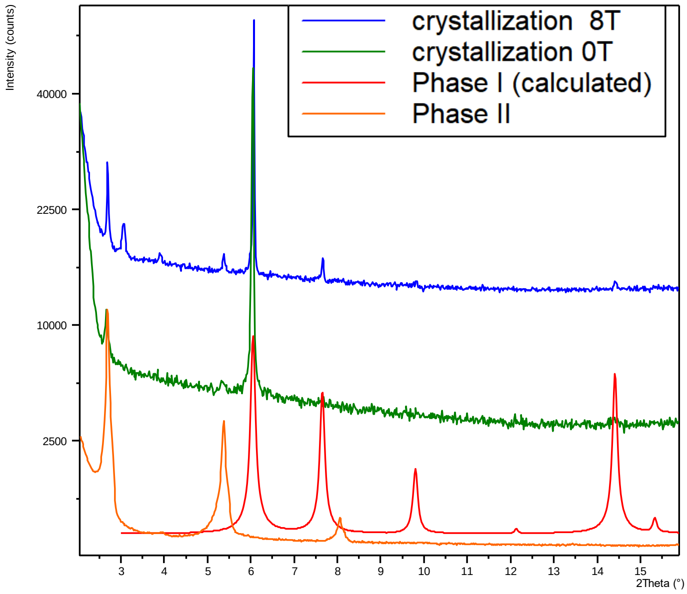

Figure 5. Powder diffractograms of the NTE deposition grown inside (blue) and outside (green) the magnetic field, compared with the calculated diffractograms of NTE phase I (red) and the experimental diffractogrram os of Phase II (orange), λ=1.5418 Å

CONCLUSION

In conclusion, it has been shown how a strong magnetic field can induce an orientation of the crystal domains of NTE during the thin deposit formation. This potentially could allow to control the direction of the crystallization with respect to the position of the substrate. It was also observed that use of an adequate magnetic field can boost the crystal size and the crystallinity of the material during the crystallization. Both aspects can significantly impact of the performances of optoelectronic devices, in particular on those of field effect transistors and light emitting transistors. Moreover, the proposed approach could also be exploited to obtain better crystals suitable for the structural determination as well as to detect elusive polymorphs which are hardly observed due to an intrinsic low crystallinity.

EXPERIMENTAL SECTION

Materials

The molecule NTE was synthesized by following the procedure already described procedures.[18] The powder diffractogram of phase I has been collected from a sample obtianed by slow evaporation from toluene solution while the diffractogram of phase IIlt has been collected from the raw material without further purifications or treatment after the synthesis, the diffractograms used for the indexing of the phase IIht was measured at high temperature (210°) since the phase II^{ht} transform in phase II^{lt} under 100°C.

Magnetic field

There were used two different magnets to obtan the magnetic field. For the bulk crystallization was used a horizontal magnetic field of 2 T generated by an electromagnet (MAGNET CHARACTERISTICS: a Tamagawa TM-WTF6215C). The depositions were performed inside a superconductive magnet (MAGNET CHARACTERISTICS: a Sumitomo Heavy Industry cryocooler-cooled superconducting magnet HF10) with a magnetic field of magnitude 8 T.

Thermal characterisation and optical microscopy

Differential scanning calorimetry

The analysis was performed with an instrument Perkin-Elmer PyrisDiamond DSC, in N_2 atmosphere and a scanning speed of 5°/min. The figure 6 reported the obtained curves. During the first heating are visible two exotermic events, the first at 142.3°C represent the transition from phase I to phase II^{ht} and then at 233.9°C the transition to the liquid crystal state. In the cooling curve 209.1°C there is the conversion fron liquid crystal to phase II, the different temperature is probably due to an hysteress effect, at 102.8°C is present a small exothermic peak, that is not the result to the transformation to phase I and is the transition between phase II^{ht} and phase II^{lt}. This event is completely reversible and is visible during the second heating at 107.4°C.

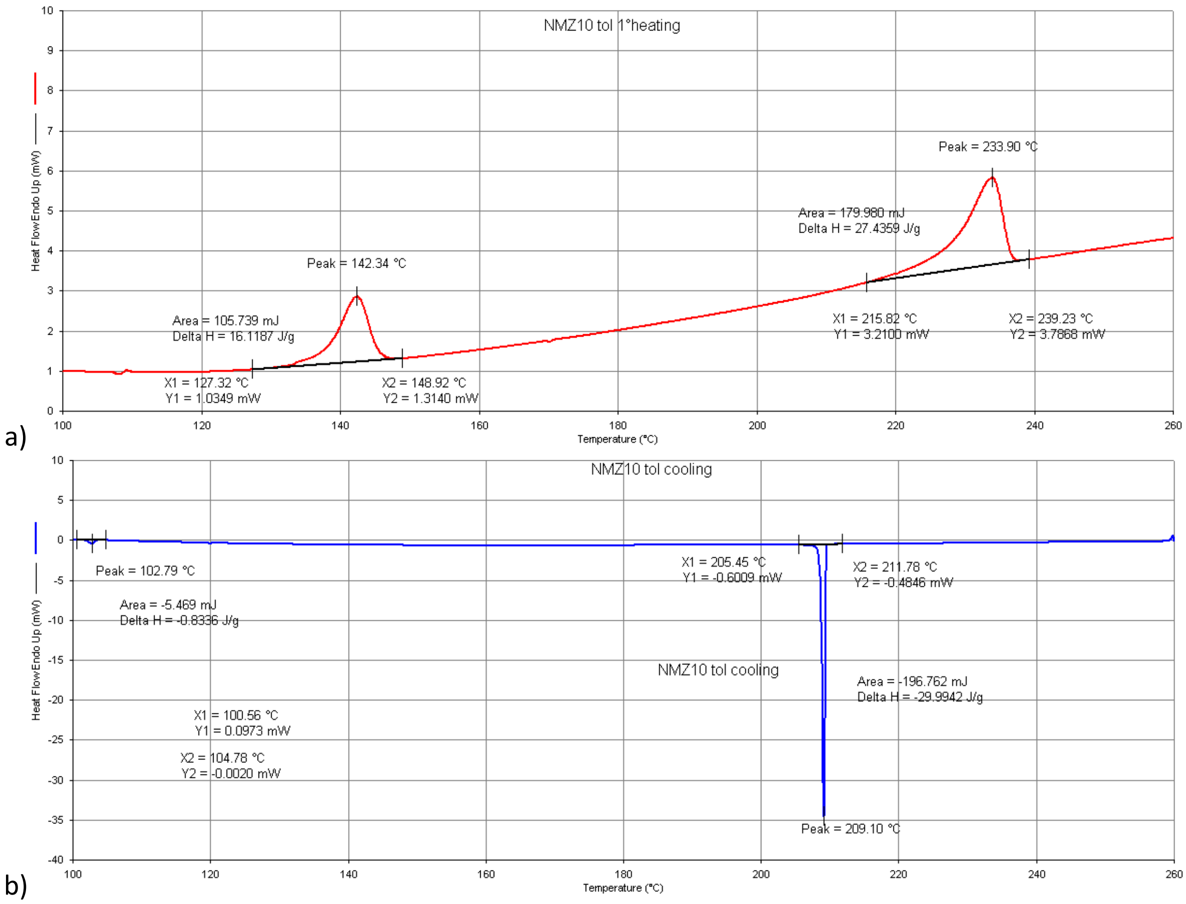

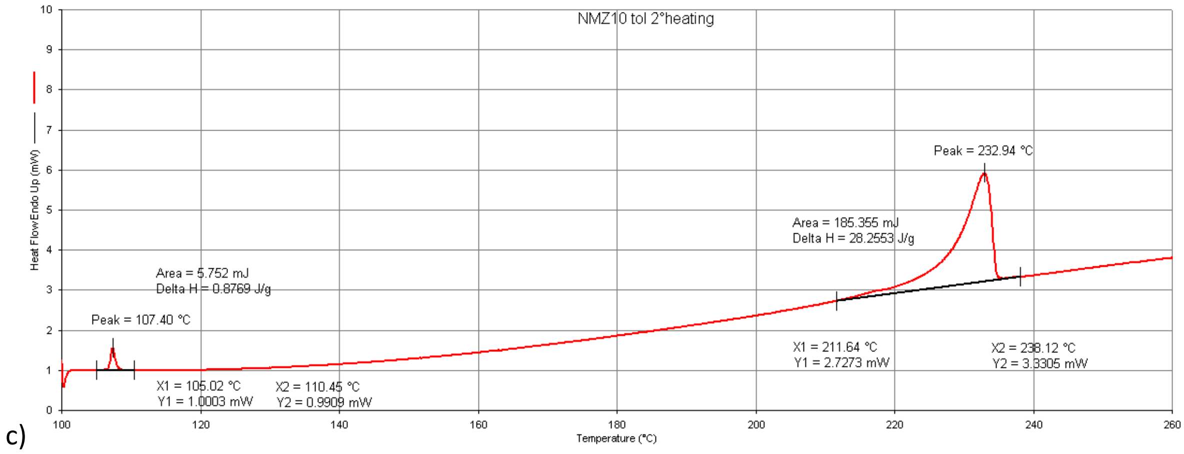

Figure 6. DSC of NTE form I; a) heating; b) cooling; c) second heating.

Hot-stage Microscopy

The analisys was performed using a microscope OLYMPUS BX41 equipped with a VISICAM 5.0 camera and a system for the temperature control Linkam TMS 94. The photos were taken under polarized light (figure 7) to underline the modification due to solid state transition, with a 40x magnification. After the thermal characterisation it was proposed an hypothetical diagram of the phases free energies. The diagram reflects the features of the enantiotropic transitions since all the transformations are plausibly enantiotropic. The transition from phase I to phase II^{ht} should be reversible from a thermodinamic point of view, but this event doesn’t take place probably for kinetic reasons.

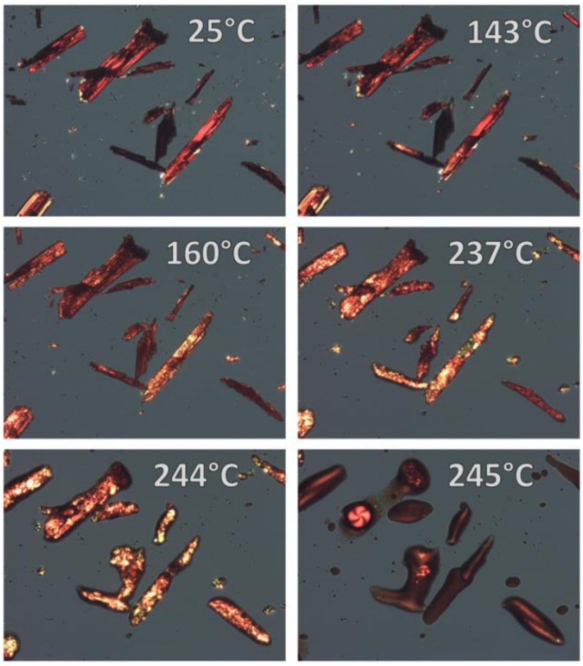

Figure 7. Hot-stage microscopy of NTE crystals of phase I

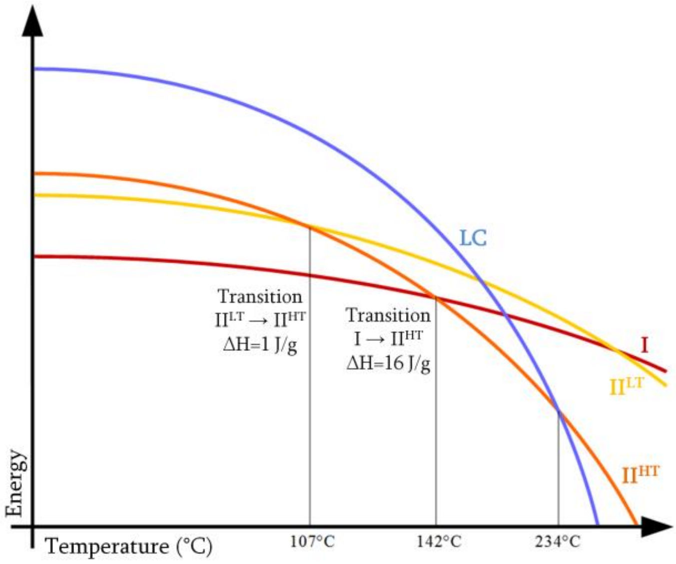

Figure 8. Hypothetical free energy surfaces of I, II^{LT}, II^{HT} polymorphs and liquid crystal of NTE.

Optical microscopy

The photos of the oriented crystal deposition were taken with a microscope OLYMPUS BX41 equipped with a NIKON DS-Fi3 camera with a 40x magnification.

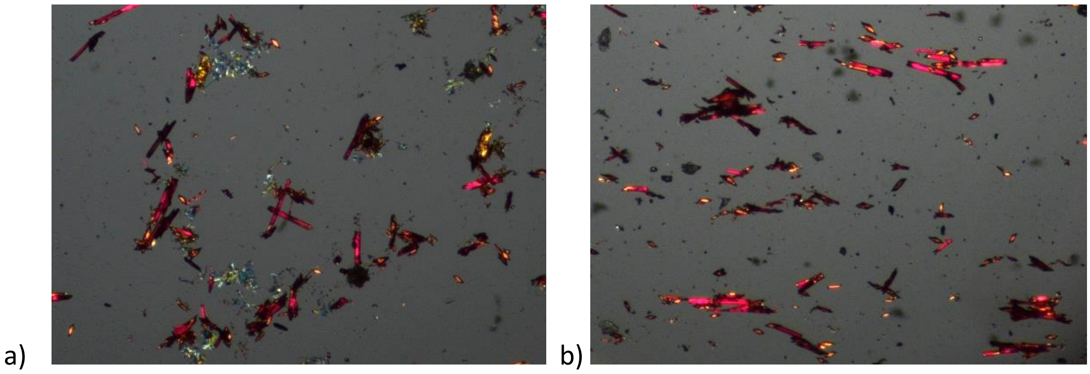

Figure 9. Comparison between the samples prepared by solvent evaporation from toluene solution, outside (a) and inside (b) an 8T magnetic field.

Diffraction and structural data

Single crystal X-ray Diffraction

Single Crystal Xray Diffraction, (SCXD), were performed on an Oxford Xcalibur S diffractometer with Mo-Kα radiation, λ= 0.71073 Å, and monochromator graphite at room temperature.

SHELX97[21] was used for structure solution and refinement based on F^2. The Non-hydrogen atoms were refined anisotropically. Hydrogen atoms bound to carbon atoms were added in calculated positions. The program Mercury[22] was used for all graphical representations and for the calculated powder pattern.

Table 1. Crystallographic data for three crystal forms of NTE

	Phase I (outside magnetic field)	Phase I (inside magnetic field: 2 T)	Phase II^{LT}	Phase II^{HT}
Chemical formula	$C_{34} H_{34} N_2 O_4 S_4$			
Formula Mass	662,9048 g/mol			
Crystal System	Triclinic	Triclinic	Monoclinic	Monoclinic
a/Å	4.8416(6)	4.8212(1)	33.814(4)	33.325(1)
b/Å	11.7738(1)	11.7376(2)	5.5090(3)	5.5886(1)
c/Å	14.6814(2)	14.6348(2)	18.711(1)	19.300(1)
α/°	89.145(1)	89.031(1)	90	90
β/°	83.362(1)	83.402(1)	76.723(7)	91.865(7)
γ/°	78.729(1)	78.878(2)	90	90
Volume/ Å^3	815.23(2)	807.2(3)	3392.3(5)	3592.5(3)
Temperature	RT	RT	RT	210°C
Space group	P-1	P-1	P2$_1$/c	P2$_1$/c
Syn / anti disorder	33.5% / 66.5%	32.7% / 67.3%	/	/
R$_1$	0.0988	0.0695	/	/
R$_2$ (all data)	0.1569	0.1274	/	/
Chi^2	1.167	1.035	/	/
Mosaicity (e$_3$)	2.55°	1.77°	/	/
R$_{wp}$	/	/	0.0565	0.0458

Synchrotron X-ray powder diffraction

Synchrotron radiation-XRPD measurements of NTE were performed at the Swiss Light Source (SLS) Material Science (MS) Powder Diffraction (PD) end station with a nominal photon energy of 16 keV. Fine Si640D NIST standard refinement returned a wavelength of 0.775375(2) Å and a residual zero error of −0.0253(4) 2θ. Data were collected with a 1D Mythen II detector[23] in the range of 2–120° 2θ with an intrinsic step size of 0.0036° (2θ). Samples were loaded in glass capillaries with a diameter of 0.5 mm and spun at 4 Hz during the measurement. Multiframing data were recorded in transmission with an exposure time of 5 seconds to avoid radiation damage; the raw data were then individually inspected before being merged together and flat field corrected.

At the syncrotron facility were also performed some difraction measurement at variable temperature with the use of a blower for the heating process.

Variable temperature X-ray powder diffraction

A sample of NTE phase I where analysed via X-ray powder diffraction at variable temperature (figure 10). In the patterns collected is clearly visible the transition from phase I to phase II between 110°C and 150°C. There are clearly some differences in the patterns of phase II collected at high and low temperature and in fact as the result of the indexing of the diffractograms obtained at room temperature (25°C) and at 210°C there were obtained two different crystal cells (table 1), corresponding respectively to phase II^{lt} and phase II^{ht}. The differences in the crystal cells are not due to a normal thermal expansion effect since some variations (expecially in the beta angle) are too marked. The patterns were indexed with TOPAS5 and the best crystal cell obtained was refined with a Pawley refinement.

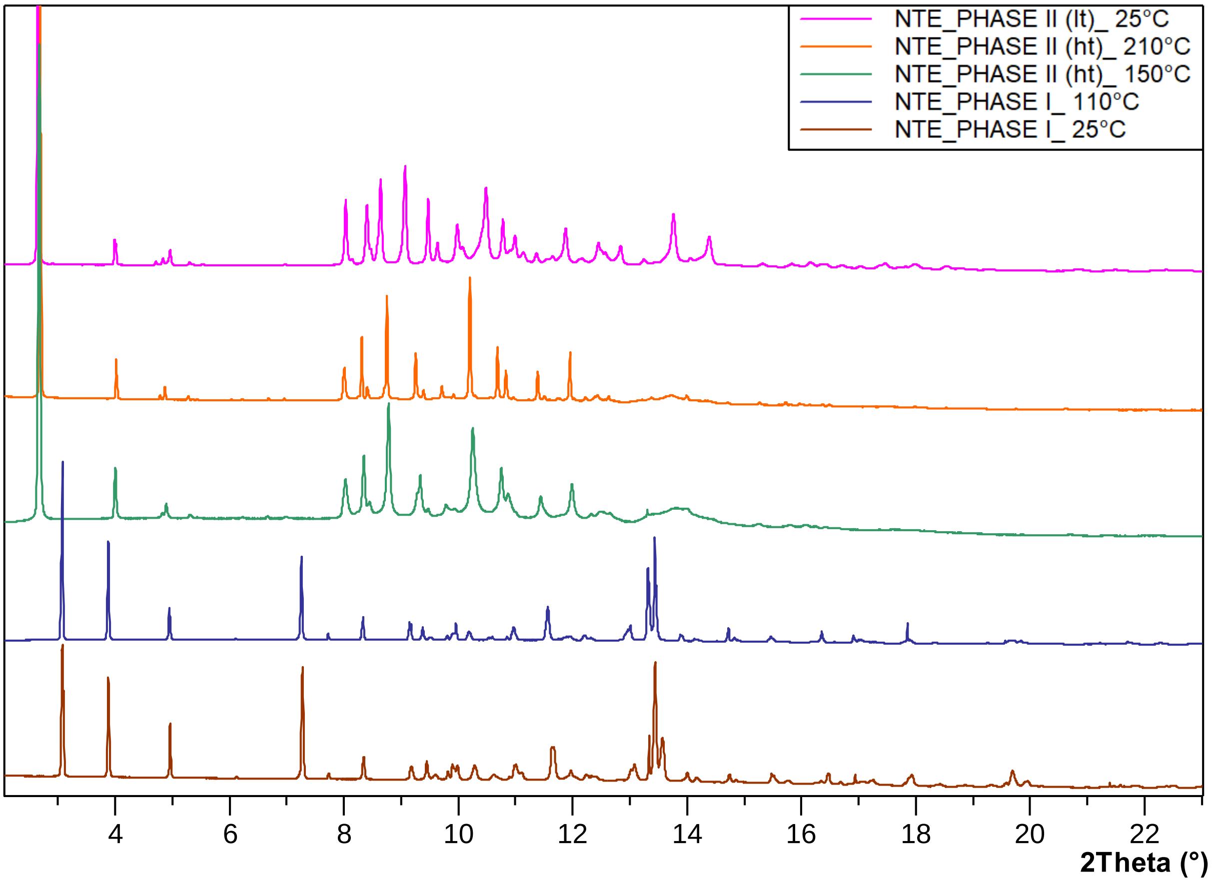

Figure 10. Powder diffractograms of a sample of NTE phase I collected at different temperature, λ= 775375(2) Å

X-ray powder diffraction

The data were collected in open air in Bragg–Brentano geometry using Cu-Kα radiation (λ=1.5418 Å) without a monochromator. X-ray powder diffractograms were collected in the 2θ range of 2.2°–44° using a Panalytical X'Pert PRO automated diffractometer equipped with an X'Celerator, with a counting time of 50 s, step size 0.0167°, soller slit=0.04 rad, anti-scatter slit=1/4°, divergence slit=1/8°.

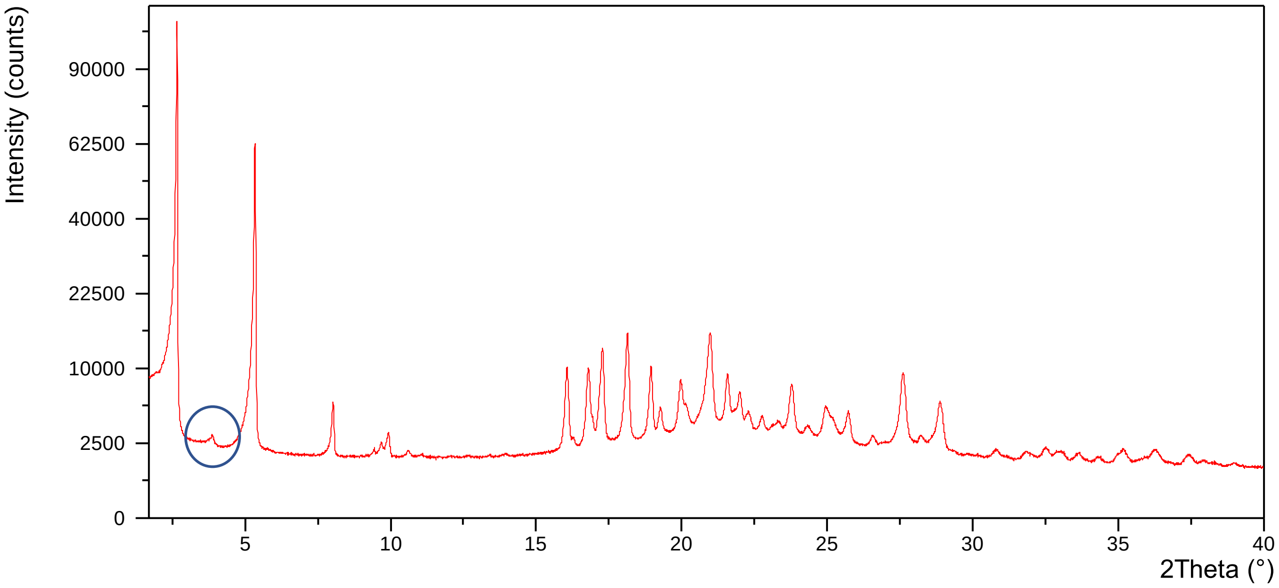

Figure 11. Powder diffractograms of a sample of NTE phase II^{lt}, Cu-Kα radiation

X-ray powder diffraction of deposited samples

The data were collected in Bragg–Brentano geometry using Cu-Kα radiation without a monochromator. The diffractograms were collected in the 2θ range of 2.2°–16° using a Panalytical X'Pert PRO automated diffractometer equipped with an X'Celerator detector, with a counting time of 150 s, step size 0.0167°, soller slit=0.04 rad, anti-scatter slit=1/8°, divergence slit=1/16°.

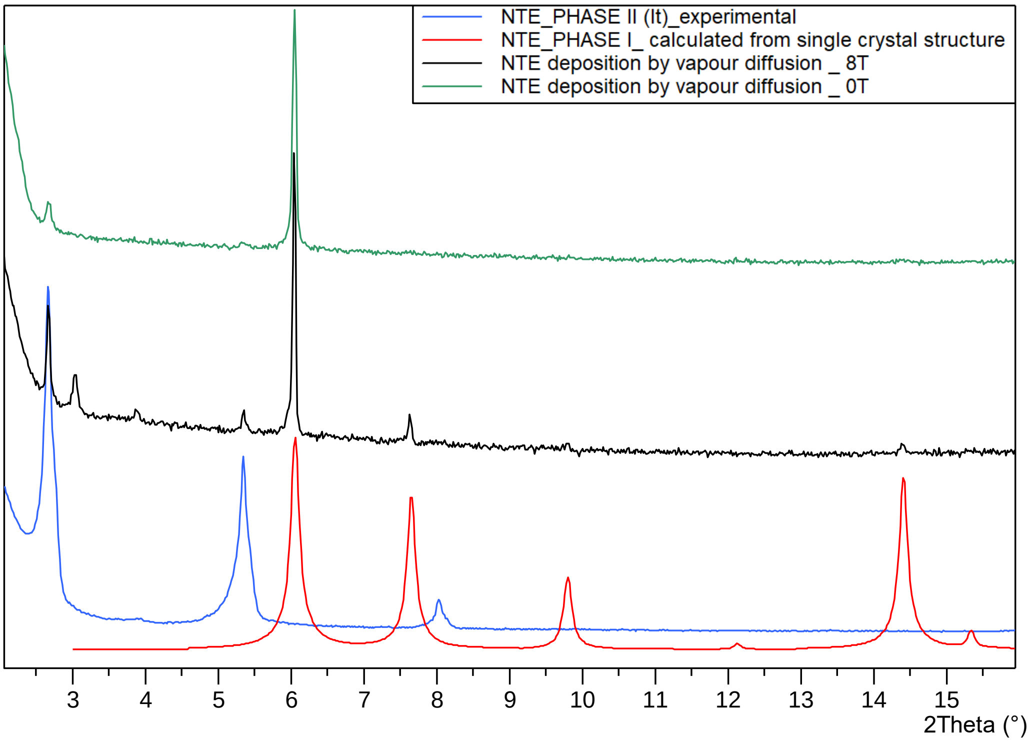

Figure 12. Powder diffractograms of the NTE deposition grown outside the magnetic field (green), compared with the calculated diffractograms of NTE phase I (red) and the experimental diffractogram of Phase II (blue), λ=1.5418 Å

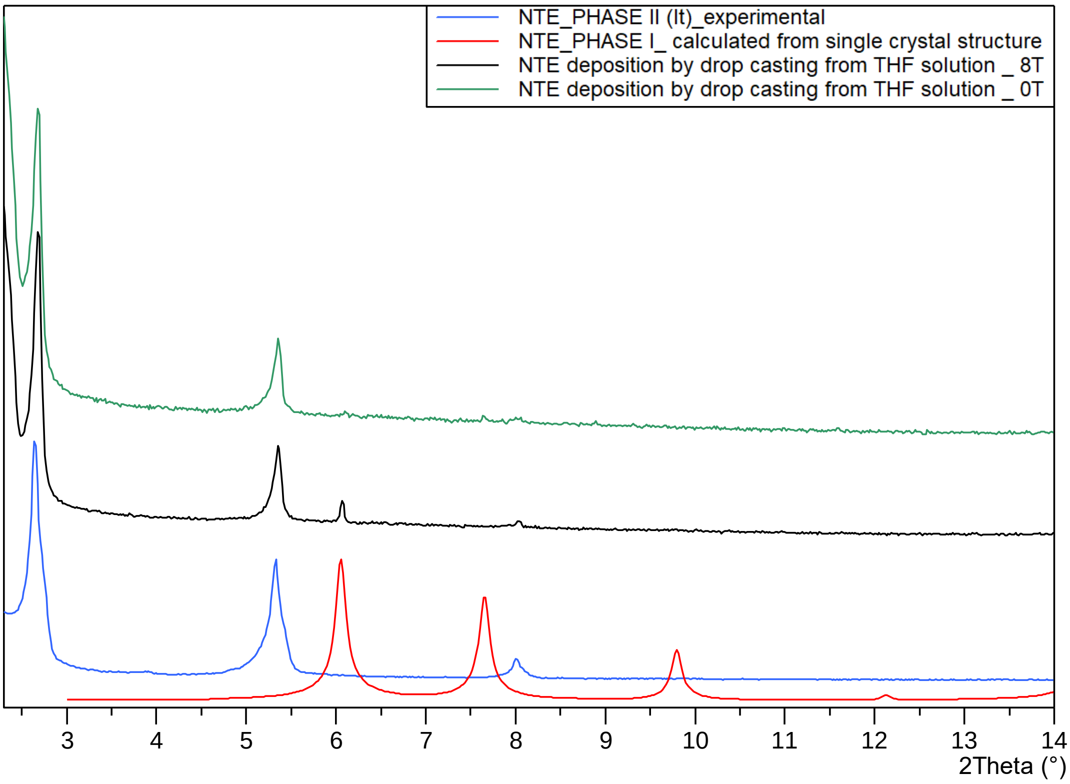

Figure 13. Powder diffractograms of the NTE deposition grown outside the magnet (green), compared with the calculated diffractograms of NTE phase I (red) and the experimental diffractogrram os Phase II (blue), λ=1.5418 Å

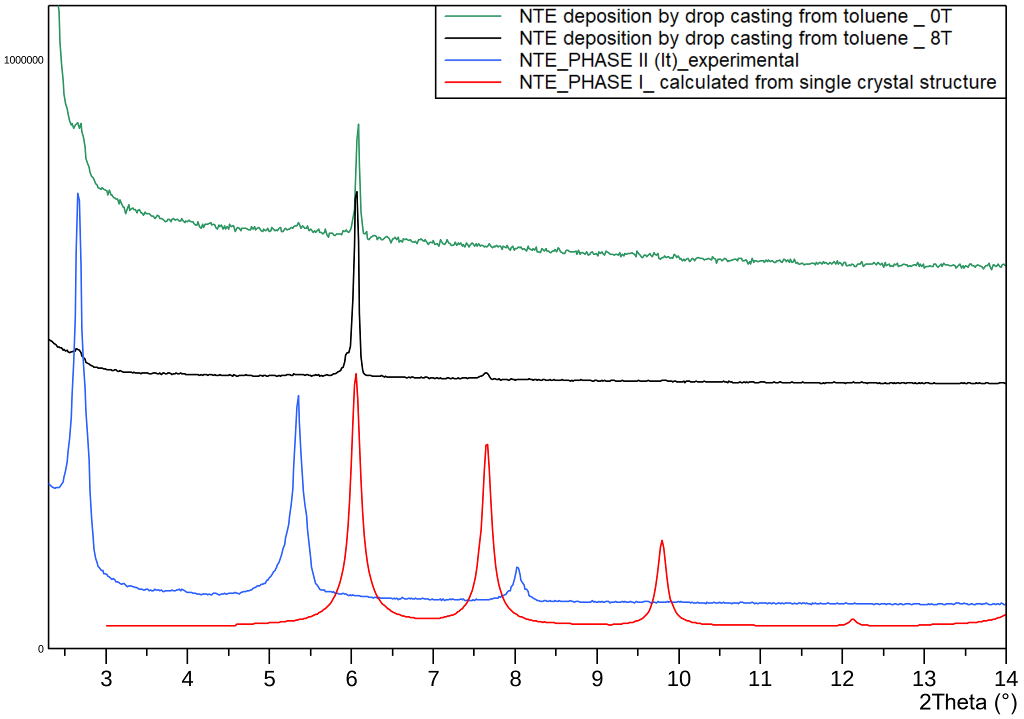

Figure 14. Powder diffractograms of the NTE deposition grown outside the magnet (green), compared with the calculated diffractograms of NTE phase I (red) and the experimental diffractogram os Phase II (blue), $\lambda=1.5418$ Å

REFERENCES

(1) Wang, C.; Dong, H.; Hu, W.; Liu, Y.; Zhu, D. Semiconducting π-Conjugated Systems in Field-Effect Transistors: A Material Odyssey of Organic Electronics. *Chem. Rev.* **2012**, 112 (4), 2208–2267.

(2) Chung, H.; Diao, Y. Polymorphism as an Emerging Design Strategy for High Performance Organic Electronics. *Journal of Materials Chemistry C*. Royal Society of Chemistry, **2016**, pp 3915–3933.

(3) Jacobs, I. E.; Cendra, C.; Harrelson, T. F.; Bedolla Valdez, Z. I.; Faller, R.; Salleo, A.; Moulé, A. J. Polymorphism Controls the Degree of Charge Transfer in a Molecularly Doped Semiconducting Polymer. *Mater. Horizons* **2018**, 5 (4), 655–660.

(4) Benvenuti, E.; Gentili, D.; Chiarella, F.; Portone, A.; Barra, M.; Cecchini, M.; Cappuccino, C.; Zambianchi, M.; Lopez, S. G.; Salzillo, T.; et al. Tuning Polymorphism in 2,3-Thienoimide Capped Oligothiophene Based Field-Effect Transistors by Implementing Vacuum and Solution Deposition Methods. *J. Mater. Chem. C* **2018**, 6 (21), 5601–5608.

(5) Kotsuki, K.; Obata, S.; Saiki, K. Self-Aligned Growth of Organic Semiconductor Single Crystals by Electric Field. *Langmuir* **2016**, 32 (2), 644–649.

(6) Jeon, H.-G.; Kim, J.-J. Magnetic Field Induced Grain Growth of Perylene Polycrystalline Films. *Org.*

Electron. **2010**, 11 (11), 1723–1728.

(7) Tabata, K.; Sasaki, T.; Yamamoto, Y. Magnetic-Field-Induced Enhancement of Crystallinity and Field-Effect Mobilities in Phthalocyanine Thin Films. *Appl. Phys. Lett.* **2013**, 103 (4), 043301.

(8) Tabata, K.; Yamamoto, Y. Enhancement of Grain Size and Crystallinity of Thin Layers of Pentacene Grown under Magnetic Field. *Thin Solid Films* **2016**, 603, 408–412.

(9) Potticary, J.; Terry, L. R.; Bell, C.; Papanikolopoulos, A. N.; Christianen, P. C. M.; Engelkamp, H.; Collins, A. M.; Fontanesi, C.; Kociok-Köhn, G.; Crampin, S.; et al. An Unforeseen Polymorph of Coronene by the Application of Magnetic Fields during Crystal Growth. *Nat. Commun.* **2016**, 7 (May), 11555.

(10) Yin, D.-C. Protein Crystallization in a Magnetic Field. *Prog. Cryst. Growth Charact. Mater.* **2015**, 61 (1), 1–26.

(11) Surade, S.; Ochi, T.; Nietlispach, D.; Chirgadze, D.; Moreno, A. Investigations into Protein Crystallization in the Presence of a Strong Magnetic Field. *Cryst. Growth Des.* **2010**, 10 (2), 691–699.

(12) Gavira, J. A.; García-Ruiz, J. M. Effects of a Magnetic Field on Lysozyme Crystal Nucleation and Growth in a Diffusive Environment. *Cryst. Growth Des.* **2009**, 9 (6), 2610–2615.

(13) Kimura, F.; Oshima, W.; Matsumoto, H.; Uekusa, H.; Aburaya, K.; Maeyama, M.; Kimura, T. Single Crystal Structure Analysis via Magnetically Oriented Microcrystal Arrays. *CrystEngComm* **2014**, 16 (29), 6630–6634.

(14) Tsuboi, C.; Aburaya, K.; Kimura, F.; Maeyama, M.; Kimura, T. Single-Crystal Structure Determination from Microcrystalline Powders (∼5 Mm) by an Orientation Attachment Mountable on an in-House X-Ray Diffractometer. *CrystEngComm* **2016**, 18 (14), 2404–2407.

(15) Tsuboi, C.; Kimura, F.; Tanaka, T.; Kimura, T. Single-Crystal X-Ray Diffraction Analysis of Microcrystalline Powders Using Magnetically Oriented Microcrystal Suspensions. *Cryst. Growth Des.* **2016**, 16 (5), 2810–2813.

(16) Melucci, M.; Zambianchi, M.; Favaretto, L.; Gazzano, M.; Zanelli, A.; Monari, M.; Capelli, R.; Troisi, S.; Toffanin, S.; Muccini, M. Thienopyrrolyl Dione End-Capped Oligothiophene Ambipolar Semiconductors for Thin Film- and Light Emitting Transistors. *Chem. Commun.* **2011**, 47 (43), 11840–11842.

(17) Favaretto, L.; Zambianchi, M.; Lopez, S. G.; Mazzanti, A.; Zanardi, C.; Seeber, R.; Gentili, D.; Valle, F.; Benvenuti, E.; Muccini, M.; et al. Synthesis and Investigation on Processing-Depending Polarized Fluorescence Emission in Thin-Films of 2,2′-([2,2′-Bithiophene]-5,5′-Diyl)Bis(5-Octyl-4-Phenyl-4: H -Thieno[2,3- c] Pyrrol-6(5 H)-One). *J. Mater. Chem. C* **2017**, 5 (39), 10320–10331.

(18) Zambianchi, M.; Favaretto, L.; Durso, M.; Bettini, C.; Zanelli, A.; Manet, I.; Gazzano, M.; Maini, L.; Gentili, D.; Toffanin, S.; et al. Synergic Effect of Unsaturated Inner Bridges and Polymorphism for Tuning the Optoelectronic Properties of 2,3-Thieno(Bis)Imide Based Materials. *J. Mater. Chem. C* **2015**, 3 (1), 121–131.

(19) Maini, L.; Gallino, F.; Zambianchi, M.; Durso, M.; Gazzano, M.; Rubini, K.; Gentili, D.; Manet, I.; Muccini, M.; Toffanin, S.; et al. Chemical Design Enables the Control of Conformational Polymorphism in Functional 2,3-Thieno(Bis)Imide-Ended Materials. *Chem. Commun.* **2014**, 51 (11), 2033–2035.

(20) Cappuccino, C.; Mazzeo, P. P.; Salzillo, T.; Venuti, E.; Giunchi, A.; Della Valle, R. G.; Brillante, A.; Bettini, C.; Melucci, M.; Maini, L. A Synergic Approach of X-Ray Powder Diffraction and Raman Spectroscopy for Crystal Structure Determination of 2,3-Thienoimide Capped Oligothiophenes. *Phys. Chem. Chem. Phys.* **2018**, 20 (5), 3630–3636.

(21) Sheldrick, G. M. SHELX97. SHELX97 **1997**, University of Göttingen, Germany.

(22) Macrae, C. F.; Bruno, I. J.; Chisholm, J. A.; Edgington, P. R.; McCabe, P.; Pidcock, E.; Rodriguez-Monge, L.; Taylor, R.; van de Streek, J.; Wood, P. A. Mercury CSD 2.0 – New Features for the Visualization and Investigation of Crystal Structures. *J. Appl. Crystallogr.* **2008**, 41 (2), 466–470.

(23) Bergamaschi, A.; Cervellino, A.; Dinapoli, R.; Gozzo, F.; Henrich, B.; Johnson, I.; Kraft, P.; Mozzanica, A.; Schmitt, B.; Shi, X. The MYTHEN Detector for X-Ray Powder Diffraction Experiments at the Swiss Light Source. *J. Synchrotron Radiat.* **2010**, 17 (5), 653–668.

CHAPTER 6: ONE MOLECULE, FOUR COLOURS, DISCOVERING THE POLYMORPHISM OF THIENO(BIS)IMIDE DERIVATIVES

The TI molecule described in this work presents one of the most interesting and complex polymorphic system of the TI family, with very impressive differences in the photophysical behavior. Computational chemistry experts were involved, in order to study and define the possible relationship between the crystal structure and photophysical properties, as well as conductive properties, of the different crystal phases.

I performed the structural characterization as well as the study on the polymorphism. The solid state transitions between the different polymorphs were investigate by hot-stage microscopy and variable-temperature X-ray diffraction.

Prof. Fabrizia Negri and Dr. Sofia Canola performed the quantomechanical calculations dedicated to the modelling of optical properties and charge transport.

ABSTRACT

The crystallization of the *2,2'-(5,5'-(Ethyne-1,2-diyl)bis(thiophene-5,2-diyl))bis(5-hexyl-4H-thieno[2,3-c]pyrrole-4,6(5H)-dione),* hereafter NTA, in different solvents and/or condition yielded to the identification of five different polymorphs which are characterized by impressive differences in the photophysical behaviour. Phase I, phase II, phase III and phase IV are characterized by a yellow, green, red and orange emission under illumination with 365 nm light. The crystal structures of phase II and III were determined by SCXRD. Phase II is characterized by the elongated molecules which lie parallels to each other in layers and hence by the presence of a long axis in the cell parameters. The two thienoimide-thiophene systems do not lay in the same plane which is consistent with the higher energy emission. In phase III, the NTA molecules pile up and form columns with strong π-π interactions. The packing is consistent with the presence of red emission and the absence of a long axis in the cell parameters. The thermal characterization revealed that phase I, II, III converts into phase IV, which, upon melting, recrystallizes in the elusive phase V. Quantum-chemical studies were carried out to investigate optical and charge transport properties. Promising charge transport properties with a dominant n-type character were predicted, however the role of internal conformational disorder could influence the efficiency of charge transport.

INTRODUCTION

Light emitting semiconductors have been widely studied because their potential application in the optoelectronic field[1] and in particular multifunctional π-conjugated small molecules are experiencing a new revival as active component of field effect transistors (OFETs) and photovoltaic devices (OPVs) or as coadjutant of polymeric based devices.[2–4] In order to tune their luminescent or conductive properties, the organic chromophore can be finely tuned by introducing new functional groups which will mainly affect the properties of the isolated molecule but also influence packing in the condensed phase. Indeed, the luminescent properties of the bulk organic material are the result of a synergic effect of properties of the single entity and the molecular packing. For this reason polymorphic modifications are a valuable way to achieve the desirable electronic structure and to tune solid-state packing and physical properties.[5–12] We have focused our attention on the family of 2,3-Thienoimide ended oligomers which are gaining increasing attention due to the promotion of n-type and ambipolar charge transport properties.[2,13] This new class of materials is being tested as active layer in ambipolar light emitting transistors (OLETs), field-effect transistors (OFETs), and both as donor and acceptors in photovoltaic cells (OPV). It worth noting that the synthesis of these molecules involves several steps and that reduce the final yields, on the other hand, their propensity to have different polymorphs allow to widen the possibility of utilization of the molecules.

Moreover the theoretical studies on luminescent polymorphs supplies new physicochemical insight into the interactions between the molecules and allow a preliminary understanding of molecular structure/crystal structure luminescence properties.[14] Hence it is fundamental not only to detect the different crystal forms but also to determine their crystal structures. Crystal structure determination can be really challenging since the recrystallization technique to obtain crystals suitable for single crystal X-ray diffraction favours the thermodynamically stable polymorph, leaving unknown the other crystalline forms. Fortunately the development of direct space methods allows the structure determination from powder, also with conventional source or in presence of several degrees of freedom.[15] This method is getting more and more attention in the field of organic molecular crystals, in particular for active pharmaceutical ingredients, while in the field of organic molecular materials only few examples are reported.[16–20]

In this paper we will describe the polymorphic behaviour of a member of this molecular family, *2,2'-(5,5'-(Ethyne-1,2-diyl)bis(thiophene-5,2-diyl))bis(5-hexyl-4H-thieno[2,3-c]pyrrole-4,6(5H)-dione)* named NTA (figure 1). The characteristic feature of NTA is the presence of an acetilenic bridge as a spacer in the oligothiophenic backbone. This moiety was introduced because it intrinsically permits a great variability in the molecular conformation thanks to the relatively ease rotation around the triple bond, promoting the formation of different crystal forms in the solid state.

On this line, here we demonstrated the existance for NTA molecule of at least five different polymorphs with different luminescent properties. Herein, we characterized these polymorphs by combines experimental techniques complemented with modelling of the optical properties and charge transport properties.

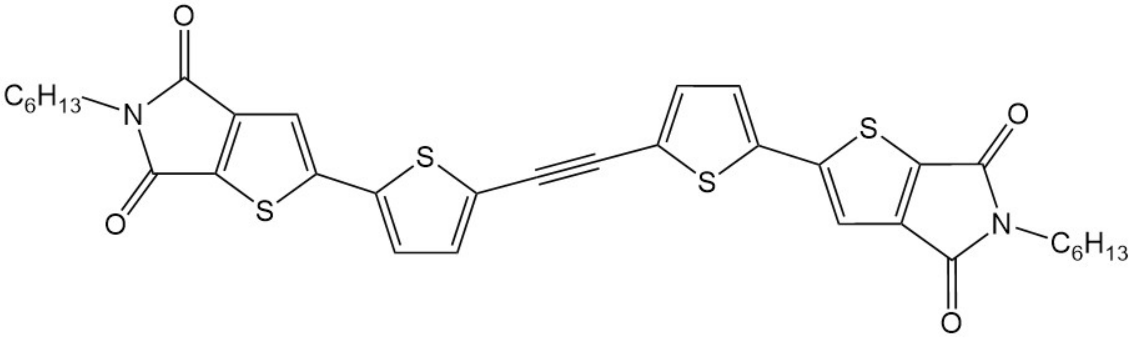

Figure 1. Scheme of the 2,2'-(5,5'-(Ethyne-1,2-diyl)bis(thiophene-5,2-diyl))bis(5-hexyl-4H-thieno[2,3-c]pyrrole-4,6(5H)-dione) called NTA.

In a previous work it was correlated the interring rotation with respect to unsaturated bridge with the existance of different polymorphs for a single molecue.[4] Here in we describe the thermal behaviour and the emission spectra of four polymorphs. We determined the crystal structure of two of them, so the experimental investigations are complemented with modelling of the optical properties and charge transport properties of the two polymorphs.

RESULTS AND DISCUSSION

Polymorphism

During our recrystallization experiments we observed the presence of at least four different polymorphs of NTA (figure 2), each one presenting a strong fluorescence and characterised by its own emission colour under UV light (365 nm). A fifth and elusive crystal forms appeared during the hot stage microscopy experiment at high temperature concomitantly with the melting point. Unfortunately, we were not able to isolate and characterize it.

The different crystalline forms have been numbered in the same order they have been found. Three of these crystalline forms were obtained from different types of crystallization and the fourth by thermic conversion from the others.

Recrystallization by solvent evaporation from toluene, xylene, chloroform and sichloromethane, of NTA yelds to yellow fibre-like crystals of phase I, with yellow emission under UV light. This phase was characterized by XRPD, since due to the shape and the dimensions, the crystals weren’t suitable for SCXRD. Phase II crystallises concomitantly with Phase I, and it was obtained only by solvent evaporation from toluene. Crystals of phase II are green/yellow plates with rhombohedral shape and show green emission under UV light. We were able to determine the structure by SCXRD but due to the low quantity obtained of this phase the others characterizations were prevented.

Small crystals of Phase III seldom appeared during early crystallizations of phase I. They are easily recognizable by their red colour. In later crystallization we obtained the pure phase by a fast adding of pentane (an antisolvent) into a concentrate solution of NTA in hot toluene. We managed to obtain single crystal suitable for SCXRD by vapour diffusion of pentane into a toluene solution. Phase III crystals have a needle-like shape with red emission under UV light. This phase has been characterized with both XRPD and with SCXRD.

Phase IV has not yet been obtained by crystallization but only by thermic conversion from the polymorphs I, II and III. It is characterized by orange emission under UV light. Until now we managed to obtain only the powder diffraction pattern, by diffraction measurement at variable temperature.

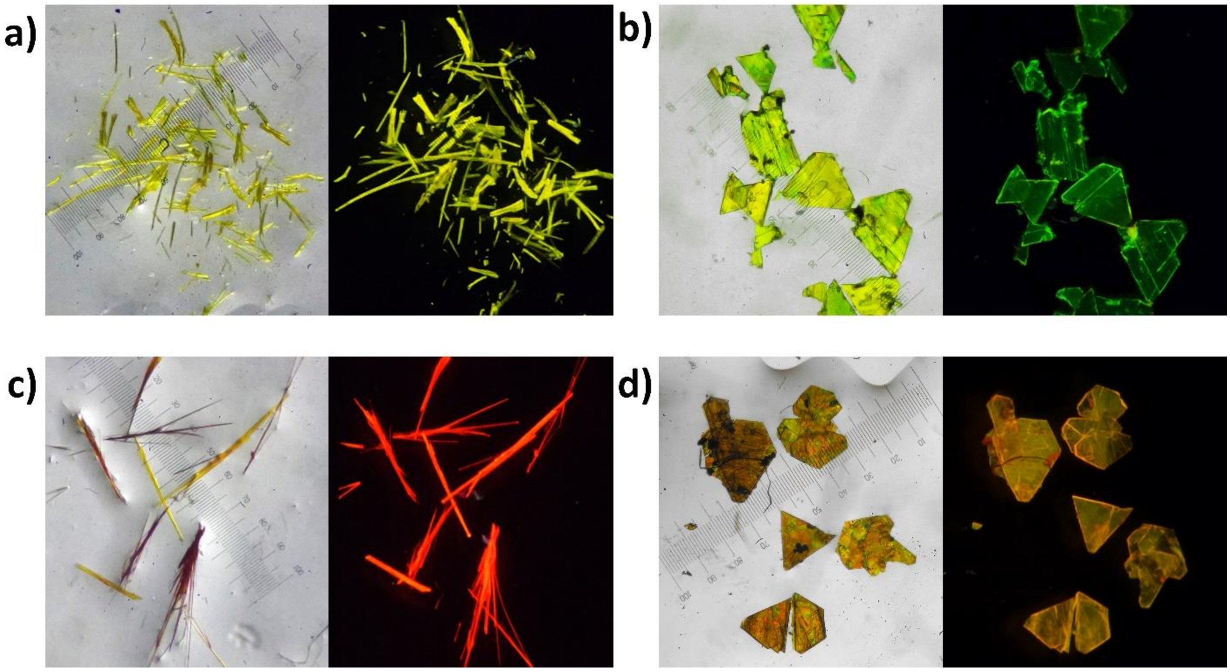

Figure 2. Photos of the different polymorphs of NTA taken by optical microscopy, transmitted light on the left and under UV light (365 nm) on the right; a) phase I, b) phase II, c) phase III, d) phase IV (obtained by thermal annealing of phase II) (Magnification 30xm, 30 ticks=1mm).

Thermal Properties

The behaviour upon thermal annealing was explored for all polymorphs by HSM under polirized light. In the case of phases I, II and III during the heating it was observed a solid state transition accompanied by variations in the emission colour under UV light. The transition is clearly visible because of the changes in the birefringence under polarized optical microscopy. In figure S1 it is possible to follow the transition Phase II and phase I to phase IV respectively at 150°C and 215°C (figure SI1b and SI1c). The transition is irreversible and by cooling form IV to room temperature the polymorph is retained as confirmed by the emission colour and the powder pattern (figure SI6). The figure SI2 shows the transition of a phase II crystal, first to phase IV (figure SI2b), and then in phase V (figure SI2d). During thew melting of the phase IV, different crystals appear inside the melt phase, growing and replacing the other polymorph. These crystals are stable during the cooling.

When the HSM was performed on a crystal of form II with dimension of 2.5 mm, it was possible to follow the front of the conversion which started at 150°C (figure 3b). In this case, during the conversion the crystal shows only few visible fractures on the surface and the transition seems to be single crystal to single crystal. Even in this case the transition appears irreversible and the colour of the crystal and the emission has changed from green to orange.

Phase III underwent to phase transition at 120°C which can be easily detected by the cracking of the crystals and the change of the colour of transmitted light (figure 4). The fusion started at 228°C followed by a recrystallization in which smalls crystals of a new phase growth into the melted material around 230°C, the complete fusion take place at 233°C.

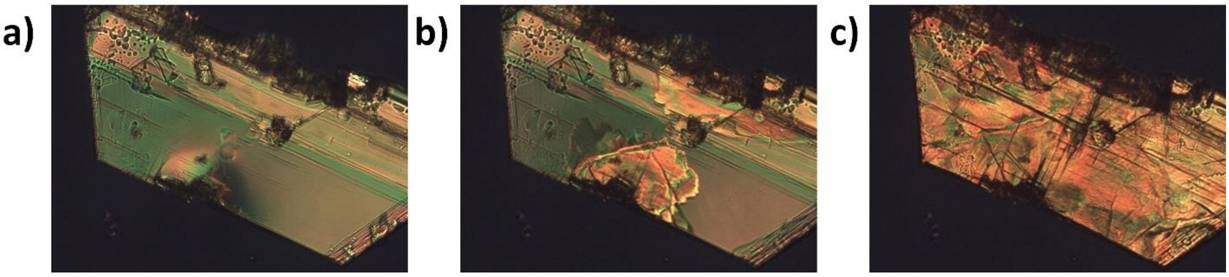

Figure 3. HSM photos of a phase II crystal under polarized light; a) 25°C, b) 150°C, transition beginning, c) 153°C, transition ending.

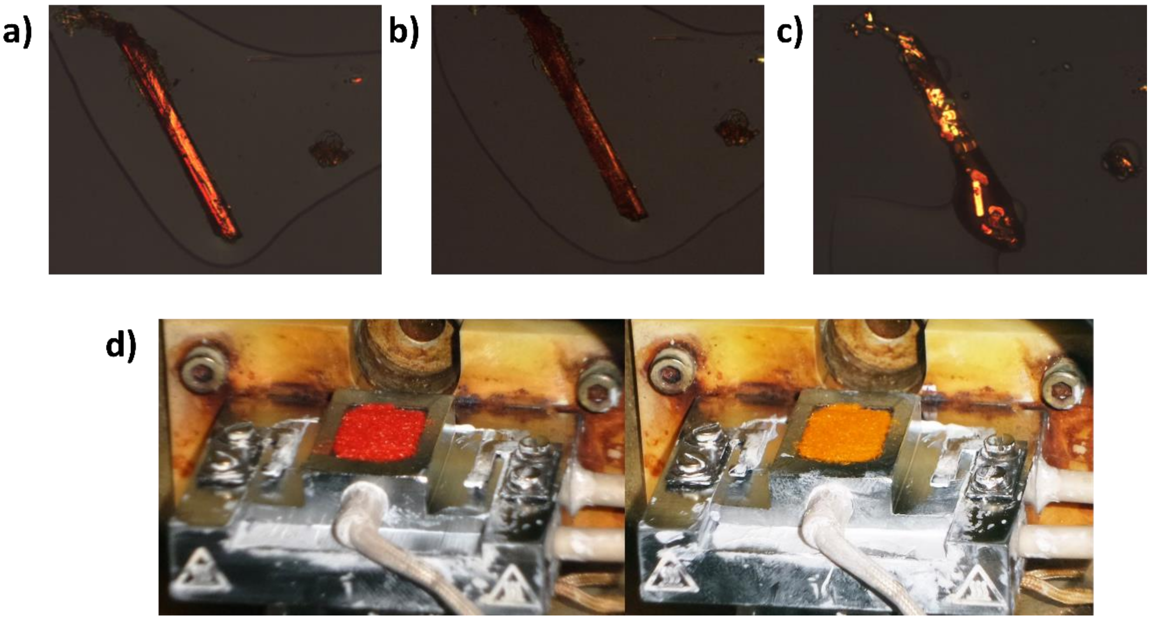

Figure 4. HSM analysis of a phase III crystal under polarized light; a) 50°C, b) 130°C, transition to phase IV, c) 231°C, melting and recrystallization of phase V; d) Color variation of the sample during the variable temperature x-ray diffraction measurements, from red of phase III to orange of phase IV.

Upon melting at temperature higher than 233°C the compound decomposes since the colour of the material turns brown and it does not emit under UV light.

The conversion of phase I and phase III into phase IV was confirmed by VT-XRPD (figure SI5 and SI6). Since in all transformations the final emission colour is orange and in all cases the melting is observed at the same temperature, we suppose that also phase II transform into phase IV upon heating.

Phase V is difficult to isolate and was observed only in the range 229-233°C, concomitantly with the melting point, upon melting it decomposed.

Crystal Determination

Phase II

Several crystals of phase II obtained by recrystallization of NTA in toluene have been tested for SCXRD and the best one was chosen for the analysis even if its dimension and the low crystallinity did not allow a complete data collection. The dimension of the crystal and the low crystallinity of the solid did not allow a complete data collection. The structure was resolved in the monoclinic space group C2/c with one molecule of NTA in the asymmetric unit (a=64.262(7) Å; b=5.6259(5) Å; c=18.487(2) Å; β=92.691(1)°; volume=6674.9(1) $Å^3$); the volume of the cell is consistent with the multiplicity of the space group, that is eight for C2/c. The thienoimide-thiophene-CC-thiophene-thienoimide portion (hereafter "molecular core") is not planar in fact the two halves of the core, separated by the triple bond, lay on two different planes (dihedral angle: 57°). The breaking of the planarity corresponds to a loss of conjugation, this may explain the blue-shift of the emission (as also demonstrated by model calculations, see below) compared to the other polymorphs of NTA and similar.[4] The sulphur atom of one thienoimide is disordered over two positions which was modelled with 70% anti conformation and 30% syn conformation (see figure 5a). The syn conformation is not unusual and it was already observed in thieno(bis)imide-ended materials.[21,22] The loss of planarity prevents a good overlap of the thiophenic cores and apparently the two halves of the core interact with different molecules to form an infinite ribbon of molecules linked together through π-π stacking. In the 3D packing these ribbons are flanked, connect through CH-π interaction, forming a herringbone motif. From the view along the b-axis, it can be noticed areas that contain only the thiophenic cores alternating with areas contain only alkyl chains. In these layers the alkyl chains do not form particularly strong interactions aside the Van der Waals forces and the carbon atoms are characterized by high thermal parameters, which causes a partial amorphization of the material, as it happens in polymers.

The presence of a long axis indicates that the molecules are prone to stay flanked, with a poor interdigitation, in order to form different layers, like in a “wafer”. This wafer-like structure is characterized by the presence of a long axis (64.262 Å as C cell and 32.254 Å), which is related to the length of the molecule as observed in other similar structure of TI ended oligomers. The obtained structure consists in layers containing only the aromatic cores alternate with layers containing only the alkyl chains. In the layers the aromatic cores are piled together through π- π stacking interactions while the alkyl chains are more flexible since no strong interactions occur between the carbon atoms. This degree of freedom of the alkyl chains permits a certain mobility and make difficult the determination of the exact position of the atoms, this feature is reflected in the relatively high thermal parameters of the alkyl carbons.

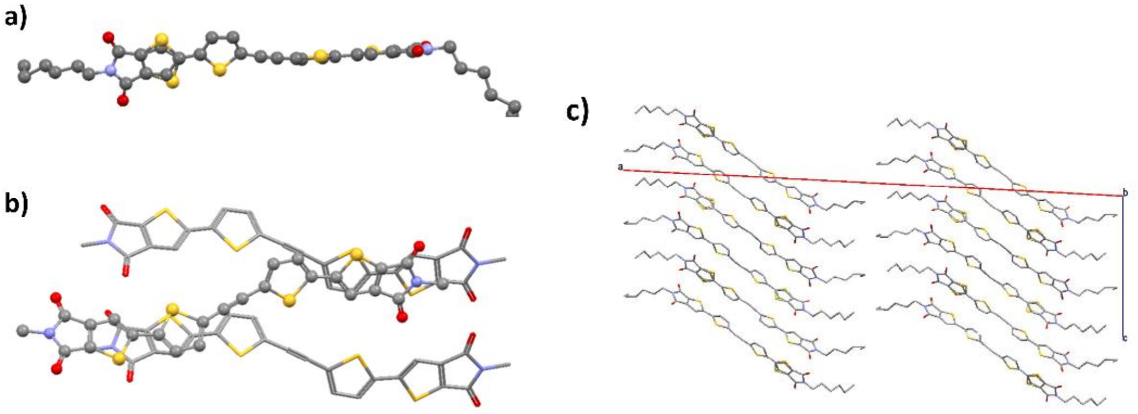

Figure 5. View of the symmetric unit of phase II, b) $\pi-\pi$ interaction among the NTA molecules (disorder and alkyl chains omitted for sake of clarity), packing view along b axis to highlight the alternation of layers rich of aromatic rings and layers containing only alkyl chains. In all figure H atoms omitted for sake of clarity.

Phase III

All the crystallization attempted yielded only very small crystals of phase III which prevented the possibility to obtain a complete data collection. The structure was resolved in the triclinic space group P-1 with one half molecule of NTA in the asimmetric unit (a=4,882(3) Å; b=11,846(6) Å; c=14,591(9) Å; α=89,80(5)°; β=83,89(5)°; γ=79,67(4)°); volume=821,64(6) Å^3); the triple bond is located on the inversion centre. The molecular core is planar as observed in the majority of thiophenic compounds (according to CSD). The lateral couple of thiophenes presents the disorder in the syn/anti isomerism which was refined for 72% in anti conformation and for 28% in syn conformation (see figure 6a). The alkyl chains are almost perpendicular respect to the aromatic ring which allow the molecules to piled in columnar stack through π–π stacking interaction (figure 6b). These columnar stacks are interdigitated each other in order to form C-H-O intermolecular interaction between the thienoimide oxygen and one hydrogen of a thiophene ring of an adjacent molecule.

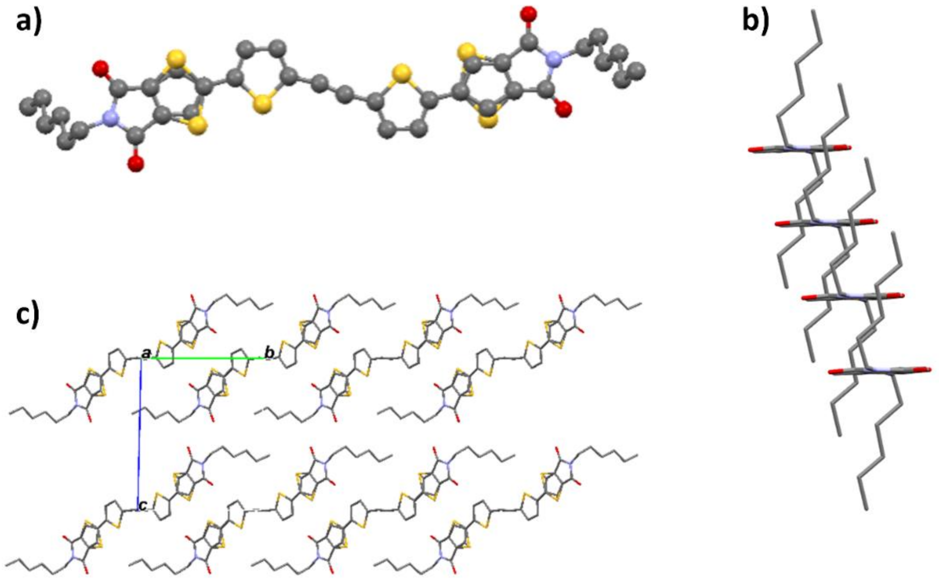

Figure 6. a) View of the molecular conformation of phase III, b) π–π interaction among the NTA molecules, c) packing view along a axis to show the interdigitation of the columnar staks of molecules. In all figure H atoms omitted for sake of clarity.

Powder Diffraction

We collected the XRPD pattern of phases I, III and IV; but not phase II since we manage to obtain only few crystals, not enough for powder diffraction. We performed variable temperature x-ray pawder diffraction of both phase I and phase III to confirm the solid state transition to phase IV.

To attempt crystal structure determination from powder we collected Phase I and Phase IV at synchrotron facility at PSI centre (Villigen, Switzerland). We collected phase I diffraction pattern Variable Temperature, as expected the diffraction pattern changed between 207°C and 212°C that correspond to the transition to the phase IV observed in the HSM (figure SI5). The powder pattern of phase I is characterized by a peak at low angle (d=32.875 Å) which suggests the presence of a long axis and hence a wafer-like structure. As observed in the other structures of thienoimide compounds, the interplanar distance of 32 suggests that the molecules are almost parallel to the molecular axis of the unit cell (being the molecular length of about 31.76 Å), with a scarse molecular interdigitation. Upon cooling no transition are observed. Interestingly, upon heating, the peaks of phase I appear dramatically sharper which suggests an increasing of the crystallinity of the sample (figure SI4). Similar behavior is observed in the polymers, where the high temperature allows the recrystallization of the amorphous part. In phase I, we speculate that the alkyl chains are disordered at RT while by increasing the temperature they are able to move themselves and reach more ordered positions[23,24]. We focused our attention to the pattern at 190°C which shows sharp and well resolved and we indexed it with a monoclinic C (base-centered) cell with a=25.220(2) Å; b=67.237(5) Å; c=5.6063(1) Å; β=113.58(3)°; and volume=8712.87(2) Å^3), however the quality of the diffraction pattern prevents the reliable attribution to a specific space group. The size of the cell is consistent with 2.5 independent molecules which correspond to at least 47 degrees of freedom, not considering the possible disorder of the S positions. The low diffraction power of the material and the number of degrees of freedom prevent the structural resolution from powder diffraction.

Unfortunately, we were not able to index the pattern obtained of phase IV. Conversion of phase III into phase IV was characterized by lab Variable Temperature XRPD. During the experiment it was observed a change in the diffraction pattern between 120 and 130°C, compatible with the value collected during the thermal annealing (approximately 120°C). The quality of lab data did not allow further investigation.

Photophysical Properties

Photoluminescence spectroscopy of NTE shows a structured emission profile for all crystal phases. Phase I and IV show almost superimposable profiles with a more intense peak located at about 550 nm a less intense peak at about 600 nm. A boad shoulder i salso visible at about 650 nm. Phase II shows a smilar profile with a more intense peak at 600 nm with respect to phases IV and II. For phase III an overall red shift with emission centered at about 625 nm.

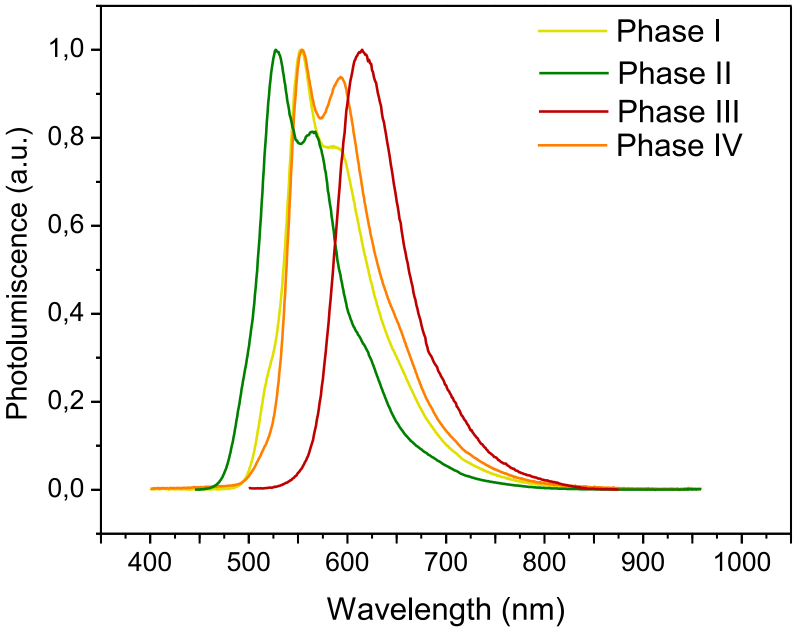

Figure 7. PL spectra of the different phases of NTE (phase I,II,IV λ_{exc}=325 nm, phase III λ_{exc}=470 nm)

Modelling Optical Properties and Charge Transport

To assist the interpretation of the spectroscopic properties observed for the different polymorphs of NTA and to model their charge transport properties, a quantum-chemical investigation was carried out. Electronic structure and optical properties were computed for the experimentally investigated thieno(bis)imide NTA featuring alkyl chains and on a model system featuring hydrogen atoms instead of alkyl substituents, hereafter labelled NTA-H. The model system was employed to model the optical properties of different conformers by evaluating excited electronic states and transition dipole moments as a function of molecular conformation. In addition to the optical properties, intra-molecular reorganization energies and intermolecular electron interactions governing charge transport were computed with quantum-chemical calculations and charge mobilities were estimated on the basis of kinetic Monte Carlo simulations as outlined in more detail in the Experimental section.

Excited states

The observed shift in the emission spectra of the different polymorphs can be traced back either to intra-molecular properties or inter-molecular interactions or both. To model the effect of the twisted structure determined experimentally for phase II on optical properties, we computed the excitation energy of the low lying excited electronic states of NTA-H (the three possible structural isomers AAA, SAA and SAS were considered) for three different conformations of the single CC bond adjacent to the triple bond (see Figure 8) corresponding to a dihedral angle of 0, 60 and 90 degrees. The observed emission clearly occurs from the lowest excited state (S_1) which is dominated by the (H→L) excitation (Figure 8). The computed excitation energies and oscillator strengths collected in Table S2 and Figure S9 show a blue shift for increasingly large twisting angles which compares well with the observed blue shifted emission of phase II, where the molecule is forced to be twisted by the packing, in contrast with phase III where the molecules are planar. Therefore we can conclude that the observed blue-shift of the luminescence of phase II is dominated by the intramolecular twisting.

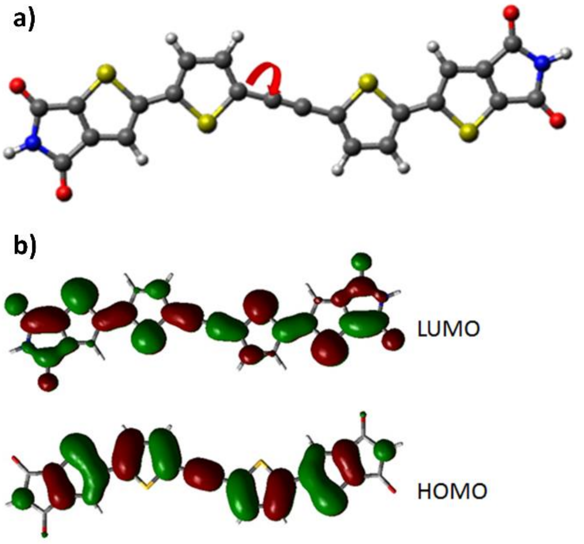

Figure 8 (a) Twisting of AAA-NTA-H and (b) frontier molecular orbitals computed at the B3LYP/6-31G* optimized geometry.

n-type and p-type charge transport

In molecular materials, where intermolecular interactions are relatively weak, the charge transport can be rationalized in terms of the non-adiabatic hopping mechanism[25] according to which charge transfer occurs in a dimer formed by two molecules with an efficiency determined by the magnitude of the rate constant. Reliable estimates of the charge transfer rate constants can be obtained using the Marcus Levich Jortner formulation[25,26] in which the reorganization energy associated with the transfer of charge between two molecules (essentially an intramolecular parameter) and the intermolecular electronic coupling (strongly influenced by packing) play an essential role. In a one-electron approximation the coupling can be computed between pairs of

HOMO/LUMO orbitals for p-type/n-type transport, respectively. The availability of the crystal structure of phase III and II enables the identification of the near-neighbors of a given molecule and their selection for the evaluation of electronic couplings. Because the crystal structure shows the presence of structural isomers of AAA and SAA type, in our modelling we considered pure crystals of the AAA and SAA isomers along with a mixed phase including both AAA and SAA molecules. The computed reorganization energy for the AAA and SAA structural isomers of NTA are in the range 0.26 – 0.31 eV with the larger values computed for the SAA isomer and for n-type charge carriers (see Table S4). These values are comparable to those of other n-type organic semiconductors such as NDI[27] or PBI[28,29] but are larger than those of the best p-type semiconductors such as pentacene.[30] Further analysis of the reorganization energies in terms of Huang-Rhys parameters allows to identify the quantum vibrational modes that most contribute to charge transfer (see Figure S11). Calculations show that the quantum correction involves a higher effective vibrational frequency for n-type conduction compared to p-type transport (see Table S5) owing to the contribution of low frequency vibrations assisting charge transfer in the latter case. This result, combined with the magnitude of electronic couplings (see below) favors the n-type charge transport.

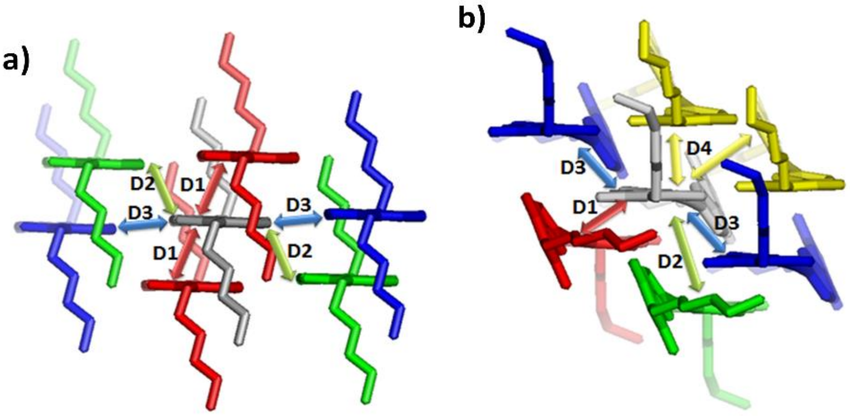

Figure 9. Schematic view of the charge pathways from the central grey molecule to the nearest neighbor molecules in phase III (a) and phase II(b) of AAA-NTA crystals. Colored arrows help to view the directionality of the charge pathways.

The electronic couplings of phase III are non-negligible only for charge transfer occurring between molecules that belong to a layer parallel to the *a,b* plane, while interactions between molecules in two different layers displaced along the *c* axis are negligible even if the molecules are strongly interdigitated. The electronic couplings and resulting rate constants (Table S6) are reflected in computed charge mobilities which show peculiar anisotropies in the *a,b* plane (see Figure S13 and Table S8). The p-type mobilities of the pure AAA, pure SAA and mixed AAA/SAA crystals show marked anisotropy with the largest values aligned along the *a* axis since the D1 charge pathway is directed along *a* and is by far the most efficient for holes. The magnitude of these mobilities is however small, owing to the modest electronic couplings. The n-type mobilities of the pure AAA, pure SAA and mixed AAA/SAA crystals are much larger than the p-type counterparts and show marked anisotropy determined by the directionality of the D1/D3 pathways (Figure 9, left). The n-type mobility of the mixed crystal is intermediate between those of the pure crystals and significantly larger than the p-type.

Because the layers (ribbons) formed by π-π stacked molecules are less interdigitated in phase II than in phase III, the absence of interactions between layers (ribbons) is not unexpected in this case and the largest couplings occur only for molecules π-π stacked (see Figure 9 right and Table S7). Each molecule is surrounded by six near-neighbors and the couplings are generally larger than those computed for phase III, especially for p-type transport. As a result, the p-type charge mobility is computed to be larger for phase II compared to phase III.

In summary, both phases display relevant charge mobilities with a preferential n-type transport whose efficiency is expected to be influenced also by the role of the low lying LUMO+1 orbital (Figure S10, Table S3) that is expected to contribute to charge transport.[31] Because the crystal structure is organized in layers of pi-stacked molecules, the charge transport is essentially two-dimensional in the perfect crystalline structures considered here. Real devices may obviously show a more marked tri-dimensional transport if some degree of disorder occurs and in this regard the most interdigitated phase III might lead to more efficient 3D transport.

CONCLUSIONS

The deep investigation of polymorphic behavior of NTA revealed five different polymorphs. The crystalline phases are characterized by different color and different emission color from green to red which allow a fast identification also with naked eyes. Phase I, Phase II and Phase III thermally and irreversibly convert to phase IV at different temperature, this remarkable feature could be exploited in the Time-temperature integrator devices.[9] While Phase II and phase III convert at 130°C and 120°C respectively, Phase I converts at 215°C, which permits to design a TTI device which can work in a wide range of temperature.

The structure determination of phase II and Phase III allowed us to better understand the photophysical properties. Indeed, the blue-shifted emission of Phase II was rationalized in terms of the twisted structure of NTA and supported by model calculations. In addition, the structures determined for the two Phases allowed to investigate the charge transport properties of two different polymorphs. Based on the calculations of intra- and inter-molecular parameters we can conclude that NTA shows promising charge transport properties with a dominant n-type character, with Phase II slightly better performing than Phase III. It is well known that different packing affects charge mobilities, but the role of morphology in real materials must clearly be considered, compared to the ideal crystalline phase to which simulations correspond. The role of internal disorder could influence and prevent efficient charge transport even in those cases where the ordered system possess a theoretical favorable arrangement.

Polymorph tuning in thin film wil be pursued for in depth electrical and possibly electrolumescence characterization of different phases in OFETs and OLETs devices.

EXPERIMENTAL SECTION

Polymorphs Crystallization

The molecule NTA was synthesized following the procedure described in the previous paper[4]. The precipitation of NTA in toluene as described in the synthesis yields to the formation of phase I. Phase II is only obtained concomitantly with phase I, by solvent evaporation from toluene. Pure phase III has been obtained from vapour diffusion of pentane in a toluene solution of NTA. Phase IV was obtained only by thermal conversion of Phases I, II and III.

Photophysical Characterization

PL emission was collected with a calibrated optical multichannel analyzer (PMA-11, Hamamatsu).

X-ray Diffraction Analysis

XRPD was performed with a PANalytical X'Pert PRO diffractometer in Bragg.-Brentano configuration equipped with a copper anode (Cu-Kα=1.5418 Å) and a X'Celerator Detector. Soller 0.04 rad, Anti-scatter slit 1/8, divergence slit ¼, step size 0.017°. An Anton Paar TTK 450 system was used for the measurement at a controlled temperature.

SCXRD analysis were carried out by means of a Oxford Diffraction Xcalibur S diffractometer equipped with a molybdenum anode (Mo-Kα=0.71073 Å).

Synchrotron radiation-XRPD measurements of NTA were performed at the Swiss Light Source (SLS) Material Science (MS) Powder Diffraction (PD) end station with a nominal photon energy of 16 keV. Fine Si640D NIST standard refinement returned a wavelength of 0.775375(2) Å and a residual zero error of −0.0253(4) 2θ, step size of 0,0036°. The measurements were performed in transmission geometry, the material was loaded inside a glass capillary with a diameter of 0.5 mm, spun at 4 Hz, with an exposure time of 5 sec.

Thermal Annealing

The analisys was performed using a microscope OLYMPUS BX41 equipped with a VISICAM 5.0 camera and a system for the temperature control Linkam TMS 94. The photos were taken under polarized to underline the modification due to solid state transition, with a 40x magnification.

Computational Details

Equilibrium structures of neutral and charged species were obtained from quantum chemical calculations performed at B3LYP/6-31G* level of theory. The nature of the stationary points obtained by structure optimization was assessed by vibrational frequencies calculations at the optimized structure. Vibrational frequencies were also employed to estimate the vibrational contributions to the intramolecular reorganization energy through the calculations of Huang-Rhys parameters[32,33] (see below). To model electronic absorption spectra time-dependent (TD) DFT calculations were carried out using the B3LYP functional with the 6-31G* basis set. All quantum-chemical calculations are performed using the Gaussian09 suite of programs.[34]

The charge transport properties are investigated within the non-adiabatic hopping mechanism[25], according to which the charge transfer is localized on a pair of neighboring molecules (dimer). The molecular materials considered here are in crystalline form, therefore the dimers are identified by evaluating the distances between the centers of mass of the molecules surrounding a central reference molecule in the crystal. The reliability of the model depends on the relative magnitude of the electronic couplings (or charge transfer integrals) V_{ij} and the reorganization energy λ, with V_{ij} required to be much smaller than λ.[35] The most suitable formulation of the charge transfer kinetic constant k_{eT}, for a dimer, is the Marcus-Levich-Jortner equation[25,26] which represents a quantum correction of the Marcus equation since it includes the quantum nature of the vibrational modes most active in molecular reorganization:

$$k_{eT} = \frac{2\pi}{\hbar} V_{ij}^2 \frac{1}{\sqrt{4\pi\lambda_{class}k_BT}} \sum_{v=0}^{\infty} \left[\exp\left(-S_{eff}\right) \frac{S_{eff}^{v}}{v!} \times \exp\left(-\frac{\left(\Delta G^o + \lambda_{class} + v\hbar\omega_{eff}\right)^2}{4\lambda_{class}k_BT} \right) \right] \qquad (1)$$

The electronic couplings V_{ij} are computed for the HOMO, LUMO and LUMO+1 orbitals (p-type and n-type charge transport) of each dimer, at B3LYP/6-31G* level of theory, in the one-electron approximation and with the direct approach described elsewhere.[36]

The reorganization energy is composed of an intramolecular term λ_i and an “outer” contribution λ_o due to the interaction with the surrounding molecules in the crystal. λ_i is computed at B3LYP/6-31G* level of theory, either with the adiabatic potentials (AP) method or via calculations of Huang-Rhys (HR) parameters S_m.[32,33] In Eq (1) λ_i collects the contribution from quantum vibrational degrees of freedom and is expressed by a single effective vibrational mode of frequency λ_{eff} and associated Huang-Rhys factor S_{eff}. The effective frequency was determined for the model system (NTA-H), discussed in the text, as $\omega_{eff} = \sum_m \omega_m \frac{S_m}{\sum_n S_n}$.

The HR factor S_{eff} is obtained from the relation $\lambda_i = \hbar\omega_{eff}S_{eff}$. The effective parameters evaluated for the model system NTA-H were applied also to the real NTA systems (see Table S1). The computed intramolecular reorganization energies of the real systems are, however, larger than those of the model systems. The exceeding magnitude is mainly due to low frequency modes associated with the flexible alkyl substituents. Because of their low frequency these can be considered classical degrees of freedom and their contribution is included in the λ_{class} term, summed with the outer sphere contribution λ_o assumed to be 0.01 eV according to recent studies.[37] ΔG_0 in eq.(1) is the free energy associated with the self-exchange process considered in this work ($M_0 + M_c \leftrightarrow M_c + M_0$, where M_0 is the molecule in the neutral state and M_c in the charged state). In the presence of an electric field (see below) ΔG_0 is set as -eF·d where F is the electric field vector and d is the vector of the intermolecular distance between the molecules composing the dimer.

Charge mobilities are evaluated under the effect of an electric field according to a time-of-flight (TOF) approach. To this end the 3D crystal structures of the investigated systems are considered and charge mobilities are obtained as

$$\mu = \frac{d_f}{\tau F} \tag{2}$$

where F is the magnitude of the electric field (10^5 V/cm), d_f is the device thickness namely the distance traveled by the charge along the F directions (taken as 0.005 cm) and τ is the time required to travel the distance d_f. The distance travelled is determined by kinetic Monte Carlo simulations (KMC) as described in more detail elsewhere.[27,31] Anisotropies of charge transport are obtained in the *a,b* plane for Phase III and in the *b,c* plane for Phase II.

SUPPORTING INFORMATION

Hot-Stage Microscopy

From HSM analysis we observed the solid state transitionof phase I and phase II to phase IV (Fig S1). The analysis was performed simultaneously on phase I and phase II to underline the differences of the two crystal forms; phase II transformed into phase IV at 150°C (completed at 155°C), after that the transformation of phase I takes place, at 215°C. The melting point occurred in a quite large range, starting at 228°C and finishing around 232°C, probabely due to the unhomogeneity of the sample. During the heating, around 229°C and togheter with the melting, it is visible inside the liquid something similar to a recrystallization process. To explain this behaviour we contemplate the existance of a new crystal phase, stable at high temperature, named phase V. The same behaviour was later observed even in other samples.

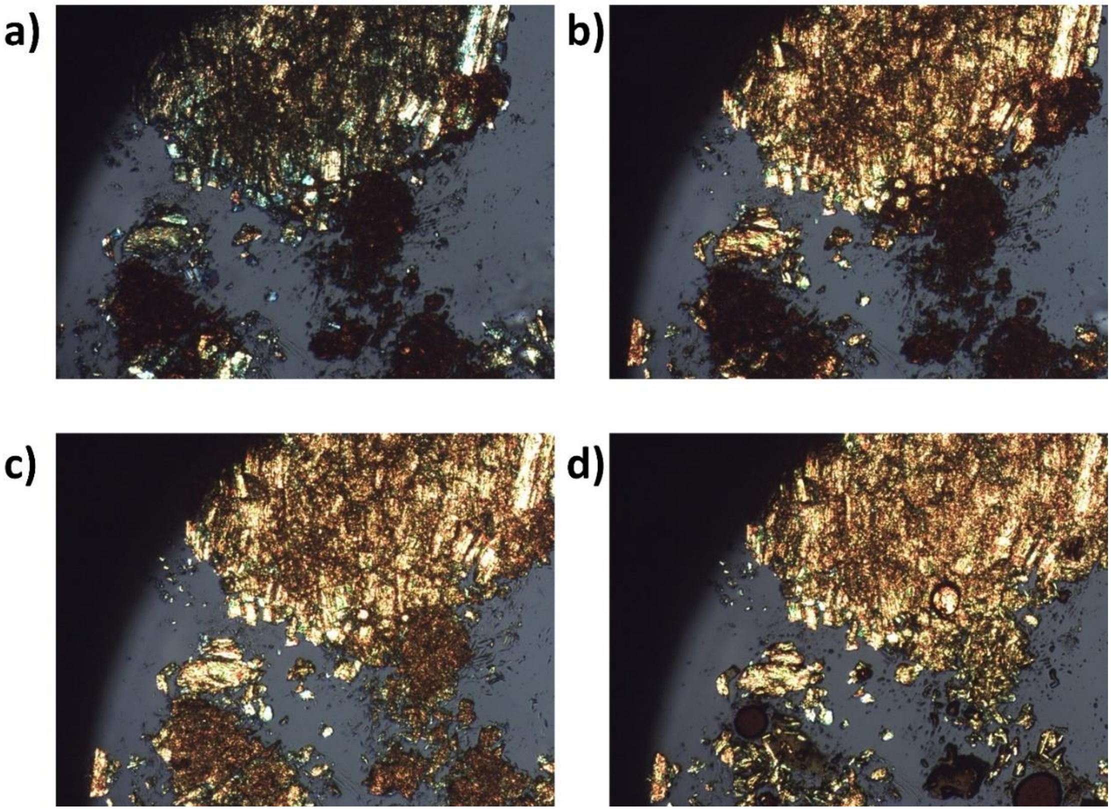

Figure SI1 HSM photos of phase I and phase II taken at different temperature under polarized light (40X magnification); a) 25°C, b) 155°C, c) 215°C, d) 229°C.

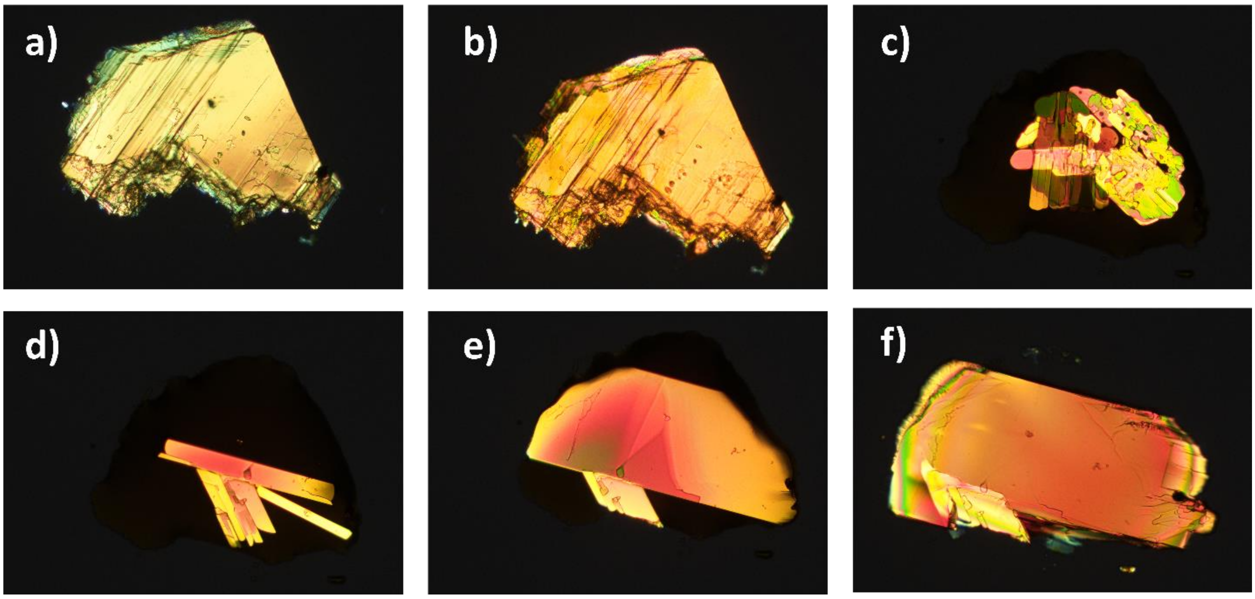

Fig S2 Hot-stage microscopy photos of a phase II crystal taken at different temperature under polarized light (40X magnification); a) 25°C, b) 160°C (transition to phase IV), c) 230°C (melting of phase IV), d) 232.5°C (growth of phase V), e) 231°C, f) 150°C.

Diffraction and structural data

Single crystal X-ray Diffraction

SHELX97[38] was used for structure solution and refinement based on F2. The Non-hydrogen atoms were refined anisotropically. Hydrogen atoms bound to carbon atoms were added in calculated positions. The program Mercury[39] was used for all graphical representations and for the calculated powder pattern.

Table SI1. Crystallographic data three crystal forms of NTA

	PHASE I	**PHASE II**	**PHASE III**
Chemical formula	$C_{34} H_{32} N_2 O_4 S_4$		
Formula Mass	660,90 g/mol		
Crystal System	Monoclinic	Monoclinic	Triclinic
a/Å	25.220(2)	64.262(7)	4.882(3)
b/Å	67.237(5)	5.6259(5)	11.846(6)
c/Å	5.6063(1)	18.487(2)	14.591(9)
α/°	90	90	89.80(5)
β/°	113.58()	92.691(1)	81.89(5)
γ/°	90	90	821.64(4)

Volume/ Å^3	8712.87(2)	6674.9(1)	3392.3(5)
Temperature	190°C	RT	RT
Space group	(C)*	C2/c	P-1
Syn / anti disorder	/	30% / 70%	40% / 60%
R_1	/	0.2253	0.1579
R_{wp}	6.9%	/	/

* The data are not precise enough for an exact determination of the crystal cell. It has been hypothesized that, similarly to phase II, it is a monoclinic-c cell.

Synchrotron X-ray powder diffraction at variable temperature

Synchrotron radiation-XRPD measurements of NTA were performed at the Swiss Light Source (SLS). Multiframing data were recorded in transmission with an exposure time of 5 seconds to avoid radiation damage; the raw data were then individually inspected before being merged together and flat field corrected. At the syncrotron facility were also performed some difraction measurement at variable temperature with the use of a blower for the heating process.

The patterns were indexed with TOPAS5[40] and the best crystal cell obtained was refined with a Pawley refinement (R_{wp}=6.9%) (Fig S2).

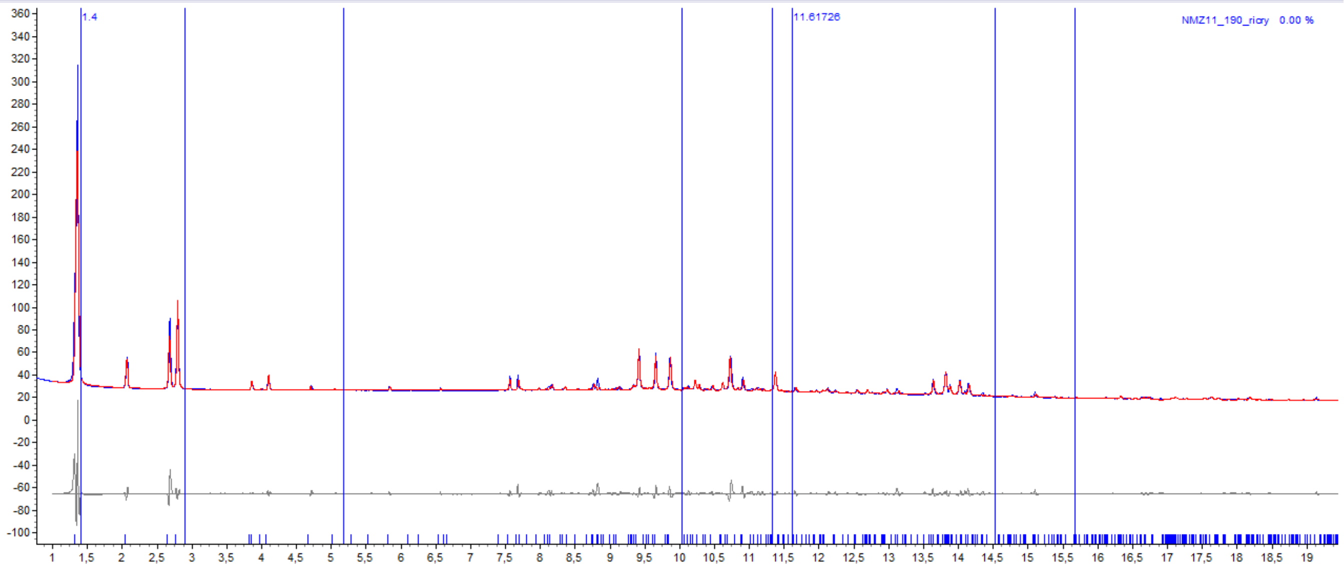

Figure SI3. Pawley refinement of Phase I diffraction pattern

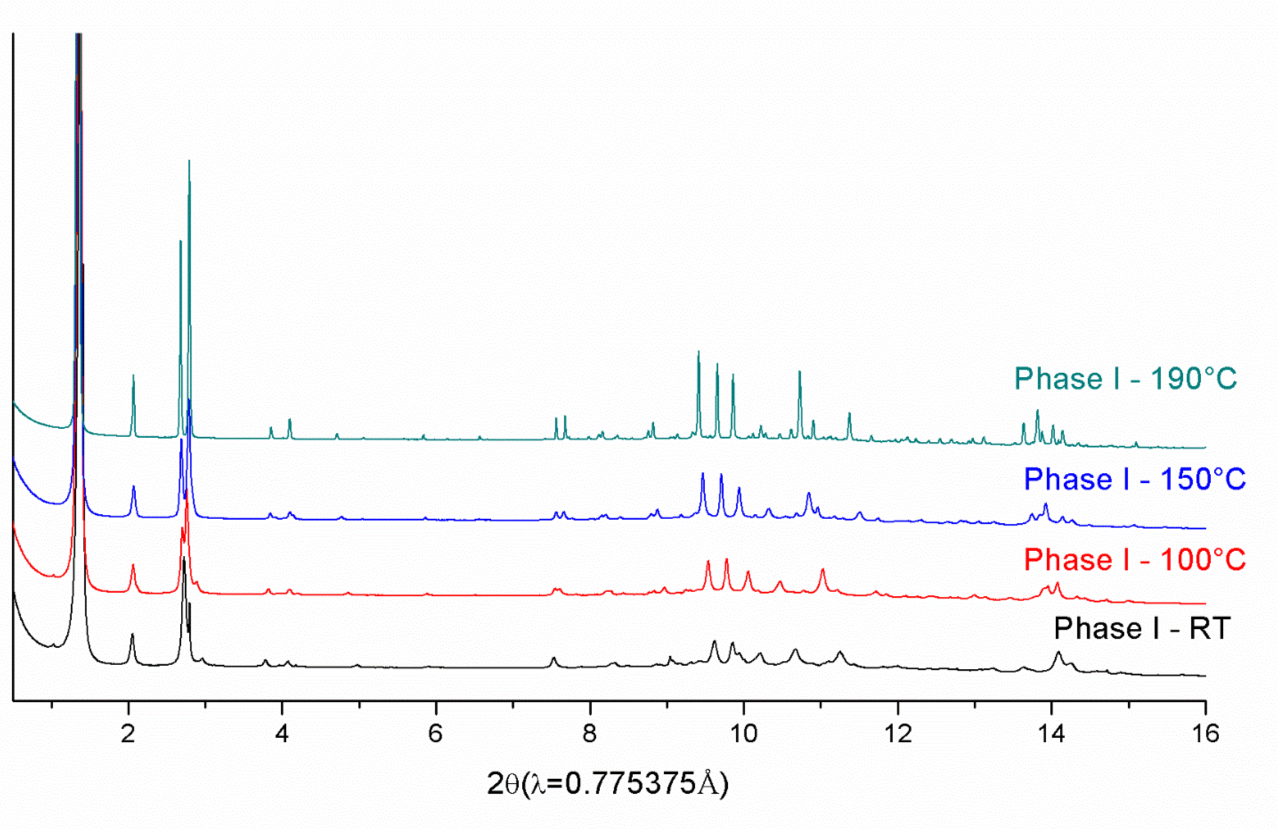

Figure SI4 Diffractograms of Phase I obtained at different temperature

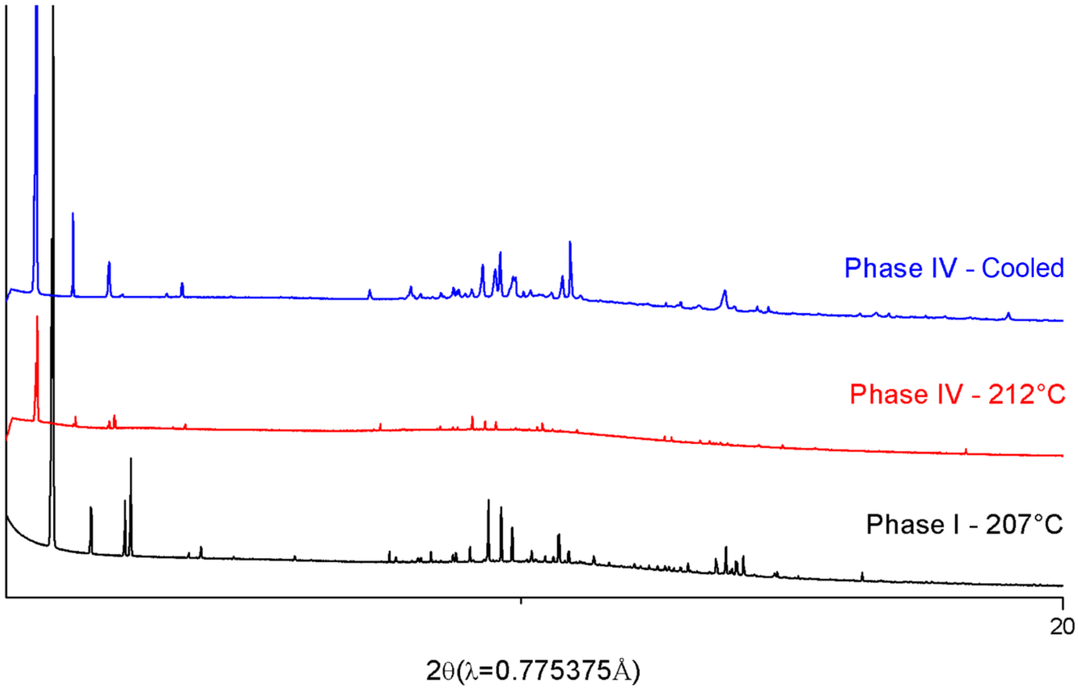

Figure SI5 Solid state transition between phase I and Phase IV

Variable temperature X-ray powder diffraction

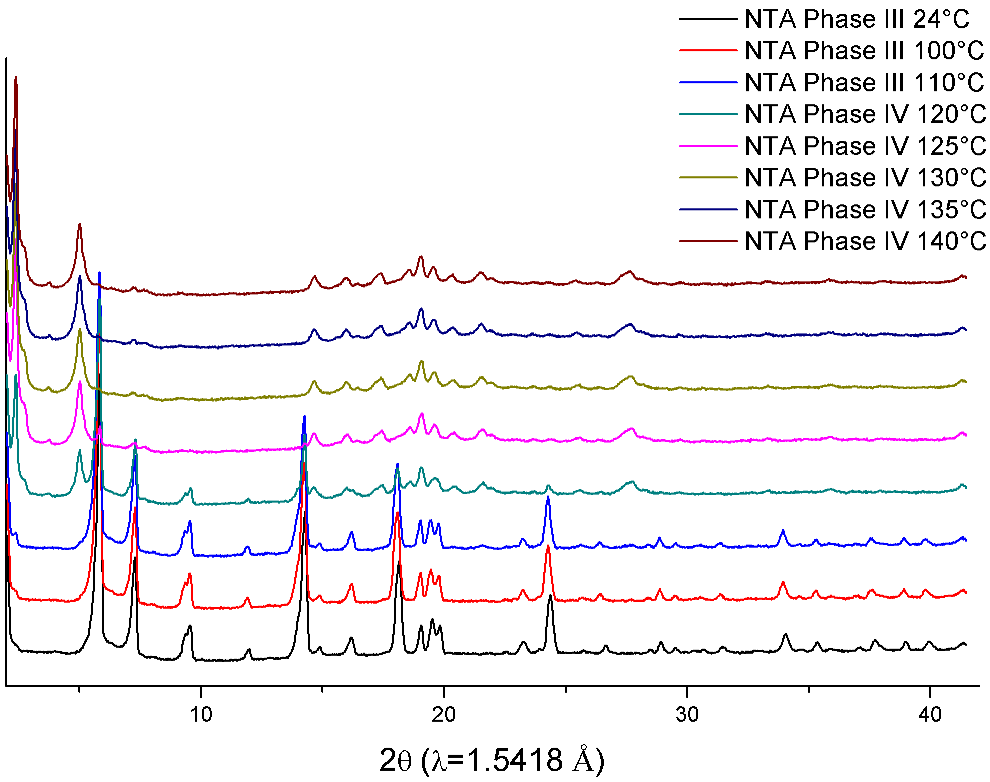

Figure SI6 Variable temperature diffraction of Phase III with the transition to Phase IV at 120°C

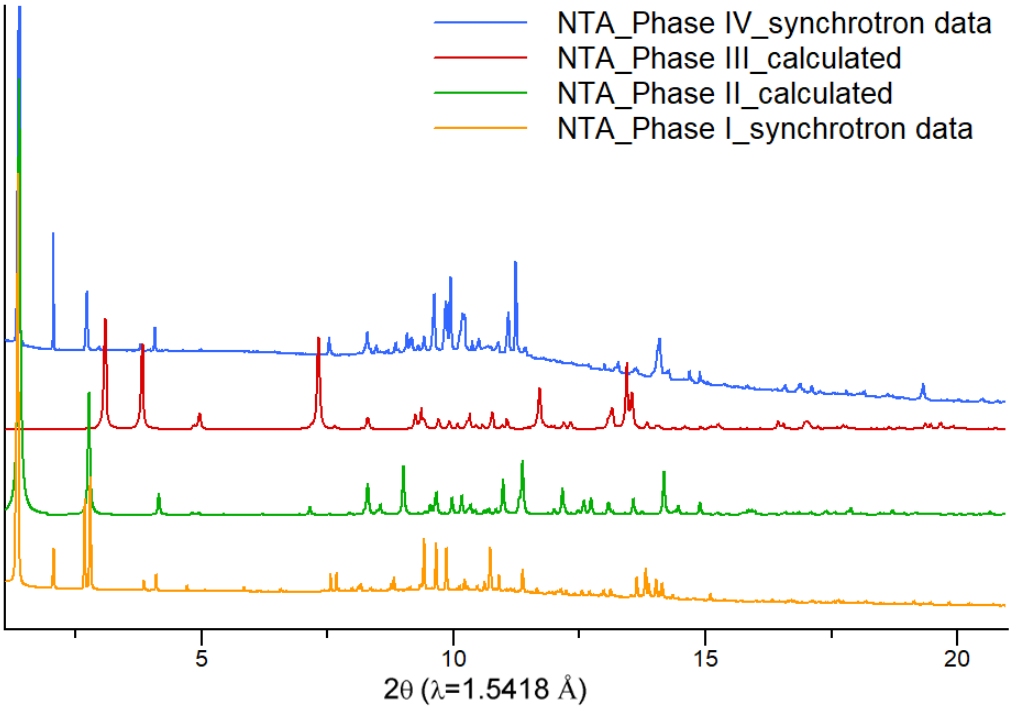

Figure SI7. Comparison of the different different polymorphs diffractograms, Phase I and Phase IV experimental, Phase II and Phase II calculated from the single crystal structure, 2θ (λ=0.775375 Å)

Computational results

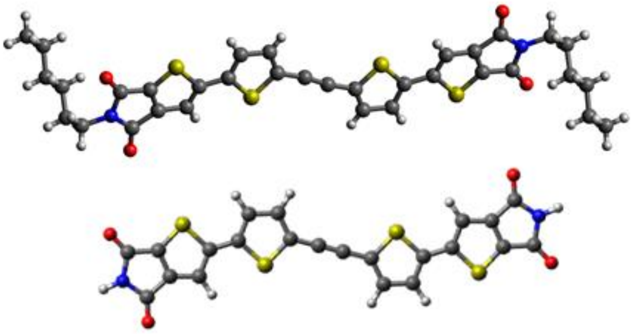

Figure SI8. Molecular structure of AAA-NTA and AAA-NTA-H that were used for the quantum-chemical calculations.

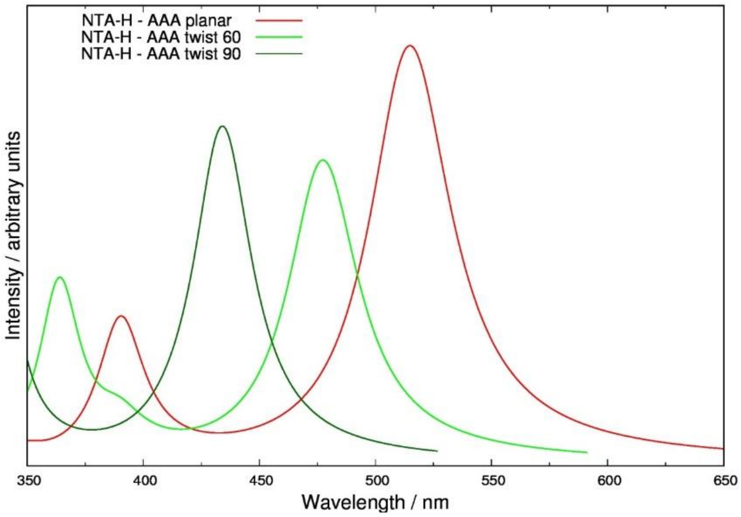

Figure SI9 TD-B3LYP/6-31G* computed absorption spectra for AAA-NTA-H conformer with different values of the dihedral angle (0, 60 and 90 degrees in red, light green and green, respectively).

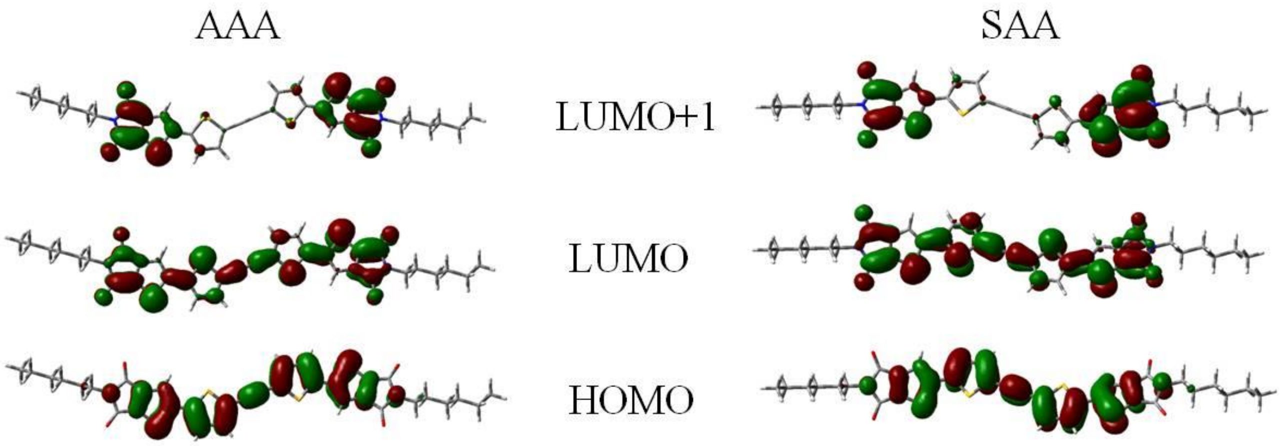

Figure SI10 Shapes of the orbitals computed at the B3LYP/6-31G* optimized geometries of *AAA*-NTA and *SAA*-NTA. We also included the LUMO+1 orbital since we have previously shown [3] that orbitals energetically close to the frontier orbitals may contribute significantly to the charge transport.

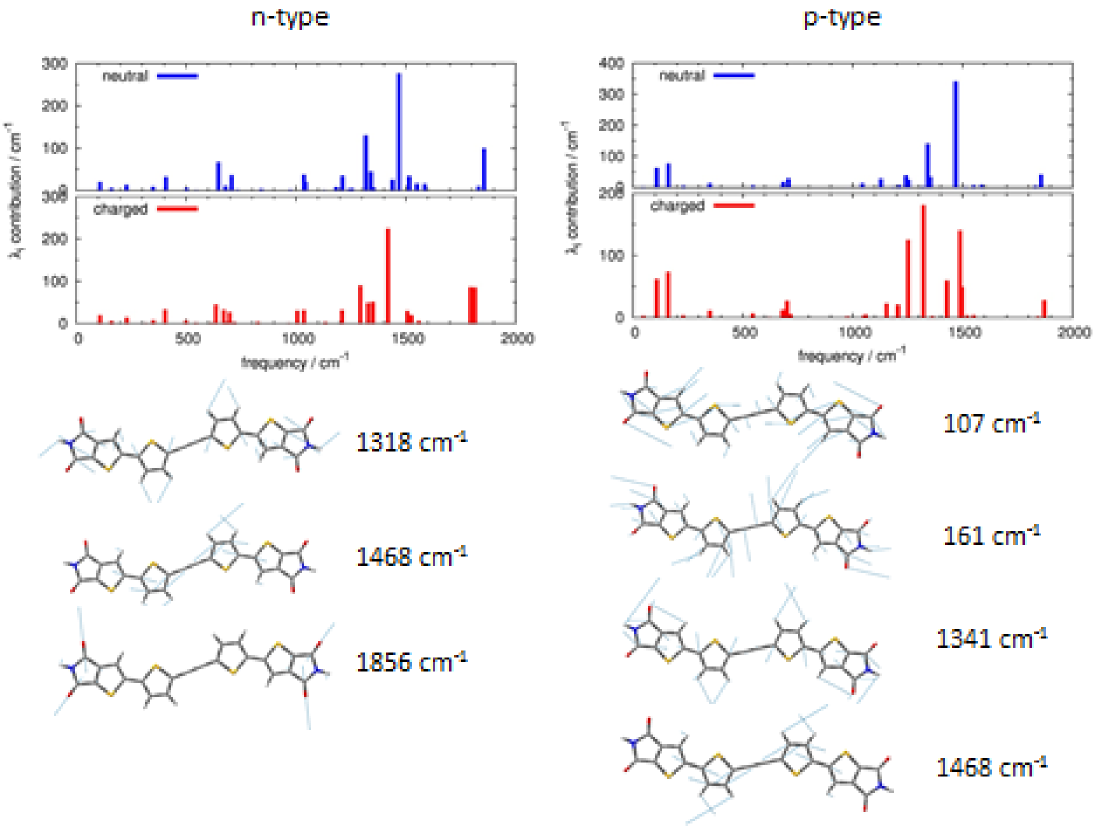

Figure SI11 The vibrational frequencies contributions to the computed intramolecular reorganization energies of NTA-H. Each graph shows the contribution from neutral species on the top and from the charged species in the bottom part. From B3LYP/6-31G* calculations. The shape of the most active normal modes in assisting charge transport is shown in the bottom part. It can be seen that low frequency modes contribute to p-type charge transport thereby lowering the frequency of the effective mode in Table S5 for p-type charge transport.

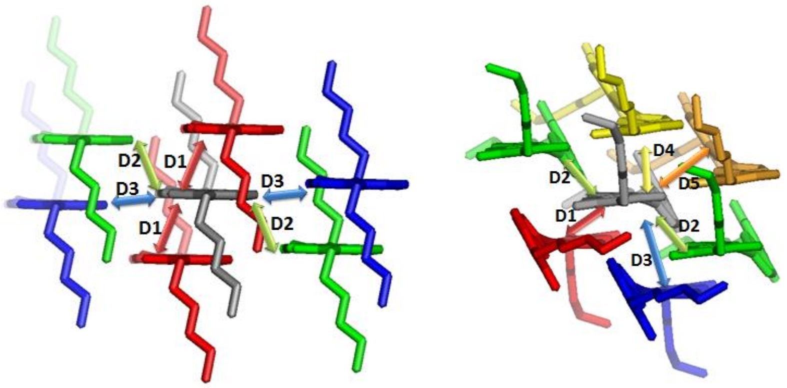

Figure SI12 (left) Phase III. Portion of the SAA-NTA crystal showing the central grey molecule and its nearest neighbors displaying the largest computed electronic couplings. (right) Phase II. Portion of the mixed-AAA-SAA-NTA crystal showing the central grey molecule and its nearest neighbors displaying the largest computed electronic couplings. For the mixed crystal of phase III we assumed that conformers of the same type (AAA or SAA) are found along the D3 pathway while conformers of different type are found along the other pathways. For the mixed crystal of phase II we assumed that conformers of the same type (AAA or SAA) are found along the D2 pathway while conformers of different type are found along the other pathways.

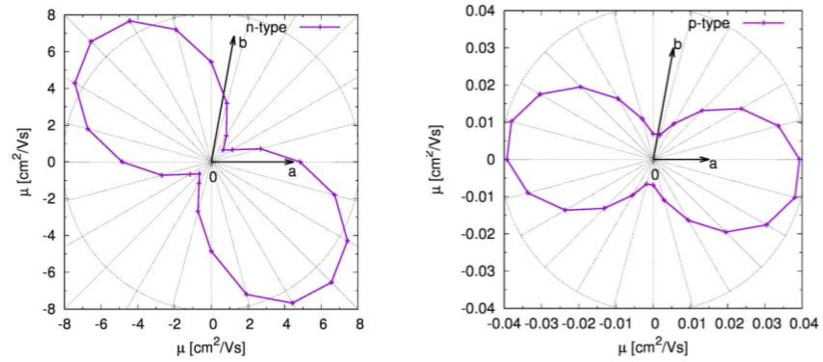

(a) phase III – pure AAA crystal

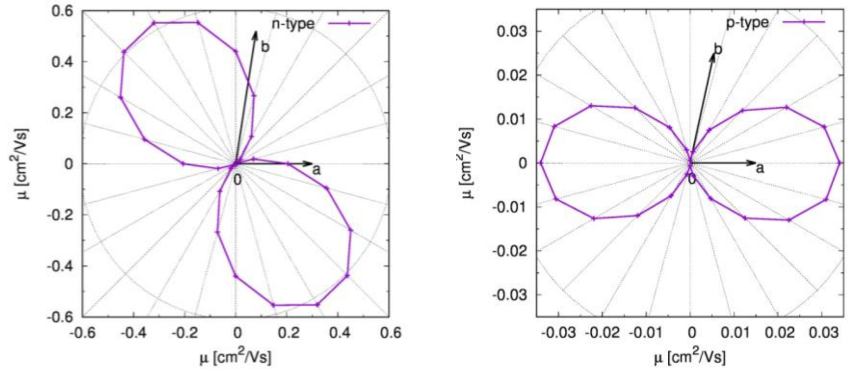

(b) phase III – pure SAA crystal

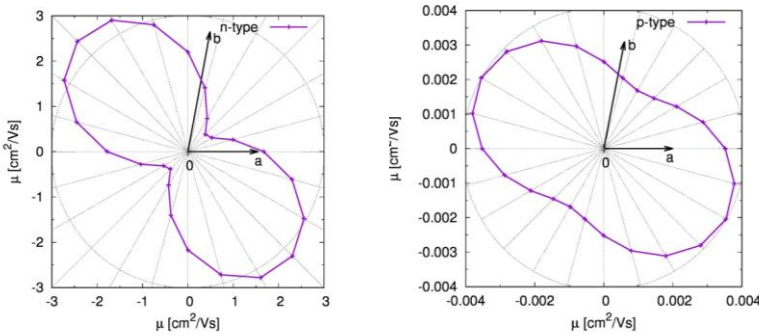

(c) phase III – mixed-SAA-AAA crystal

Figure SI13. Computed charge-transport anisotropy for the crystal of NTA in phase III. Anisotropy in the *a,b* crystallographic plane from KMC TOF simulations involving the anion (LUMO) as charge carrier (left) and the cation (HOMO) as charge carrier (right).

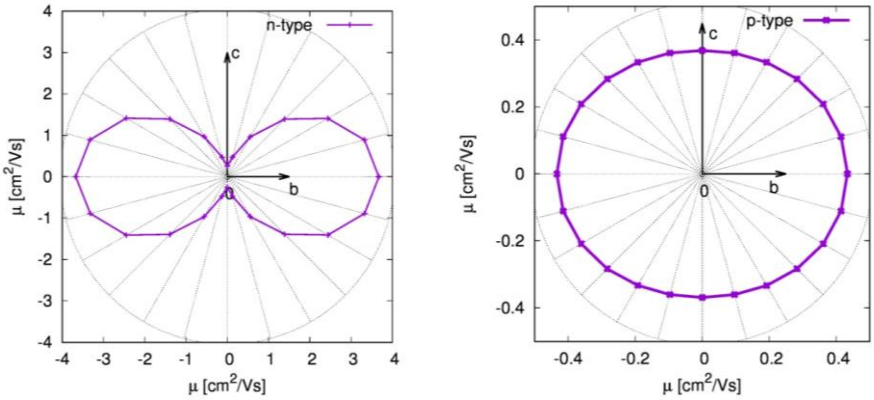

(a) phase II – AAA

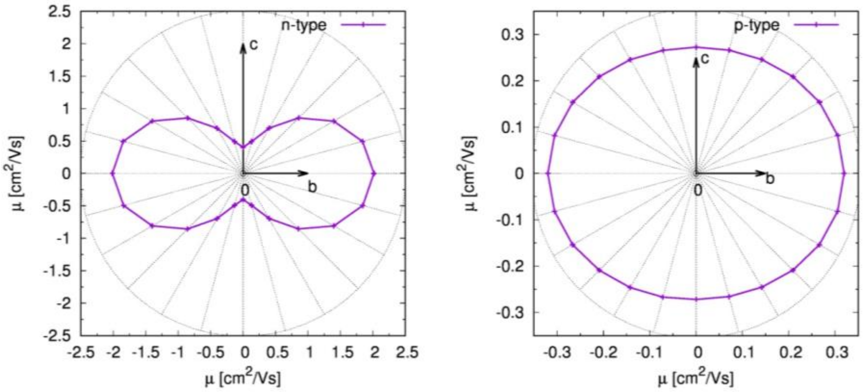

(b) phase II – mixed-SAA-AAA

Figure SI14. Computed charge-transport anisotropy for the crystal of NTA in phase II. Anisotropy in the *b,c* crystallographic plane from KMC TOF simulations involving the anion (LUMO) as charge carrier (left) and the cation (HOMO) as charge carrier (right).

Table SI2. Vertical excitations energies and oscillator strengths for planar and twisted NTA-H computed at TD-B3LYP/6-31G* level of theory.

Compound	State	Energy/eV(nm)	wf	*f*
planar				
AAA-NTA-H	S_1	2.41(515)	H→L	1.42
SAA-NTA-H	S_1	2.40(517)	H→L	1.45
SAS-NTA-H	S_1	2.39(519)	H→L	1.48
twisted 60°				
AAA-NTA-H	S_1	2.60(477)	H→L	1.03
SAA-NTA-H	S_1	2.59(479)	H→L	1.03
SAS-NTA-H	S_1	2.57(482)	H→L	1.03
twisted 90°				
AAA-NTA-H	S_2	2.86(434)	H→L	1.13
SAA-NTA-H	S_3	2.85(434)	H→L	1.14
SAS-NTA-H	S_3	2.85(435)	H→L	1.15

Table SI3. Frontier orbital energies and transport gaps for *SAA*- and *AAA*-NTA computed at the B3LYP/6-31G* optimized structures of the neutral systems.

Compound	E(HOMO) eV	E(LUMO) eV	E(LUMO+1) eV	ΔE(L/L+1) eV	ΔE(H-L) eV
AAA-NTA	-5.59	-2.92	-2.59	0.33	2.67
SAA-NTA	-5.61	-2.90	-2.58	0.32	2.71

Table SI4. Intramolecular reorganization energy computed with the adiabatic potential (AP) method, at B3LYP/6-31G* level of theory, for n-type and p-type charge transport: $\lambda_i^{n\,(AP)}$ and $\lambda_i^{c\,(AP)}$ are the contributions from the neutral and the charged states, respectively, to the total AP reorganization energy λ_i^{AP}

Compound	λ_i^{AP} / eV	$\lambda_i^{n\,(AP)}$ / eV	$\lambda_i^{c\,(AP)}$ / eV
n-type			
AAA-NTA	0.281	0.138	0.143
SAA-NTA	0.315	0.146	0.169
AAA-NTA-H	0.250	0.128	0.123
SAA-NTA-H	0.251	0.128	0.123
p-type			
AAA-NTA	0.264	0.128	0.135
SAA-NTA	0.296	0.135	0.161
AAA-NTA-H	0.250	0.126	0.124
SAA-NTA-H	0.249	0.125	0.124

Table SI5. Effective frequency ω_{eff} and associated Huang-Rhys factor S_{eff} employed to calculate rate constants

Compound		ω_{eff} / cm^{-1}	S_{eff}	λ_i^{ref} / eV	λ_{class} /eV ^{a}	λ_{class}^{tot} /eV^{b}
AAA-NTA	n-type	877	2.299	0.250	0.031	0.041
AAA-NTA	p-type	566	3.564	0.250	0.014	0.024
SAA-NTA	n-type	878	2.298	0.250	0.064	0.074
SAA-NTA	p-type	549	3.662	0.249	0.046	0.056
Mixed AAA-SAA-NTA [c]	n-type	877	2.298	0.250	0.030	0.040
	p-type	558	3.613	0.250	0.047	0.057

[a] Contributions to classical reorganization energy from intramolecular classical vibrations. [b] Total classical reorganization energy, adding 0.01 eV to λ_{class}, the contribution of external reorganization energy according to recent estimates of the outer contribution [4] [c] Reorganization energy of the mixed crystal computed as an average of AAA and SAA data.

Table SI6. Computed electronic couplings (B3LYP/6-31G* level of theory) and charge rate constants for n-type and p-type charge transport of phase III. Values computed for crystals of AAA-NTA, SAA-NTA and mixed-AA-SAA-NMZ are reported

Compound	Dimer label	Dist. / Å	V_{ij}^{HOMO} / meV ^{a}	V_{ij}^{LUMO} / meV ^{a}	V_{ij}^{LUMO+1} / meV ^{a}	$k_{eT}^{p\text{-}type}$ / ps^{-1} ^{b}	$k_{eT}^{n\text{-}type}$ / ps^{-1} ^{b}
AAA-NTA	D1	4.8820	10	50	30	0.30	14.1
	D2	13.9357	2	36	30	0.10	7.16
	D3	17.1064	0	23	28	0.00	2.93
SAA-NTA	D1	4.8820	13	1	-14	0.26	0.00
	D2	13.9357	1	15	13	0.00	0.74
	D3	17.1064	0	3	1	0.00	0.04
Mixed -NTA	D1a	4.8420	17	72	54	0.57	22.0
	D1b	4.9240	2	28	12	0.01	3.33
	D2a	13.8719	2	35	30	0.01	5.07
	D2b	13.9985	1	16	12	0.00	1.08
	D3AA	17.0428	0	22	29	0.00	0.05
	D3SS	17.1694	0	3	1	0.00	2.17

[a] Electronic couplings computed according to the 2x2 orthogonalization procedure.[5] [b]Kinetic constants computed in the absence of an external electric field

Table SI7. Computed electronic couplings (B3LYP/6-31G* level of theory) and charge rate constants for n-type and p-type charge transport of phase II. Values computed for crystals of AAA-NTA and mixed-AA-SAA-NMZ are reported

Compound	Dimer label	Dist. / Å	V_{ij}^{HOMO} / meV ^{a}	V_{ij}^{LUMO} / meV ^{a}	V_{ij}^{LUMO+1} / meV ^{a}	$k_{eT}^{p\text{-}type}$ / ps^{-1} ^{b}	$k_{eT}^{n\text{-}type}$ / ps^{-1} ^{b}
AAA-NTA	D1	4.7046	20	56	65	1.06	18.1
	D2	5.6109	17	1	7	0.80	0.50
	D3	5.6259	9	71	42	0.25	28.4
	D4	6.0990	57	12	19	8.74	0.82
Mixed -NTA	D1	4.7166	21	28	31	0.86	3.26
	D2SS	5.6259	2	48	33	0.01	9.75
	D2AA	5.6259	9	71	42	0.18	21.1
	D3	5.7078	15	2	1	0.43	0.02
	D4	6.0362	55	3	21	6.08	0.05
	D5	6.1172	59	42	7	6.88	7.46

[a] Electronic couplings computed according to the 2x2 orthogonalization procedure.[5] [b] Kinetic constants computed in the absence of an external electric field

Table SI8. TOF charge mobilities for AAA-NTA, SAA-NTA and mixed AAA-SAA-NTA, computed from KMC simulations for an electric field directed along the crystallographic axes. The largest mobility μ_{max} computed for each set is also reported.

			Phase III		
		μ_a / cm^2/(Vs)	μ_b / cm^2/(Vs)	μ_a/μ_b ^{a}	μ_{max} ^{b}/ cm^2/(Vs)
AAA-NTA	n-type	4.85	5.44	0.89	**9.26**
AAA-NTA	p-type	0.04	0.01	4.00	0.04
SAA-NTA	n-type	0.21	0.44	0.48	**0.64**
SAA-NTA	p-type	0.03	0.00	56.1	0.03
mixed-NTA	n-type	1.67	2.20	0.76	**3.45**
mixed-NTA	p-type	0.00	0.00	-	0.00
			Phase II		
		μ_b / cm^2/(Vs)	μ_c / cm^2/(Vs)	μ_b/μ_c ^{c}	μ_{max} ^{d}/ cm^2/(Vs)
AAA-NTA	n-type	3.67	0.26	1.18	**3.67**
AAA-NTA	p-type	0.43	0.37	26	0.43
mixed-NTA	n-type	2.02	0.10	20.2	**2.02**
mixed-NTA	p-type	0.32	0.27	1.19	0.32

[a] Anisotropy ratio between the mobility along *a* and the mobility along *b.* [b] Maximum computed value of the mobility in the *ab* plane. [c] Anisotropy ratio between the mobility along *b* and the mobility along *c.* [d] Maximum computed value of the mobility in the *bc* plane.

REFERENCES

(1) Treat, N. D.; Westacott, P.; Stingelin, N. The Power of Materials Science Tools for Gaining Insights into Organic Semiconductors. *Annu. Rev. Mater. Res.* **2015**, *45* (1), 459–490.

(2) Melucci, M.; Zambianchi, M.; Favaretto, L.; Gazzano, M.; Zanelli, A.; Monari, M.; Capelli, R.; Troisi, S.; Toffanin, S.; Muccini, M. Thienopyrrolyl Dione End-Capped Oligothiophene Ambipolar Semiconductors for Thin Film- and Light Emitting Transistors. *Chem. Commun.* **2011**, *47* (43), 11840–11842.

(3) Melucci, M.; Durso, M.; Bettini, C.; Gazzano, M.; Maini, L.; Toffanin, S.; Cavallini, S.; Cavallini, M.; Gentili, D.; Biondo, V.; et al. Structure–property Relationships in Multifunctional Thieno(Bis)Imide-Based Semiconductors with Different Sized and Shaped N-Alkyl Ends. *J. Mater. Chem. C* **2014**, *2* (17), 3448.

(4) Zambianchi, M.; Favaretto, L.; Durso, M.; Bettini, C.; Zanelli, A.; Manet, I.; Gazzano, M.; Maini, L.; Gentili, D.; Toffanin, S.; et al. Synergic Effect of Unsaturated Inner Bridges and Polymorphism for Tuning the Optoelectronic Properties of 2,3-Thieno(Bis)Imide Based Materials. *J. Mater. Chem. C* **2015**, *3* (1), 121–131.

(5) Benvenuti, E.; Gentili, D.; Chiarella, F.; Portone, A.; Barra, M.; Cecchini, M.; Cappuccino, C.; Zambianchi, M.; Lopez, S. G.; Salzillo, T.; et al. Tuning Polymorphism in 2,3-Thienoimide Capped Oligothiophene Based Field-Effect Transistors by Implementing Vacuum and Solution Deposition Methods. *J. Mater. Chem. C,* **2018**, *6* (21), 5601–5608.

(6) Di Maria, F.; Fabiano, E.; Gentili, D.; Biasiucci, M.; Salzillo, T.; Bergamini, G.; Gazzano, M.; Zanelli, A.; Brillante, A.; Cavallini, M.; et al. Polymorphism in Crystalline Microfibers of Achiral Octithiophene: The Effect on Charge Transport, Supramolecular Chirality and Optical Properties. *Adv. Funct. Mater.* **2014**, *24* (31), 4943–4951.

(7) Hiszpanski, A. M.; Baur, R. M.; Kim, B.; Tremblay, N. J.; Nuckolls, C.; Woll, A. R.; Loo, Y. L. Tuning Polymorphism and Orientation in Organic Semiconductor Thin Films via Post-Deposition Processing. *J. Am. Chem. Soc.* **2014**, *136* (44), 15749–15756.

(8) Chung, H.; Diao, Y. Polymorphism as an Emerging Design Strategy for High Performance Organic Electronics. *Journal of Materials Chemistry C*. Royal Society of Chemistry May 5, **2016**, pp 3915–3933.

(9) Gentili, D.; Durso, M.; Bettini, C.; Manet, I.; Gazzano, M.; Capelli, R.; Muccini, M.; Melucci, M.; Cavallini, M. A Time-Temperature Integrator Based on Fluorescent and Polymorphic Compounds. *Sci. Rep.* **2013**, *3*, 2581.

(10) Yan, D.; Evans, D. G. Molecular Crystalline Materials with Tunable Luminescent Properties: From Polymorphs to Multi-Component Solids. *Materials Horizons*. The Royal Society of Chemistry **2014**, pp 46–57.

(11) Pfattner, R.; Bromley, S. T.; Rovira, C.; Mas-Torrent, M. Tuning Crystal Ordering, Electronic Structure, and Morphology in Organic Semiconductors: Tetrathiafulvalenes as a Model Case. *Adv. Funct. Mater.* **2016**, *26* (14), 2256–2275.

(12) He, P.; Tu, Z.; Zhao, G.; Zhen, Y.; Geng, H.; Yi, Y.; Wang, Z.; Zhang, H.; Xu, C.; Liu, J.; et al. Tuning the Crystal Polymorphs of Alkyl Thienoacene via Solution Self-Assembly toward Air-Stable and High-Performance Organic Field-Effect Transistors. *Adv. Mater.* **2015**, *27* (5), 825–830.

(13) Durso, M.; Bettini, C.; Zanelli, A.; Gazzano, M.; Lobello, M. G.; De Angelis, F.; Biondo, V.; Gentili, D.; Capelli, R.; Cavallini, M.; et al. Synthesis, Size-Dependent Optoelectronic and Charge Transport Properties of Thieno(Bis)Imide End-Substituted Molecular Semiconductors. *Org. Electron. physics, Mater. Appl.* **2013**, *14* (11), 3089–3097.

(14) He, X.; Benniston, A. C.; Saarenpää, H.; Lemmetyinen, H.; Tkachenko, N. V; Baisch, U. Polymorph Crystal Packing Effects on Charge Transfer Emission in the Solid State. *Chem. Sci.* **2015**, *6* (6), 3525–3532.

(15) David, W. I. F.; Shankland, K. *Structure Determination from Powder Diffraction Data*; Oxford University Press: New York, **2008**; Vol. 64.

(16) Stokes, M. A.; Kortan, R.; Amy, S. R.; Katz, H. E.; Chabal, Y. J.; Kloc, C.; Siegrist, T. Molecular Ordering in Bis(Phenylenyl)Bithiophenes. *J. Mater. Chem.* **2007**, *17* (32), 3427–3432.

(17) Neumann, M. A.; Tedesco, C.; Destri, S.; Ferro, D. R.; Porzio, W. Bridging the Gap - Structure Determination of the Red Polymorph of Tetrahexylsexithiophene by Monte Carlo Simulated Annealing, First-Principles DFT Calculations and Rietveld Refinement. *J. Appl. Crystallogr.* **2002**, *35* (3), 296–303.

(18) Tedesco, E.; Della Sala, F.; Favaretto, L.; Barbarella, G.; Albesa-Jové, D.; Pisignano, D.; Gigli, G.; Cingolani, R.; Harris, K. D. M. Solid-State Supramolecular Organization, Established Directly from Powder Diffraction Data, and Photoluminescence Efficiency of Rigid-Core Oligothiophene-S,S-Dioxides. *J. Am. Chem. Soc.* **2003**, *125* (40), 12277–12283.

(19) Porzio, W.; Destri, S.; Pasini, M.; Rapallo, A.; Giovanella, U.; Vercelli, B.; Campione, M. Close Packing in Crystals of Cyanophenylene/Thienylene Derivatives. *Cryst. Growth Des.* **2006**, *6* (6), 1497–1503.

(20) Maini, L.; Gallino, F.; Zambianchi, M.; Durso, M.; Gazzano, M.; Rubini, K.; Gentili, D.; Manet, I.; Muccini, M.; Toffanin, S.; et al. Chemical Design Enables the Control of Conformational Polymorphism in Functional 2,3-Thieno(Bis)Imide-Ended Materials. *Chem. Commun.* **2015**, *51* (11), 2033–2035.

(21) Maini, L.; Gallino, F.; Zambianchi, M.; Durso, M.; Gazzano, M.; Rubini, K.; Gentili, D.; Manet, I.; Muccini, M.; Toffanin, S.; et al. Chemical Design Enables the Control of Conformational Polymorphism in Functional 2,3-Thieno(Bis)Imide-Ended Materials. *Chem. Commun.* **2014**, *51* (11), 2033–2035.

(22) Cappuccino, C.; Mazzeo, P. P.; Salzillo, T.; Venuti, E.; Giunchi, A.; Della Valle, R. G.; Brillante, A.; Bettini, C.; Melucci, M.; Maini, L. A Synergic Approach of X-Ray Powder Diffraction and Raman Spectroscopy

for Crystal Structure Determination of 2,3-Thienoimide Capped Oligothiophenes. *Phys. Chem. Chem. Phys.* **2018**, *20* (5), 3630–3636.

(23) Ostoja, P.; Maccagnani, P.; Gazzano, M.; Cavallini, M.; Kengne, J. C.; Kshirsagar, R.; Biscarini, F.; Melucci, M.; Zambianchi, M.; Barbarella, G. FET Device Performance, Morphology and X-Ray Thin Film Structure of Unsubstituted and Modified Quinquethiophenes. *Synth. Met.* **2004**, *146* (3), 243–250.

(24) Guidotti, G.; Gigli, M.; Soccio, M.; Lotti, N.; Gazzano, M.; Siracusa, V.; Munari, A. Poly(Butylene 2,5-Thiophenedicarboxylate): An Added Value to the Class of High Gas Barrier Biopolyesters. *Polymers (Basel).* **2018**, *10* (2), 167.

(25) Barbara, P. F.; Meyer, T. J.; Ratner, M. A. Contemporary Issues in Electron Transfer Research. *J. Phys. Chem.* **1996**, *100* (31), 13148–13168.

(26) Jortner, J. Temperature Dependent Activation Energy for Electron Transfer between Biological Molecules. *J. Chem. Phys.* **1976**, *64* (12), 4860–4867.

(27) Canola, S.; Negri, F. Anisotropy of the N-Type Charge Transport and Thermal Effects in Crystals of a Fluoro-Alkylated Naphthalene Diimide: A Computational Investigation. *Phys. Chem. Chem. Phys.* **2014**, *16* (39), 21550–21558.

(28) Di Motta, S.; Siracusa, M.; Negri, F. Structural and Thermal Effects on the Charge Transport of Core-Twisted Chlorinated Perylene Bisimide Semiconductors. *J. Phys. Chem. C* **2011**, *115* (42), 20754–20764.

(29) Di Donato, E.; Fornari, R. P.; Di Motta, S.; Li, Y.; Wang, Z.; Negri, F. N-Type Charge Transport and Mobility of Fluorinated Perylene Bisimide Semiconductors. *J. Phys. Chem. B* **2010**, *114* (16), 5327–5334.

(30) Di Motta, S.; Di Donato, E.; Negri, F.; Orlandi, G.; Fazzi, D.; Castiglioni, C. Resistive Molecular Memories: Influence of Molecular Parameters on the Electrical Bistability. *J. Am. Chem. Soc.* **2009**, *131* (18), 6591–6598.

(31) Canola, S.; Negri, F. Role of the HOMO-1 Orbital on the p-Type Charge Transport of the Fused-Ring Thienoacene DBTDT. *J. Phys. Chem. C* **2015**, *119* (21), 11499–11505.

(32) Brédas, J. L.; Beljonne, D.; Coropceanu, V.; Cornil, J. Charge-Transfer and Energy-Transfer Processes in π-Conjugated Oligomers and Polymers: A Molecular Picture. *Chem. Rev.* **2004**, *104* (11), 4971–5003.

(33) Coropceanu, V.; Cornil, J.; da Silva Filho, D. A.; Olivier, Y.; Silbey, R.; Brédas, J. L. Charge Transport in Organic Semiconductors. *Chemical Reviews*. **2007**, pp 926–952.

(34) Frisch, J. M.; Trucks, W. G.; Schlegel, B. H.; Scuseria, E. G.; Robb, A. M.; Cheeseman, R. J.; Scalmani, G.; Barone, V.; Mennucci, B.; Petersson, A. G. Gaussian 09, Revision D.01. Gaussian, Inc., Wallingfortd, CT **2009**.

(35) Troisi, A. Charge Transport in High Mobility Molecular Semiconductors: Classical Models and New Theories. *Chemical Society Reviews*. The Royal Society of Chemistry, **2011**, pp 2347–2358.

(36) Canola, S.; Pecoraro, C.; Negri, F. Dimer and Cluster Approach for the Evaluation of Electronic Couplings Governing Charge Transport: Application to Two Pentacene Polymorphs. *Chem. Phys.* **2016**, *478*, 130–138.

(37) McMahon, D. P.; Troisi, A. Evaluation of the External Reorganization Energy of Polyacenes. *J. Phys. Chem. Lett.* **2010**, *1* (6), 941–946.

(38) Herbst-Irmer, R.; Sheldrick, G. M. Refinement of Twinned Structures with SHELXL97. *Acta Crystallogr. B* **1998**, *54* (4), 443–449.

(39) Macrae, C. F.; Bruno, I. J.; Chisholm, J. A.; Edgington, P. R.; McCabe, P.; Pidcock, E.; Rodriguez-Monge, L.; Taylor, R.; van de Streek, J.; Wood, P. A. Mercury CSD 2.0 – New Features for the Visualization and Investigation of Crystal Structures. *J. Appl. Crystallogr.* **2008**, *41* (2), 466–470.

(40) Coelho, A. A. *TOPAS* and *TOPAS-Academic* : An Optimization Program Integrating Computer Algebra and Crystallographic Objects Written in C++. *J. Appl. Crystallogr.* **2018**, *51* (1), 210–218.

CHAPTER 7: MECHANOCHEMISTRY, AN EASY TECHNIQUE TO BOOST THE SYNTHESIS OF CuI PYRAZINE POLYMERS

This project was a part of the PhD project of Dr. Francesco Farinella at the Molecular Crystal Engineering group (PhD thesis: “Synthesis and characterization of new luminescent complexes based on Copper(I) iodide”, 2017, University of Bologna), he performed the screening using CuI and pyrazine as reagents, discovering the new coordination polymer $[(CuI)_2(pyz)_2]_n$ and studing the conversion between the other known CuI-pyz coordination polymers.

During my PhD the work was expanded discovering new conversion routes and solving the crystal structure of $[(CuI)_2(pyz)_2]_n$ *via* X-ray powder diffraction. Additionally, there were performed reaction with 4-cyanopyrazine to yield a mixed ligand structure, $[(CuI)(4CN\text{-}py)_2pyz]_n$.

ABSTRACT

The solid state reaction of CuI with pyrazine (pyz) yielded three distinct coordination polymers depending on the experimental conditions: a double chain polymer $[Cu_2I_2(pyz)]_n$ (yellow powder), a single strand $[CuI(pyz)]_n$ (red powder) and its new isomeric compound $[(CuI)_2(pyz)_2]_n$ (orange powder), which present dimers of CuI bridged by the pyrazine ligands. Crystals of red $[CuI(pyz)]_n$ were obtained by solvothermal reaction, while microcrystalline powder can be easily obtained by kneading (grinding with a drop of acetonitrile) of copper iodide with pyrazine. When the same solid state reaction is carried without the addition of solvents the orange $[(CuI)_2(pyz)_2]_n$, whose structure was determined by X-ray powder diffraction, is obtained. The orange isomer is not stable and in presence of solvent or vapor readily transforms into the red isomer. By heating up to 110°C, $[CuI(pyz)]_n$ or $[(CuI)_2(pyz)_2]_n$ convert into $[Cu_2I_2(pyz)]_n$, which reverts to the starting compounds upon kneading or grinding in the presence of pyrazine. $[Cu_2I_2(pyz)]_n$ reacts also with 4-cyanopyrazine to yield the mixed ligand compound $[(CuI)(4CN\text{-}py)_2py]_n$ which, upon heating, decomposes into $[Cu_2I_2(pyz)]_n$ and $[(CuI)_4(4CN\text{-}py)_5]_n$.

INTRODUCTION

Coordination polymers based on the combination of metal ions and ligands are interesting because of their potential applications as multifunctional and multi-stimuli responsive materials. In the case of luminescent materials, the final properties can be tuned by an appropriate choice of ligand bridges and metal coordination nodes.[1–4] In this respect the quest for more sustainable materials is driving towards the use of coinage metals, which are cheaper and more environmentally friendly than Ir, Pt and rare earth metal ions.[5–7] Among these the family of copper(I) halides and pseudo-halides is particularly attractive due to its large variety of photophysical properties[7–14] associated with an extremely high structural diversity,[15] which allows to obtain several different compounds starting from the same reagents. This latter feature implies, as a drawback, that the final structure of the coordination polymer based on Cu(I) is difficult to design or in some cases to obtain as pure material due to mixture formation.[16] For instance, there are not less than[14] different structures in the CSD[17] based on CuI and DABCO (diazabicyclo octane) which differ in stoichiometry, nuclearity of the CuI core and nature of encapsulated solvent molecules.[18]

Infinite double chains based on copper halides or pseudo-halides have been investigated for their luminescence[14,19–21] and conductivity properties.[11,22–27] Several papers describe the structures and behavior of CuX pyrazine compounds[14,19,24,28–32] and recently the missing structure of the $[CuI(pyz)]_n$ has been published.[21]

The synthetic conditions, especially the solvent and the stoichiometry ratio between reactants, appear to play a fundamental role in determining the nature of the final product. In general, reactions performed with an excess of ligand favor the formation of low nuclearity compounds such as dimers, while and excess of copper(I) halide promotes the formation of infinite arrangements of CuX. Less explored has been, however, the effect of moving from solution to solid state mechanochemical reaction conditions. In the strive for more sustainable eco-friendly approach to synthetic procedures, the use of solvent-less methods, such as those based on the mechanical mixing of the reactants, has been demonstrated to be attractive alternative. Moreover, the diverse experimental conditions may lead to different results[16,33] which is exactly what we have observed in the case of the reaction of CuI with pyrazine.

With the awareness that the copper iodide reacts easily via mechanochemistry, we have investigated the possibility to obtain and transform the CuI pyrazine compounds upon mechanical and thermal treatments. Moreover, we have explored the possibility of substituting pyrazine with an alternative bridging ligand in coordination polymer formation.

Here we report that the previously known compounds $[Cu_2I_2(pyz)]_n$[31] and $[CuI(pyz)]_n$,[21] can be synthesized by kneading (i.e. solvent drop grinding) and new coordination polymer $[(CuI)_2(pyz)_2]_n$ can be obtained by neat grinding, i.e. in the absence of any solvent. Since $[(CuI)_2(pyz)_2]_n$ is produced only as a microcrystalline powder, the structure was determined by X-ray powder diffraction and it is characterized by the presence of copper iodide dimers bridged by the pyrazine ligands. $[(CuI)_2(pyz)_2]_n$ transforms to the more stable isomer $[CuI(pyz)]_n$ in the presence of solvents or humidity.

We also show that 4-cyanopyridine, (4CN-py), can be used to replace pyrazine affording a the coordination polymer of formula $[(CuI)_2(pyz)(4CN\text{-}pyz)]_n$, which upon thermal treatment loses pyrazine and converts into the known $[(CuI)_4(4CN\text{-}py)_5]$.[34]

Mechanochemical syntheses and structural characterization, interconversion by thermal and mechanical treatments of the products, as well as the outcome of slurry experiments, will be described.

EXPERIMENTAL SECTION

All glassware was dried in an oven set to a temperature of 80°C for 24h prior to use and stripped with N_2 for 15min. All reagents were purchased from Sigma Aldrich and used without further purification. A Retsch MM200 ball mill was used for solid state reaction, the mechano-syntheses were performed in 5 mL steel jars with two steel spheres (Ø=5 mm, 0.505 g) inside, no grinding media has been added. The quantities of the reagents have been adjusted to have a complete conversion of the CuI into the final product, excess of pyrazine can be easily removed by gently heating or under low pressure; all the mechanochemical reactions are considered quantitative as no CuI peaks are visible in the diffraction patterns of the products.

Synthesis of $[Cu_2I_2(pyz)]_n$

<u>Solid state reaction:</u> CuI (0.788 mmol; 0.150 g) and pyrazine (0.394 mmol; 0.031g) were ground together with four drops of acetonitrile for 20 minutes with a frequency of 20 rpm, with a ball to powder mass ratio (BPR) of 10:1.8. The product is presented as a yellow crystalline powder. The

product was washed with acetonitrile, dried under vacuum and analyzed by X-ray powder diffraction.

Reaction in solution: $[Cu_2I_2(pyz)]_n$ was obtained following the procedure described in literature.[31] CuI (300 mg, 1.57 mmol) dissolved in MeCN (20 mL) was added to a stirred solution of pyrazine (pyz) (63 mg, 7.9 mmol) in MeCN (20 mL). A yellow precipitate formed immediately and was filtered off after stirring for 1h. The solid was dried in vacuo and analyzed by X-ray powder diffraction.

Synthesis of $[CuI(pyz)]_n$

Solid state reaction: CuI (1 mmol; 0.190 g) and pyrazine (2 mmol; 0.162g) were ground together with few drops of acetonitrile for 20 minutes with a frequency of 20 rpm (BPR of 10:3.5). The product is a red crystalline powder. The product was washed with acetonitrile, dried under vacuum and analyzed by X-ray powder diffraction.

Solvothermal reaction: The solvothermal reaction used differs from the published one.[21] CuI (0,25 mmol; 0,043 g), pyrazine (1 mmol; 0,080 g) and 15 drops of acetonitrile were placed in 8 mL Teflon-lined steel autoclave and heated to 120 °C for 30 mins and then cool down.

Synthesis of $[(CuI)_2(pyz)_2]_n$

Solid state reaction: CuI (1 mmol; 0.190 g) and pyrazine (1.2 mmol; 0.100g) were ground together for 40 minutes with a frequency of 20 rpm (ball-to-powder ratio BPR of 10:2.9). The product is an orange crystalline powder. It was stored in a dry place to prevent the conversion to the $[CuI(pyz)]_n$ isomer.

CuI reacts with melted pyrazine to produce $[(CuI)_2(pyz)_2]_n$. Regardless from the synthetic process $[(CuI)_2(pyz)_2]_n$ is unstable and the conversion to the red isomer was observed over time.

Synthesis of $[(CuI)_4(4CNpy)_5]_n$

Solid state reaction: CuI (1 mmol; 0.190 g) and 4CN-py (1.5 mmol; 0.156g) were ground together with four drops of acetonitrile for 20 minutes with a frequency of 20 rpm (BPR of 10:3.5). The product is a yellow crystalline powder. The product was washed with acetonitrile, dried under vacuum and analyzed by X-ray powder diffraction.

Reaction in solution: The product of $[Cu_2I_2(pyz)]_n$ was obtained following the procedure described in literature.[34] CuI (0.300 g, 1.57 mmol) dissolved in MeCN (20 mL) was added to a stirred solution of 4-cyanopyridine (4CNpyz) (0.204 g, 2 mmol) in MeCN (20 mL). A yellow precipitate formed immediately and was filtered off after stirring for 1h. The solid was dried in vacuo and analyzed by X-ray powder diffraction.

Synthesis of $[(CuI)_2(4CN\text{-}py)(pyz)]_n$

Solid state reaction: $[(CuI)_2(pyz)]_n$ (1 mmol; 0.115 g) and 4-cianopyridine (2 mmol; 0.052g) were ground together with four drops of acetonitrile for 40 minutes with a frequency of 20 rpm (BPR of 10:1.7). The product is a yellow crystalline powder. The product was washed with acetonitrile, dried under vacuum and analyzed by X-ray powder diffraction.

Crystallization: Single crystals of $[(CuI)_2(4CN\text{-}py)(pyz)]_n$ were obtained by slow evaporation of an acetonitrile solution of $[(CuI)_2(pyz)]_n$ and 4CN-py.

Slurry experiments

A saturated acetonitrile solution of the microcrystalline powder with added pyrazine or Copper iodide, was left stirring for at least 3 days. The powder was filtered and characterized by X-ray powder diffraction.

Thermogravimetric analysis (TGA)

TGA measurements were performed using a Perkin Elmer TGA7 in the temperature range 35-400°C under N_2 gas flow and heating was carried out at 5°C min^{-1}.

X-ray powder diffraction

The data were collected in open air in Bragg–Brentano geometry using Cu-Kα radiation without a monochromator. X-ray powder diffractograms were collected in the 2θ range of 5–50° using a Panalytical X'Pert PRO automated diffractometer equipped with an X'Celerator detector and an Anton Paar TTK 450 system for measurements at a controlled temperature.

Structure determination from powder diffraction

The data of $[(CuI)_2(pyz)_2]_n$ were collected with a Panalytical X'Pert PRO diffractometer equipped with an Pixcel detector in transmission geometry with Cu Kα radiation without a monochromator. The sample was placed in 0.05 mm capillary, the 2θ range 10-85° (step size 0.013°, time/step 200 s, VxA 40 kV x 40 mA).

The pattern was indexed with TOPAS[35], as a triclinic cell with a= 7.2730(3)Å, b=7.2912(3)Å, c=7.9513(2) Å, α=112.297(2)°, β= 109.398(2)°, γ=102.807(2)°. The volume of 337.52(2)Å^3 corresponds to two copper atoms, two iodine atoms and two pyrazine molecules. The structure was solved in P1 space group with simulated annealing and the structure found was converted in the P-1 space group. The asymmetric unit contains one copper atom, one iodine atoms and two half pyrazine molecules. The pyrazine molecules are forced to be on the inversion center by the use of a dummy atoms and the number of degrees of freedom is minimized. The Rietveld refinement was carried in the P-1 space group. A shifted Chebyshev function with 11 parameters and four peaks were used to fit background and an impurity, respectively. TCHZ function was used to fit peak shape. All the hydrogen atoms were fixed in calculated positions. Refinement converged with Rwp = 4.77%; Rp = 3.78% and Rexp =7.19%.

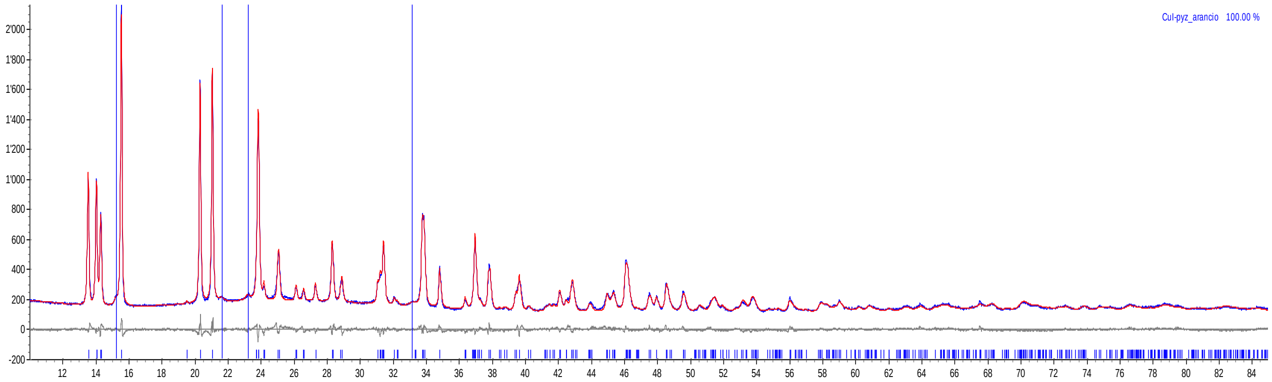

Figure 1. Rietveld refinement of $[(CuI)_2(pyz)_2]_n$. Blue line is the experimental pattern, red line is the calculated pattern, grey line is the difference plot.

Single crystal X-ray Diffraction

SCXRD measurements were performed on an Oxford Xcalibur S diffractometer with Mo-Ka radiation, λ= 0.71073 Å, and monochromator graphite at room temperature.

$[(CuI)_2(4CN\text{-}py)(pyz)]_n$ crystallizes as monoclinic $P2_1/c$ with a= 10.2348(6)Å, b=12.3289(4) Å, c= 8.8309(5) Å and β= 109.605(6)° with volume 1049.73(9)Å^3. SHELX97[36] was used for structure solution and refinement based on F^2. The non-hydrogen atoms were refined anisotropically. Hydrogen atoms bound to carbon atoms were added in calculated positions. The refinement converged to R_1 (F, I >2σ(I)= 0.042 and WR_2 (F^2, all data)= 0.136. The program Mercury[37] was used for all graphical representations and for the calculated powder pattern.

RESULTS AND DISCUSSION

We have reacted copper iodide with pyrazine in solid state (whether kneading or dry) with the aim of investigating the possibility of obtaining new products via alternative synthetic routes with respect to solution. Furthermore we have explored the effect of varying the stoichiometry ratios and solvothermal procedures.

We found that the coordination polymers, $[Cu_2I_2(pyz)]_n$ and $[CuI(pyz)]_n$ can be easily prepared by kneading of CuI and pyrazine in the appropriate stoichiometry ratios, while the absence of solvent, during the milling, allows the formation of the orange product $[(CuI)_2(pyz)_2]_n$. The reactions in solution, on the other hand, yield exclusively yellow $[Cu_2I_2(pyz)]_n$ regardless of the stoichiometry ratio. Red crystals of $[CuI(pyz)]_n$ can be obtained in solvothermal conditions. The results will be described in details the following.

For the sake of the discussion it is worth recalling the salient structural features of the $[Cu_2I_2(pyz)]_n$ and $[CuI(pyz)]_n$, which had been determined by Blake et. and by Malaestean et. al., respectively.[21,38] Both coordination polymers present infinite chain of CuI.

The structure of “yellow” $[Cu_2I_2(pyz)]_n$ is characterized by the presence of double polymeric chains with staircase-like arrangements of CuI in which the copper atoms, in tetrahedral coordination, bind three iodine atoms and one pyrazine molecule (figure 2a). The ligand acts as a bridge between two adjacent chains forming infinite 2D sheets (figure 2b) stacked along the a-axis. The structure of “red” $[CuI(pyz)]_n$ consists of "zig-zag" chains of CuI in which the tetrahedral coordinated copper atoms bind two iodine atoms and two pyrazine molecules. The chains are linked together by the ligands that act as a bridge between two copper atoms forming an infinite 2-D network (figure 3a). The crystal packing reveals the presence of a stacking along the b-axis of the chevron-like 2-D sheets (figure 3b).

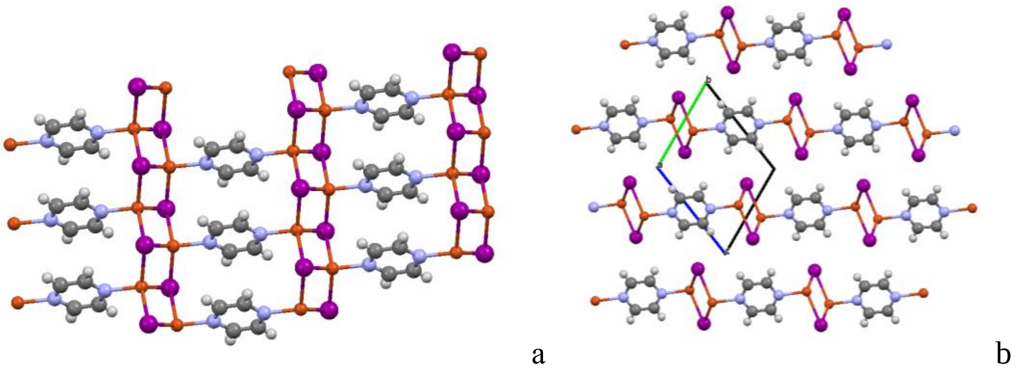

Figure 2. a) The 2-D network made of infinite double CuI chains bridged by the pyrazine molecules in $[Cu_2I_2(pyz)]_n$. b) View along the a axis showing the stacking of the infinite 2D sheets .

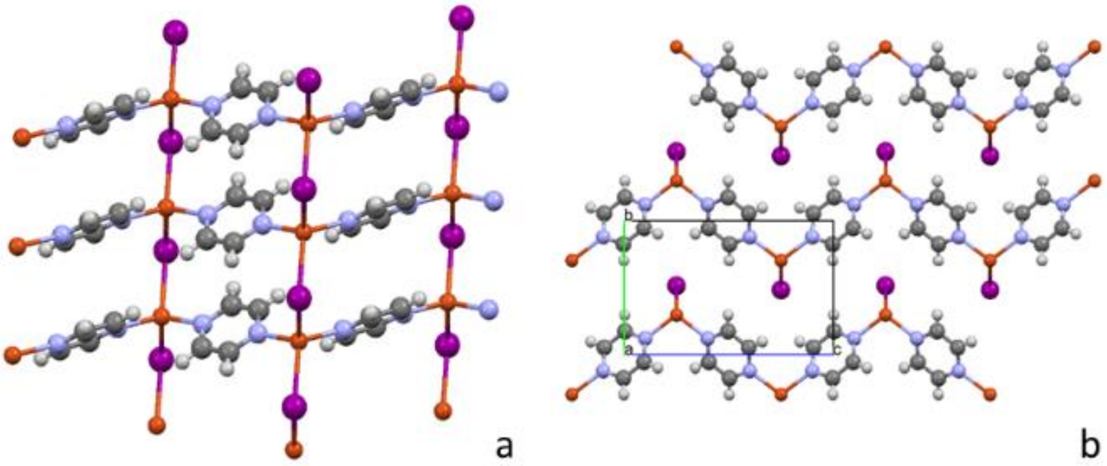

Figure 3. a) The 2-D network made of the infinite single strain CuI chains bridged by the pyrazine molecules in $[CuI(pyz)]_n$. b) View along the a-axis showing the chevron-like 2D sheets.

These features ought to be compared with those of the novel compound, “orange” $[(CuI)_2(pyz)_2]_n$. Owing to the polycrystalline nature of the mechanochemical product, its structure was determined from powder diffraction data. The asymmetric unit consists of one copper atom, one iodine atom and two independent half molecules of pyrazine. The copper atoms present a short Cu-Cu distance (2.648(2) Å) and their tetrahedral coordination is fulfilled by two pyrazine ligands which bridge two other dimers (figure 4a). The overall structure can be described as 2-D coordination polymers stacked one on the others (figure 4b). The $[(CuI)_2(pyz)_2]_n$ presents a void volume of 4.4% (no solvent trapped inside as confirmed by the TGA analysis) and this could explain why it easily converts into the more stable isomer over time, readily in presence of solvent or humidity. The coordination polymer is isostructural with the previously reported $[(CuI)_2(L)_2]_n$ (L= DABCO, and piperazine)[33] which can also be obtained by solid state reaction. It is worth noting that $[(CuI)_2(DABCO)_2]_n$ shows a 3.3% of void volume without, however, making the compound unstable.

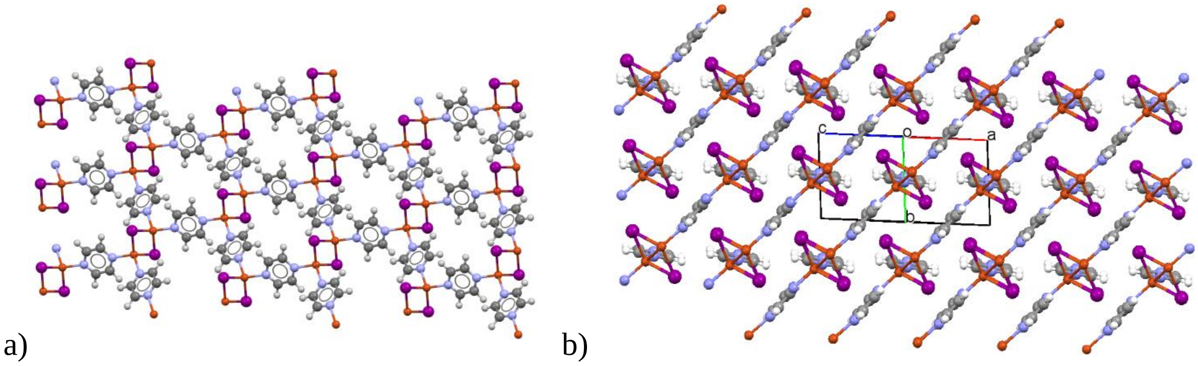

Figure 4. a) The 2-D network made of the CuI dimers bridged by the pyrazine molecules in $[(CuI)_2(pyz)_2]_n$. b) View along the [101] axes which shows the stacking of 2D sheets.

The existence of isomers of CuXL (X=halogen, L=organic ligand) is not unusual, and we have already described some of them.[16,20,39,40] In the reported cases the solvent used during the synthesis drives the formation of one or the other isomer, while for the CuI and pyrazine the presence or absence of the solvent is foundamental for obtaining $[CuI(pyz)]_n$ or $[(CuI)_2(pyz)_2]_n$.

Reversible transformations between $[CuI(pyz)]_n$, $[Cu_2I_2(pyz)]_n$ and $[(CuI)_2(pyz)_2]_n$

We explored the possibilities of interconversion between the three coordination polymers by using different processes such as slurries, thermal and mechanical treatments.

The interconversion between the compounds were easily detected by naked eyes, because they have different color. The purity of the resulting solid phases was confirmed by X-ray powder diffraction (see figure 5).

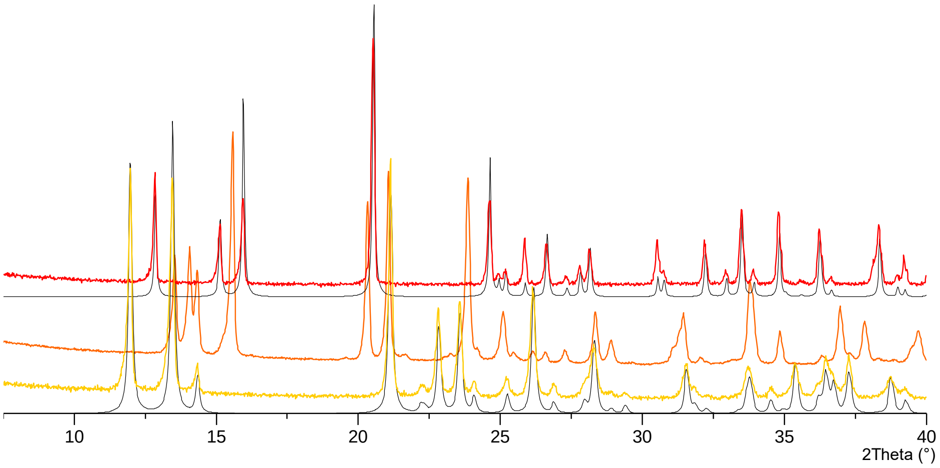

Figure 5. Powder patterns: on top $[CuI(pyz)]_n$ observed (red line) and calculated on the basis of the known structure (underlying black line), $[(CuI)_2(pyz)_2]_n$ observed (orange line, middle); $[Cu_2I_2(pyz)]_n$ observed (yellow line) and calculated on the basis of known structure (underlying black line, bottom).

The TGA analyses of the two isomers have very similar results: in both cases the curves show loss of weight in two equal steps, the first at around 110°C and the second at 240°C (figure 6a). We collected the pattern of the microcrystalline powders with variable temperature X-ray powder diffraction, to understand the conversion. Upon heating the orange $[(CuI)_2(pyz)_2]_n$ is stable up to 100 °C. Above 100°C the compound releases pyrazine and transforms into yellow crystalline $[Cu_2I_2(pyz)]_n$ (figure 6b), which is stable up to 175°C and finally decomposes into CuI. The red $[CuI(pyz)]_n$ shows the same behavior as its isomer and as other isomorphic compounds[30] by releasing one pyrazine at about 110° C and converting into the $[Cu_2I_2(pyz)]_n$ (see figure SI2).

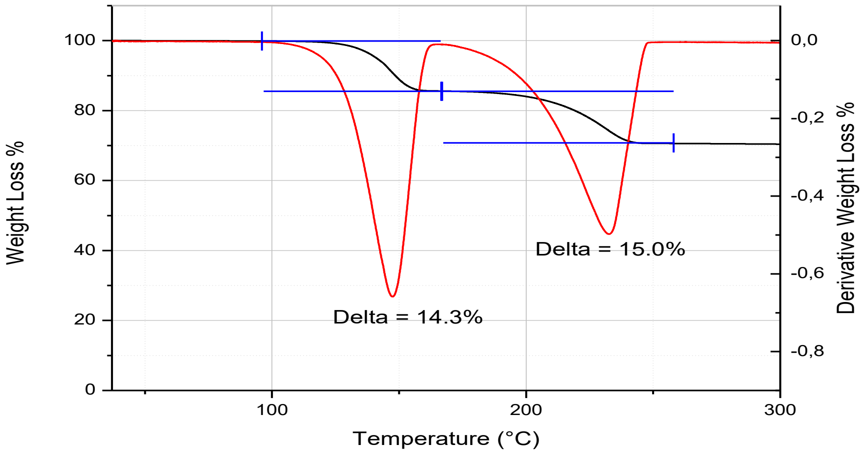

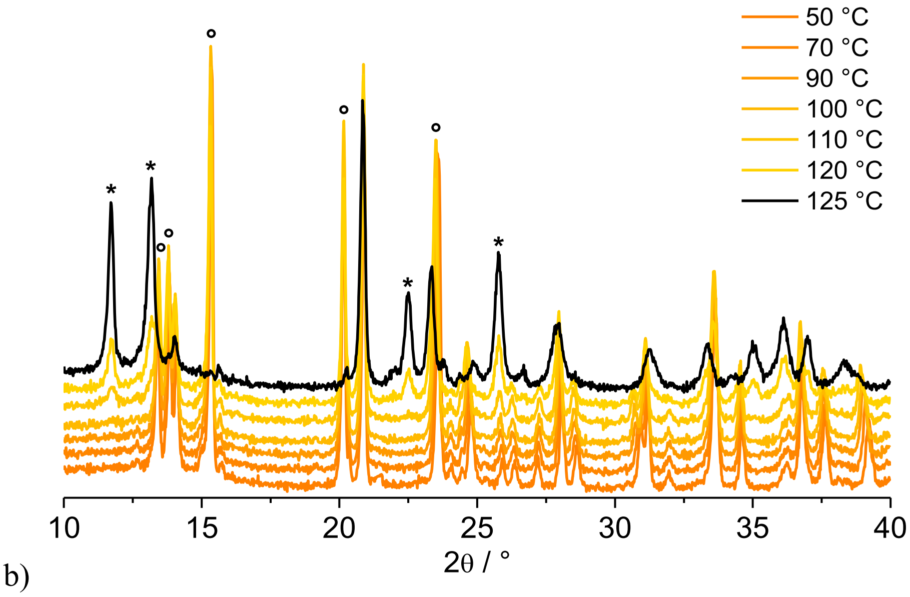

Figure 6. a) TGA analysis for the $[CuI(pyz)]_n$, the black line represents the trend of the weight loss %, the red line represents the derivative weight loss %. b) VT-XRPD measurements for $[(CuI)_2(pyz)_2]_n$, the * indicates the peaks of the starting material while the ° indicates the peaks of $[Cu_2I_2(pyz)]_n$.

All reactions are reversible and by grinding $[Cu_2I_2(pyz)]_n$ with pyrazine (stoichiometry ratio 1:1) the pristine coordination polymer is obtained. As for the reaction in solid state with CuI and pyrazine, the final product depends on the presence of the solvent so that the synthesis by neat grinding of $[Cu_2I_2(pyz)]_n$ with pyrazine (stoichiometry ratio 1:1) yields $[(CuI)_2(pyz)_2]_n$, while $[CuI(pyz)]_n$ is obtained if some drops of acetonitrile are added. As expected, the isomers readily transform into $[Cu_2I_2(pyz)]_n$ by grinding with CuI, while $[(CuI)_2(pyz)_2]_n$ converts into $[CuI(pyz)]_n$ if ground with a drop of solvent or exposed to vapors of solvent. This conversion suggests a higher thermodynamic stability of $[CuI(pyz)]_n$ with respect to the other isomer, which is consistent with the idea that the most closed packed structure is the most stable (density 2.754 vs 2.662 g/cm^3). Scheme 1 summarizes all the possible conversions.

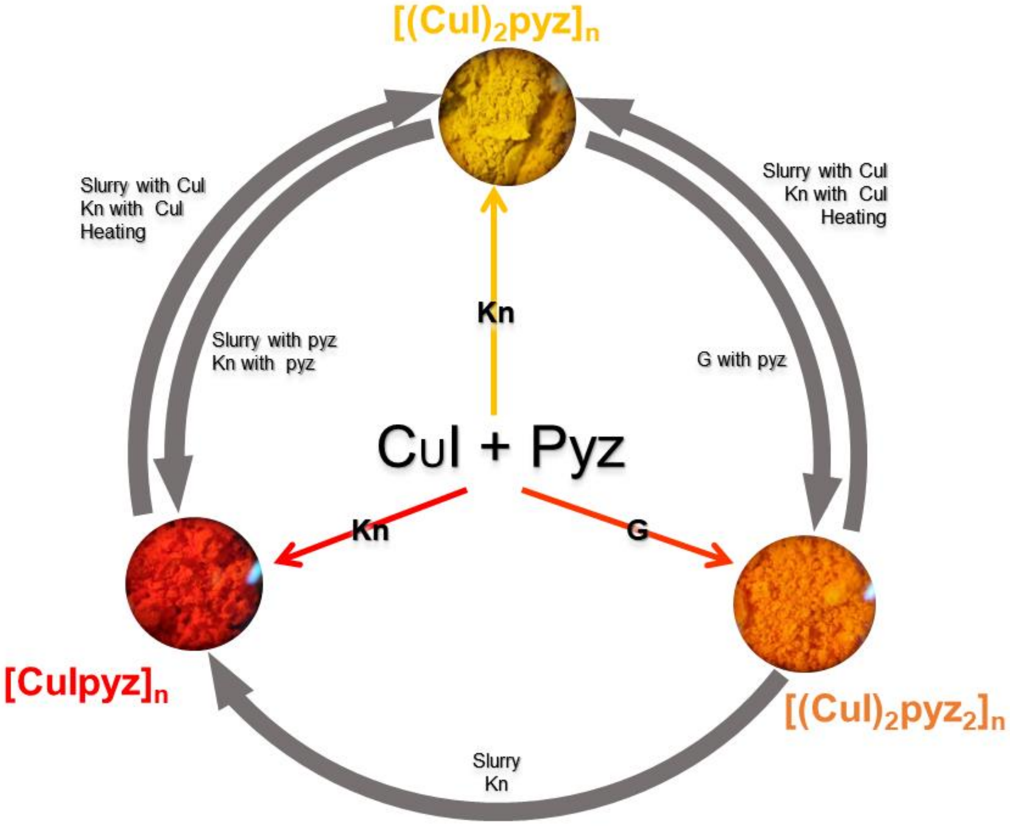

Scheme 1. Summary of the interconversions among the coordination polymers: Kn indicates kneading (liquid assisted grinding with a drop of acetonitrile), G indicates grinding.

Slurries experiments confirmed most of these interconversion processes, but did not allow formation of $[(CuI)_2(pyz)_2]_n$ which can only be obtained in the absence of solvents. For this reason, it is possible to follow the diagram clockwise only by considering the mechanochemical reactions.

Reactions with 4-cyano pyridine

Considering the high degree of versatility of the solid state processes involving CuI, in an attempt to prepare a mixed-ligand compound, we have attempted grinding of $[Cu_2I_2(pyz)]_n$ in the presence of pyrazine and 4-cyanopyridine affording the desired mixed ligand coordination polymer $[(CuI)(4CN\text{-}py)_2py]_n$.

In the literature three structures with CuX (X= Cl, Br, I) and 4-cyanopyridine (4CN-py) are reported. [CuX(4CN-py)]n (X= Cl, Br) forms a single stranded infinite copper halide chain bridged by the organic ligand while for the copper iodide only the unusual $[(CuI)_4(4CN\text{-}py)_5]_n$ is obtained.[34] All attempts to obtain new reaction products by grinding and kneading of CuI and 4CNpy, also with different stoichiometries, invariably afforded only the known compound $[(CuI)_4(4CN\text{-}py)5]_n$.

The structure of the mixed ligand $[(CuI)(4CN\text{-}py)_2py]_n$ is characterized by the presence of Cu_2I_2 dimers with short Cu-Cu distance (2.606(2)Å) bridged by the pyrazine to form a 1-D coordination polymer (figure 7a). The 4-cyanopyridine coordinates the copper atom by the N–pyridine and the –CN group is not involved in any interactions. The infinite chains run along the c axes and the cyanopyridine ligands are interdigitated (figure 7b).

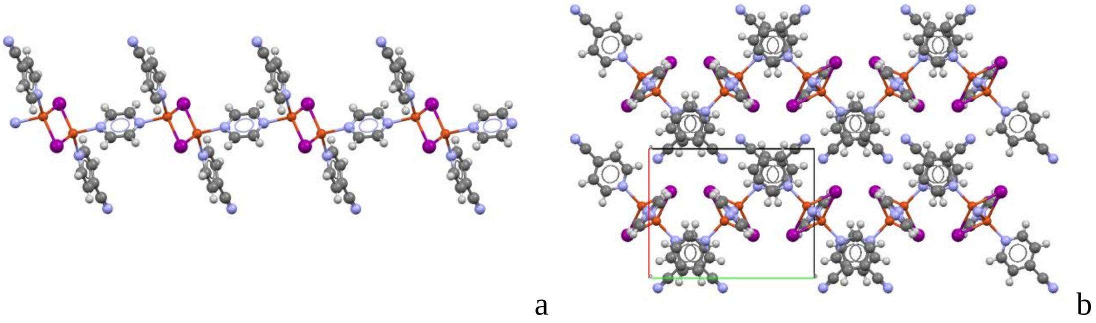

Figure 7. a) The infinite chain of $[(CuI)(4CN\text{-}py)_2py]_n$ with pyrazine bridging the copper iodide dimers and the 4CN-py almost perpendicular to the direction of the chain. b) Packing view along the c axes.

The TGA curve shows a weight loss in different steps while variable temperature diffraction shows that at ca. 120°C $[(CuI)(4CN\text{-}py)_2py]_n$ decomposes to form $[Cu_2I_2(pyz)]_n$ and $[(CuI)_4(4CN\text{-}py)_5]_n$. The mixture is stable up to 150°C when all the 4-CN-py is released and the powder left contains $[Cu_2I_2(pyz)]_n$ and CuI (see figure 8).

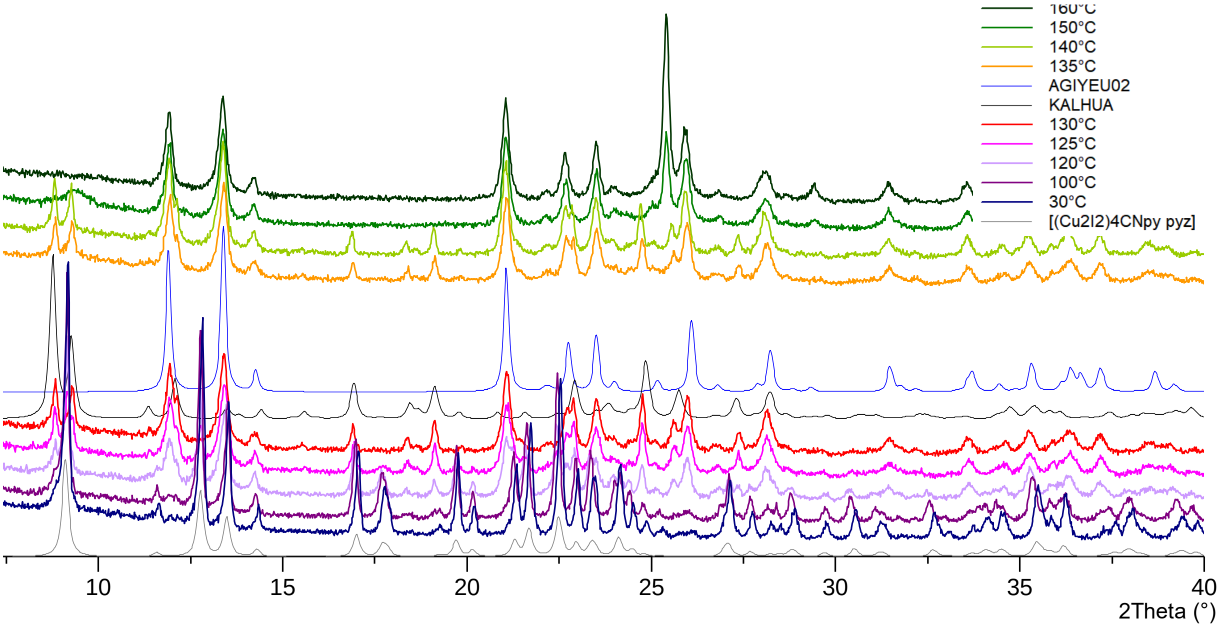

Figure 8. VT-XRPD of $[(CuI)(4CN\text{-}py)_2py]_n$. The sample is stable up to 100°C, at 120° the peaks characteristic of $[Cu_2I_2(pyz)]_n$ and $[(CuI)_4(4CN\text{-}py)_5]_n$ appears. The calculated patterns of the last two compounds are added to the diagram for comparison (labelled AGIYEU02 and KALHUA from the refcode of the CSD). At 150°C the peak at $2\theta = 25$°c is clearly visible.

CONCLUSIONS

Mechanochemical methods have become increasingly popular in the field of crystal engineering and materials scienceref because they allow to explore reaction conditions that do not depend on the solubility of the reactants and/or of the products. The major drawback of a mechanochemical approach, however, remains the difficulty of ascertaining the structural features of the product, which is, necessarily, in the form of a polycrystalline powder ruling out the possibility of collecting single crystal X-ray diffraction data. In these cases structure determination from powder data, possibly combined with other techniques carrying structural information (NMR crystallography,[41,42] Raman spectroscopy[43]) and DFT calculation,[44] can be the only available option to determine the crystal structure.

In this paper we have approached a well known family of compounds, namely the coordination polymers obtained by reaction of CuI and pyrazine, with a mechanochemical method with the awareness that the identification of the nature of the reaction products would have to rely exclusively on powder diffraction data. We were gratified by the discovery not only that the known $[CuIpyz]_n$ compound, obtained by solvothermal synthesis,ref can be easily and quantitatively obtained by kneading, but also that the same solid-state reaction carried out by neat grinding, yielded the previously unknown “orange” compound $[(CuI)_2(pyz)_2]_n$. The structure of $[(CuI)_2(pyz)_2]_n$ has been determined from powder diffraction data and shown to consist of discrete Cu_2I_2 dimers bridged by the pyrazine ligands to form a 2-D network. The structure presents a 4.4% of void space which makes the compound unstable and in presence of solvent or vapor it transforms into its isomer $[CuIpyz]_n$ also over time. We have also thoroughly explored the interconversion relationship between the three CuI derivatives. Scheme 1 summarizes all the possible conversions among the three coordination polymers, via mechanochemistry, thermal treatment and slurry. It is worth stressing that $[(CuI)_2(pyz)_2]_n$ represents a rather extreme example of a compound that can only be obtained by mechanical grinding of the reactants and in complete absence of solvents.

With the aim of expanding this chemistry further, we have also attempted substitution of pyrazine with another bridging ligand, namely 4CN-py, obtaining the novel mixed-ligand compound $[(CuI)(4CN\text{-}py)_2py]_n$ whose complex behavior upon heating has also been rationalized.

In summary, with this paper, we have provided further evidence of the importance of testing solvent-free non-solution methods of preparation also within the area of coordination polymer chemistry with the awareness that structure determination can nowadays be tackled successfully by powder diffraction methods. We have shown that this approach allows not only to move in a “green” synthetic direction but also to discover compounds which would not be otherwise accessible by solution methods.

SUPPORTING INFORMATION

Emission and excitation spectra of $[(CuI)_2(pyz)_2]_n$

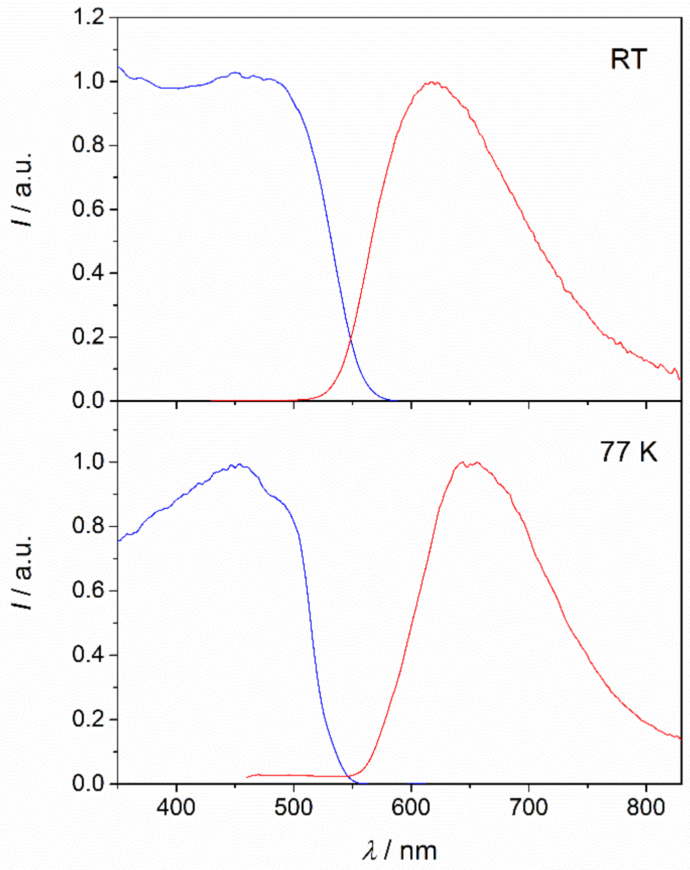

Figure SI 1: Normalized corrected emission (red, λ_{exc} = 400 nm) and excitation (blue, λ_{em} = 670 nm) spectra of $[(CuI)_2(pyz)_2]n$ at room temperature (top) and at 77 K (bottom).

The emission and excitation spectra were obtained with an Edinburgh Instruments FLS920 spectrometer equipped with a Peltier-cooled Hamamatsu R928 PMT (200-850 nm). To record the 77 K luminescence spectra, samples were placed in quartz tubes (2 mm inner diameter) and inserted into a special quartz Dewar flask filled with liquid nitrogen.

Variable temperature X-ray powder diffraction

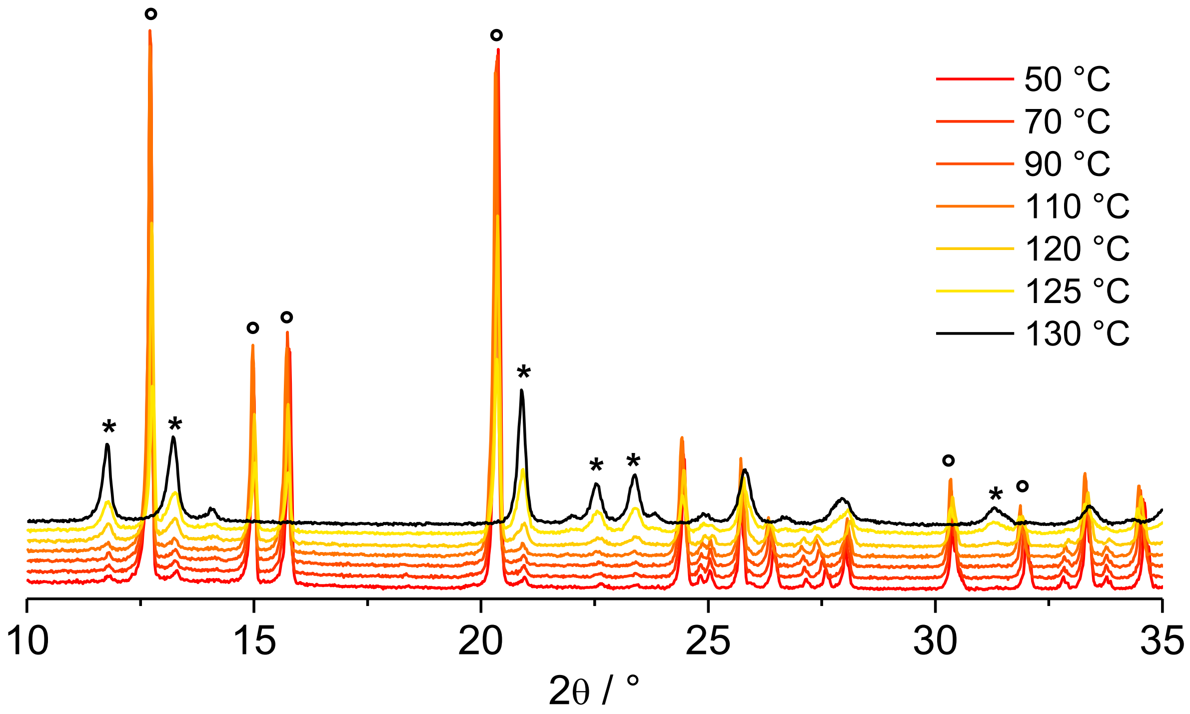

Figure SI2. VT-XRPD for the [CuI(pyz)]$_n$. with the * indicated the characteristic peak of the red [CuI(pyz)]$_n$, and ° indicates the peaks of [Cu$_2$I$_2$(pyz)]$_n$.

REFERENCES

(1) Zhang, S.; Yang, Q.; Liu, X.; Qu, X.; Wei, Q.; Xie, G.; Chen, S.; Gao, S. High-Energy Metal–organic Frameworks (HE-MOFs): Synthesis, Structure and Energetic Performance. *Coord. Chem. Rev.* **2016**, *307*, 292–312.

(2) Li, B.; Wen, H.-M.; Cui, Y.; Zhou, W.; Qian, G.; Chen, B. Emerging Multifunctional Metal-Organic Framework Materials. *Adv. Mater.* **2016**, *28* (40), 8819–8860.

(3) Zhang, H.; Liu, G.; Shi, L.; Liu, H.; Wang, T.; Ye, J. Engineering Coordination Polymers for Photocatalysis. *Nano Energy* **2016**, *22*, 149–168.

(4) Mazzeo, P. P.; Maini, L.; Braga, D.; Valenti, G.; Paolucci, F.; Marcaccio, M.; Barbieri, A.; Ventura, B. Switch On/Switch Off Signal in an MOF-Guest Crystalline Device. *Eur. J. Inorg. Chem.* **2013**, *2013* (25),

4459–4465.

(5) Volz, D.; Wallesch, M.; Flechon, C.; Danz, M.; Verma, A.; Navarro, J. M.; Zink, D. M.; Brase, S.; Baumann, T. From Iridium and Platinum to Copper and Carbon: New Avenues for More Sustainability in Organic Light-Emitting Diodes. *Green Chem.* **2015**, *17* (4), 1988–2011.

(6) Barbieri, A.; Accorsi, G.; Armaroli, N. Luminescent Complexes beyond the Platinum Group: The d(10) Avenue. *Chem. Commun.* **2008**, No. 19, 2185–2193.

(7) Leitl, M. J.; Zink, D. M.; Schinabeck, A.; Baumann, T.; Volz, D.; Yersin, H. Copper(I) Complexes for Thermally Activated Delayed Fluorescence: From Photophysical to Device Properties. *Topics in Current Chemistry*. Springer International Publishing June **2016**, p 25.

(8) Cariati, E.; Lucenti, E.; Botta, C.; Giovanella, U.; Marinotto, D.; Righetto, S. Cu(I) Hybrid Inorganic-Organic Materials with Intriguing Stimuli Responsive and Optoelectronic Properties. *Coordination Chemistry Reviews*. Elsevier January 1, **2016**, pp 566–614.

(9) Ford, P. C.; Cariati, E.; Bourassa, J. Photoluminescence Properties of Multinuclear Copper(I) Compounds. *Chem. Rev.* **1999**, *99* (12), 3625–3648.

(10) Zink, D. M.; Bergmann, L.; Ambrosek, D.; Wallesch, M.; Volz, D.; Mydlak, M. Singlet Harvesting Copper-Based Emitters: A Modular Approach towards next-Generation OLED Technology. *Transl. Mater. Res.* **2014**, *1* (1), 15003.

(11) Maini, L.; Braga, D.; Mazzeo, P. P.; Maschio, L.; Rerat, M.; Manet, I.; Ventura, B. Dual Luminescence in Solid CuI(Piperazine): Hypothesis of an Emissive 1-D Delocalized Excited State. *Dalt. Trans.* **2015**, *44* (29), 13003–13006.

(12) Kobayashi, A.; Kato, M. Stimuli-Responsive Luminescent Copper(I) Complexes for Intelligent Emissive Devices. *Chem. Lett.* **2017**, *46* (2), 154–162.

(13) Yersin, H.; Czerwieniec, R.; Shafikov, M. Z.; Suleymanova, A. F. TADF Material Design: Photophysical Background and Case Studies Focusing on CuI and AgI Complexes. *ChemPhysChem*. December **2017**, pp 3508–3535.

(14) Khatri, N. M.; Pablico-Lansigan, M. H.; Boncher, W. L.; Mertzman, J. E.; Labatete, A. C.; Grande, L. M.; Wunder, D.; Prushan, M. J.; Zhang, W.; Halasyamani, P. S.; et al. Luminescence and Nonlinear Optical Properties in Copper(I) Halide Extended Networks. *Inorg. Chem.* **2016**, *55* (21), 11408–11417.

(15) Peng, R.; Li, M.; Li, D. Copper(I) Halides: A Versatile Family in Coordination Chemistry and Crystal Engineering. *Coordination Chemistry Reviews*. Elsevier, **2010**, pp 1–18.

(16) Maini, L.; Mazzeo, P. P.; Farinella, F.; Fattori, V.; Braga, D. Mechanochemical Preparation of Copper Iodide Clusters of Interest for Luminescent Devices. *Faraday Discuss.* **2014**, *170* (0), 93–107.

(17) Groom, C. R.; Bruno, I. J.; Lightfoot, M. P.; Ward, S. C. The Cambridge Structural Database. *Acta Crystallogr. Sect. B Struct. Sci. Cryst. Eng. Mater.* **2016**, *72* (2), 171–179.

(18) FEVNOL, GUPBEZ01, GUPBEZ02, IQEDOY, IQEDUE, LIRVOY, LIWDIF, NEYYOG, OLUTEV, RIPKEH,

UMUXAC, WUZDOL, W. FEVNOL,GUPBEZ01, GUPBEZ02, IQEDOY,IQEDUE, LIRVOY, LIWDIF, NEYYOG, OLUTEV, RIPKEH, UMUXAC, WUZDOL, WUZFAZ.

(19) Pospisil, J.; Jess, I.; Näther, C.; Necas, M.; Taborsky, P. Luminescence Properties of "Double-Stranded Staircase" Copper(I) Halide Coordination Polymers with N-Containing Ligands. *New J. Chem.* **2011**, *35* (4), 861–864.

(20) Farinella, F.; Maini, L.; Mazzeo, P. P.; Fattori, V.; Monti, F.; Braga, D. White Luminescence Achieved by a Multiple Thermochromic Emission in a Hybrid Organic–inorganic Compound Based on 3-Picolylamine and Copper(I) Iodide. *Dalt. Trans.* **2016**, *45* (44), 17939–17947.

(21) Malaestean, I. L.; Kravtsov, V. C.; Lipkowski, J.; Cariati, E.; Righetto, S.; Marinotto, D.; Forni, A.; Fonari, M. S. Partial in Situ Reduction of Copper(II) Resulting in One-Pot Formation of 2D Neutral and 3D Cationic Copper(I) Iodide–Pyrazine Coordination Polymers: Structure and Emissive Properties. *Inorg. Chem.* **2017**, *56* (9), 5141–5151.

(22) Mateo-Martí, E.; Welte, L.; Amo-Ochoa, P.; Sanz Miguel, P. J.; Gómez-Herrero, J.; Martín-Gago, J. A.; Zamora, F.; Zamora, F.; Mu, Z. C.; Yang, G. D. Direct Evidence of Nanowires Formation from a Cu(I) Coordination Polymer. *Chem. Commun.* **2008**, *13* (8), 945–947.

(23) Hassanein, K.; Amo-Ochoa, P.; Gómez-García, C. J.; Delgado, S.; Castillo, O.; Ocón, P.; Martínez, J. I.; Perles, J.; Zamora, F. Halo and Pseudohalo Cu(I)-Pyridinato Double Chains with Tunable Physical Properties. *Inorg. Chem.* **2015**, *54* (22), 10738–10747.

(24) Troyano, J.; Perles, J.; Amo-Ochoa, P.; Zamora, F.; Delgado, S. Strong Luminescent Copper(i) Halide Coordination Polymers and Dinuclear Complexes with Thioacetamide and N,N′-Donor Ligands. *CrystEngComm.* **2016**, *18* (10), 1809–1817.

(25) Hassanein, K.; Conesa-Egea, J.; Delgado, S.; Castillo, O.; Benmansour, S.; Martínez, J. I.; Abellán, G.; Gõmez-García, C. J.; Zamora, F.; Amo-Ochoa, P. Electrical Conductivity and Strong Luminescence in Copper Iodide Double Chains with Isonicotinato Derivatives. *Chem. - A Eur. J.* **2015**, *21* (48), 17282–17292.

(26) Gallego, A.; Castillo, O.; Gómez-García, C. J.; Zamora, F.; Delgado, S. Electrical Conductivity and Luminescence in Coordination Polymers Based on Copper(I)-Halides and Sulfur-Pyrimidine Ligands. *Inorg. Chem.* **2012**, *51* (1), 718–727.

(27) Amo-Ochoa, P.; Hassanein, K.; Gómez-García, C. J.; Benmansour, S.; Perles, J.; Castillo, O.; Martínez, J. I.; Ocón, P.; Zamora, F. Reversible Stimulus-Responsive Cu(I) Iodide Pyridine Coordination Polymer. *Chem. Commun.* **2015**, *51* (76), 14306–14309.

(28) Näther, C.; Jeß, I.; Greve, J. Synthesis and Thermal Properties of the Inorganic-Organic Transition Metal Halogenides CuCl-Pyrazine and Cu2Cl2-Pyrazine. *Polyhedron* **2001**, *20* (9–10), 1017–1022.

(29) Kuhlman, R.; Schimek, G. L.; Kolis, J. W. Inorganic-Organic Composites from Solvothermal Routes: Extended Structures of [CuX(Pyrazine)]$_\infty$(X=CN, Cl, CF_3CO_2), and $Cu(NO_2)_2$(Pyz). *Polyhedron* **1999**, *18*

(10), 1379–1387.

(30) Graham, P. M.; Pike, R. D.; Sabat, M.; Bailey, R. D.; Pennington, W. T. Coordination Polymers of Copper(I) Halides. *Inorg. Chem.* **2000**, *39* (22), 5121–5132.

(31) Blake, A. J.; Brooks, N. R.; Champness, N. R.; Cooke, P. A.; Crew, M.; Deveson, A. M.; Hanton, L. R.; Hubberstey, P.; Fenske, D.; Schröder, M. Copper(I) Iodide Coordination Networks-Controlling the Placement of (CuI)[Infinity] Ladders and Chains within Two-Dimensional Sheets. *Cryst. Eng.* **1999**, *2* (2–3), 181–195.

(32) Cottam, J. R. A.; Steel, P. J. The Synthesis and Crystal Structures of 'Necklace' 1-D Coordination Polymers with Cu_2I_2 Nodes and 'Extended-Reach' Heterocyclic Bridging Ligands. *Inorganica Chim. Acta* **2014**, *413* (0), 160–165.

(33) Braga, D.; Grepioni, F.; Maini, L.; Mazzeo, P. P.; Ventura, B. Solid-State Reactivity of Copper(i) Iodide: Luminescent 2D-Coordination Polymers of CuI with Saturated Bidentate Nitrogen Bases. *New J. Chem.* **2011**, *35* (2), 339–344.

(34) Graham, A. J.; Peter, A. I. B.; Kildeaa, D.; Allan, H. Lewis-Base Adducts of Group 11 Metal(I) Compounds. XLVI. Synthesis and Conformational Systematics of Some Novel Polymeric Adducts of Pyridine-4-Carbonitrile with Copper(I) Halides. *Aust. J. Chem.* **1989**, *42* (1), 177–184.

(35) Coelho, A. A. TOPAS-Academic. version 4. Coelho Software: Brisbane, Australia **2006**.

(36) Sheldrick, G. M. SHELX97. *SHELX97* **1997**, University of Göttingen, Germany.

(37) Macrae, C. F.; Bruno, I. J.; Chisholm, J. A.; Edgington, P. R.; McCabe, P.; Pidcock, E.; Rodriguez-Monge, L.; Taylor, R.; van de Streek, J.; Wood, P. A. Mercury CSD 2.0 – New Features for the Visualization and Investigation of Crystal Structures. *J. Appl. Crystallogr.* **2008**, *41* (2), 466–470.

(38) Blake, A. J.; Brooks, N. R.; Champness, N. R.; Crew, M.; Deveson, A.; Fenske, D.; Gregory, D. H.; Hanton, L. R.; Hubbersteya, P.; Schröder, M. Topological Isomerism in Coordination Polymers. *Chem. Commun.* **2001**, *1* (16), 1432–1433.

(39) Maini, L.; Braga, D.; Mazzeo, P. P.; Ventura, B. Polymorph and Isomer Conversion of Complexes Based on CuI and PPh_3 Easily Observed via Luminescence. *Dalt. Trans.* **2012**, *41* (2), 531–539.

(40) Braga, D.; Maini, L.; Mazzeo, P. P.; Ventura, B. Reversible Interconversion between Luminescent Isomeric Metal-Organic Frameworks of $[Cu_4I_4 (DABCO)_2]$ (DABCO=1,4-Diazabicyclo[2.2.2]Octane). *Chem. - A Eur. J.* **2010**, *16* (5), 1553–1559.

(41) Dudenko, D. V.; Williams, P. A.; Hughes, C. E.; Antzutkin, O. N.; Velaga, S. P.; Brown, S. P.; Harris, K. D. M. Exploiting the Synergy of Powder X-Ray Diffraction and Solid-State NMR Spectroscopy in Structure Determination of Organic Molecular Solids. *J. Phys. Chem. C* **2013**, *117* (23), 12258–12265.

(42) Watts, A. E.; Maruyoshi, K.; Hughes, C. E.; Brown, S. P.; Harris, K. D. M. Combining the Advantages of Powder X-Ray Diffraction and NMR Crystallography in Structure Determination of the Pharmaceutical Material Cimetidine Hydrochloride. *Cryst. Growth Des.* **2016**, *16* (4), 1798–1804.

(43) Cappuccino, C.; Mazzeo, P. P.; Salzillo, T.; Venuti, E.; Giunchi, A.; Della Valle, R. G.; Brillante, A.; Bettini, C.; Melucci, M.; Maini, L. A Synergic Approach of X-Ray Powder Diffraction and Raman Spectroscopy for Crystal Structure Determination of 2,3-Thienoimide Capped Oligothiophenes. *Phys. Chem. Chem. Phys.* **2018**, *20* (5), 3630–3636.

(44) van de Streek, J.; Neumann, M. A. Validation of Molecular Crystal Structures from Powder Diffraction Data with Dispersion-Corrected Density Functional Theory (DFT-D). *Acta Crystallogr. B. Struct. Sci. Cryst. Eng. Mater.* **2014**, *70* (Pt 6), 1020–1032.

CHAPTER 8: SYNTHESYS OF NEW COORDINATION POLYMERS BASED ON DIFFERENT SILVER HALIDES

The described work was initially carried out by Francesco Farinella during is PhD in the Molecular Crystal Engineering group; he performed the starting screening with AgI and the three isomers of picolylamine, solving the structure of the coordination polymers AgI(4pica)]$_n$, [AgI(3pica)]$_n$. While during my studies I determined the structure form powder of AgI(2pica)]$_n$.

Due to the similarities between the different silver halides, we wanted to expand the studio also to AgBr, a salt that is less present in literature.

The photophysical characterization was performed by Dr. Barbara Ventura from ISOF-CNR.

INTRODUCTION

In recent years, the synthesis of coordination polymers and organic-inorganic hybrid materials has had a remarkable development, in view of the interest in the preparation of compounds with different properties. The term “coordination polymer” defines those materials that consist in coordination compound with repeating coordination entities extending in 1, 2, or 3 dimensions.[1,2,3] The advantages of these type of compounds is to combine the typical features of organic and inorganic system in a single new material,[4–6] which allows their utilization from the manufacture of light-emitting devices to that of field-effect transistors.[7]

Researchers have focused the attention on compounds based on metal halides, which are characterized by a great variety of structures and by excellent electrical, optical and magnetic properties.[8]

Good candidates for these applications are the silver halides coordinated with nitrogen ligands: these are interesting for the diversity of structures in which they can be synthesized and which are typically produced by the condensation of tetrahedral units of $[AgX_4]^{3-}$ that can share corners, sides or faces to form structures from 0 to 3 dimensions.[6,8,9]

In the case of silver(I) compounds are often common crystal structure characteristic of organic-inorganic hybrid materials, were the ligand do not partecipate in the polimeric expansion of the network. Those type of materials possess interesting preoperties and have been for years subject of reasearch. Less common are the examples of coordination polymers based on silver(I), and in this category cases based on silver(I) halides are very rare.[10] Both organic-inorganic hybrid materials and coordination polymers based on silver iodide are used for their semiconducting, non-linear optics and luminescence properties.[11,12]

However, usually organic-inorganic hybrid materials has been so far mainly based on the nature of the inorganic components while the role of the organic component is confined to supporting the inorganic architecture so that few applications are usually based on the organic moiety.[13]

It has long been known, also, that the silver salts show an intense luminescence in the solid state, following the exposure to ultraviolet light and in particular at low temperatures. This phenomenon has proved to be particularly pronounced for crystal structures with short contacts between silver atoms. This feature is commonly referred to by the term "argentophilic interaction" and is associated to all compounds where the distance between two silver atoms is less than 3.44 Å.[11]

A problem in the synthesis of hybrid or coordination polymers derivatives of AgI and AgBr is the poor solubility (K_{PS} AgI≈ $8\cdot10^{-17}$; K_{PS} AgBr≈ $5\cdot10^{-13}$) in most of the common solvents. In some case this problem can be partially overcome by using a rich solution of X- ions to favor the formation of the complex $[AgX_4]^{3-}$, even if this involves a reduction of dimensionality of the hybrid.[12] In the literature, several new compounds have been obtained by solvothermal synthesis. However, one of the most convenient procedure to overcome insolubility, is the use of mechanochemistry.

Also the use of a liquid ligand could promote the product formation, so we have exploited the liquid nature of three isomers 2, 3 and 4 (aminomethyl)pyridine (or picolylamine, hereafter 2-pica, 3-pica, 4-pica) to act both as a ligand and as a solvent, in the attempt to bring the silver halides in solution directly while reacting.

Silver Iodide

Two different synthetic procedures were followed to obtain the CPs: i) liquid assisted grinding (kneading) of AgI with pica and (ii) a solid-liquid reaction both performed without any further solvent added. The solid-liquid reaction produced needle-like crystals suitable for single crystal X-ray diffraction (SCXRD) for $AgI(4pica)]_n$, $[AgI(3pica)]_n$, and a crystalline powder in the case of $[AgI(2pica)]_n$, while the kneading produced crystalline powders with all ligands and no decomposition was observed.

The crystal structures of $[AgI(4pica)]_n$, $[AgI(3pica)]_n$ were easily determined by single crystal X-ray diffraction, and the structures are characterized by infinite double chains.

For $[AgI(2pica)]_n$ the crystalline powder was measured by powder X-ray diffraction (XRPD) and indexed with a plausible cell which is consistent with the presence of an infinite double chain similar to the other two compounds, and then the structure was solved from the powder diffractogram *via* a simulated annealing method.

It is worth noting that in all structures the ligands coordinate only the amino group, at variance with the compounds with 3pica and CuI where both nitrogen atoms are involved in the coordination.[13]

In the case of $AgI(3pica)]_{n,}$ the synthesis of big crystals and the presence of AgI infinite chains, prompted us to perform electrical conduction measurements. The samples exhibit insulating behaviour at room temperature, in air spanning the applied voltage the range 0-110V. Furthermore, a spectroscopic characterization of the crystals has been carried on, both at room and at low temperature (T=77K), resulting in a not detectable luminescence signal.

RESULTS AND DISCUSSION

Crystal structure of $[AgI(4pica)]_n$

The crystalline structure of $[AgI(4pica)]_n$ is characterized by a double chain of AgI units where each silver cation adopts a distorted tetrahedral geometry to connect with three iodine atoms and one nitrogen atom of the amino group. Only one nitrogen atom coordinates the cations and the ligand is almost perpendicular to the chain. The crystalline packing shows an herringbone geometry of the chains with the aromatic N atom pointing directly toward the amino group leading to the formation of H-bonds rather than coordination bonds with silver atoms (figure 1). Along the same chain the ligands are parallel to each other with a distance between the aromatic centroids of 4.466 Å, which is too long for intramolecular π-π interactions. The silver atoms are correlated by inversion centers within the pairs Ag1-Ag1, with distances of 3.128 Å and 2.941 Å which suggests the presence of argentophilic interactions ($d_{Ag\text{-}Ag} < 3.44$Å).[11]

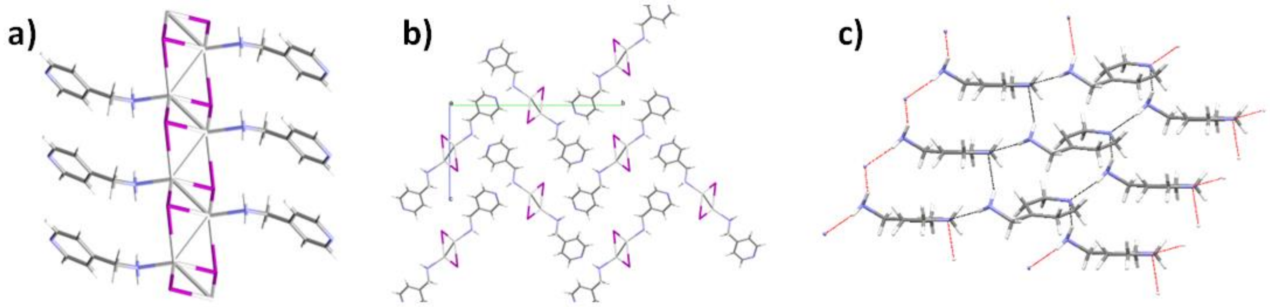

Figura 1. a) double chain of AgI units b) herringbone geometry, c) H-bonds between the N and the amino group.

Crystal structure of [AgI(3pica)]ₙ

The crystalline structure of [AgI(3pica)]$_n$ is very similar to that of [AgI(4pica)]$_n$ and showing a double chains of AgI where the tetrahedral coordination of Ag is fulfilled by three adjacent iodide atom and the ligand, again the ligand coordinate the metal atom only with the amino group. The asymmetric unit is made of two independent molecules of AgI(3pica). The crystalline packing shows that the aromatic N points towards the amino group leading to the formation of H-bonds with a slightly distorted herringbone geometry due to the non-linear configuration of the ligand. Along the same chain the ligands are parallel to each other with a distance between the centroids of 4.568 Å, comparable to the value in [AgI(3pica)]$_n$ and too long for intramolecular π-π interactions. The Ag-Ag distances in both the independent chains are 3.331(3), 3.038(2) and 3.218(2) Å.

The aromatic nitrogen is involved in H-bonds with the amino group of an adjacent chain leading to the formation of ligand chains that stabilized the whole structure. The presence of the H bonds was thought to be very important for the stability of the product or even for the good success of the reactions itself.

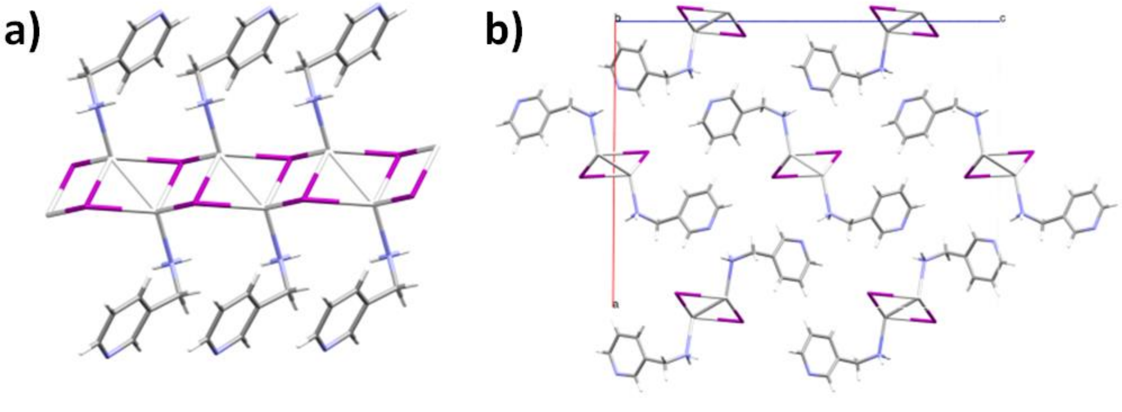

Figure 2. a) double chains of AgI b) crystalline packing

Crystal structure of [AgI(2pica)]$_n$

The crystalline structure of [AgI(2pica)]$_n$ was determined by XRPD and shows a similar arrangement to the previous two coordination compounds. The structure is characterized by a double chain of AgI where the tetrahedral coordination of Ag is fulfilled by three adjacent iodide atoms and the ligand. The asymmetric unit shows the presence of only one silver atom coordinated by the nitrogen of the amino group and the iodine. The aromatic N atom, points, as in previous cases, towards the amino group of an adjacent molecule along the same chain leading to the formation of intramolecular interactions. The distance between the two silver atoms Ag-Ag is 3.179(9) Å and 3.136(9) Å. These distances are consistent to the argentophilic interactions.

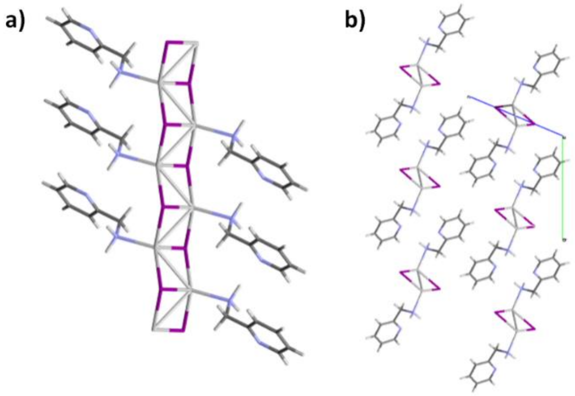

Figure 3. a) double chain of AgI b) packings along a-axis

Silver Bromide

The reaction of AgBr with pica ligands brought to more complex scenario, in fact it was observed, during the screening via mechanochemistry , that the AgBr:pica ratio plays an important role for the product outcome.

Three different synthesis method were used: i) liquid assisted grinding (kneading) of AgBr with pica, (ii) a solid-liquid reaction both performed without any further solvent added, (iii) solvothermal reaction in acetontrile or THF.

We obtained only one compound reacting AgBr and 2pica which is isostructural to the AgI 2pica. While AgBr with 3pica or 4pica can react with different stoichiometry ratio, 1:1 and 2:1.

The reactions are easily controlled *via* mechanochemistry by changing the stoichiometry; however, it was observed that synthesis method influence the product formation. The simple contact between the two reagents always gives the product with the 1:1 ratio with both 3pica and

4pica; the solvothermal reaction with the 3pica produces the 2:1 compound, the same reactions performed with the 4pica gives no coordination polymers but only the formation of the 4pica$^+$Br$^-$ salt.

The preliminary photophysical measurements showed that all the obtained coordination polymers are luminescent, in contrast to the AgI family, however the photophysical behavior appeared peculiar and complex, so other and more specific photophysical analysis are required to explain the emission mechanism.

RESULTS AND DISCUSSION

Crystal structure of [AgBr(2pica)]$_n$

The crystalline structure of [AgBr(2pica)]$_n$ was determined by SCXRD. The packing is isomorphous to the structure of [AgI(2pica)]$_n$. The structure is characterized by a double chain of AgBr (figure 4), previous observed for the AgI compounds, where the tetrahedral coordination of Ag is fulfilled by three adjacent bromide atoms and the ligand. As in the previous cases the ligand coordinates only one silver atoms, and each chain doesn't form intermolecular interactions with the adjacent chains.

The distance between the two silver atoms Ag1-Ag1 is 3.1988(9) Å and 3.2987(9) Å. These distances are consistent to the argentophilic interactions.[11] The crystallographic data are summarized in Table SI2.

[AgBr(2pica)]$_n$, in contrast to the isomorphic iodine compound, presents an evident luminescence under UV lamp (Figure 5).

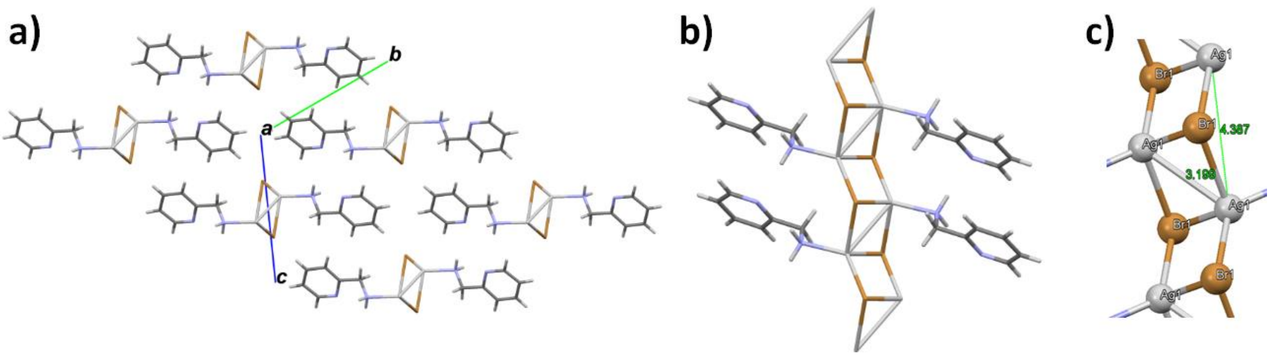

Figure 4. a) crystalline packing along a axis; b)double chains of AgBr; c) detail of Ag-Ag distances.

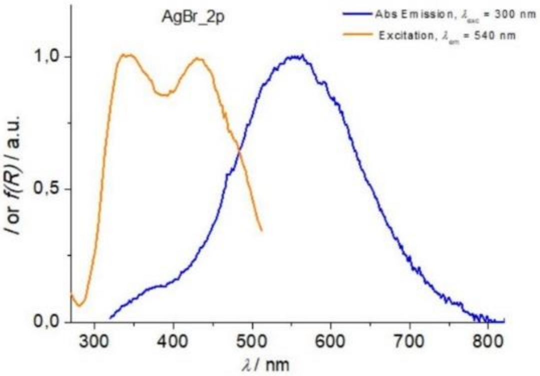

Figure 5. Photophysical characterization of *[AgBr(2pica)]*: in blue is reported the emission (λ_{exc}=300 nm), in yellow the excitation (λ_{em}=540 nm).

Crystal structure of [AgBr(3pica)]$_n$

The crystalline structure of [AgBr(3pica)]$_n$ was determined by SCXRD. The structure is characterized by a single chain of alternated silver and bromine atoms, in a configuration defined "castellated" (figure 6). The tetrahedral coordination of the Ag is fulfilled with two bromine and two ligands. The 3pica coordinates silvers atoms with the piridinic and amino nitrogen, bridging two different chains and forming a two-dimensional network. The connection of two metal atoms by an organic bridge, in an infinite network, is typical of the coordination polymers, where the polymer expansion is due to a coordination bond between an organic and inorganic centres.

Due to the packing in the structure short Ag-Ag distances are not present, however it possesses a bright luminescence under UV light (figure 7).

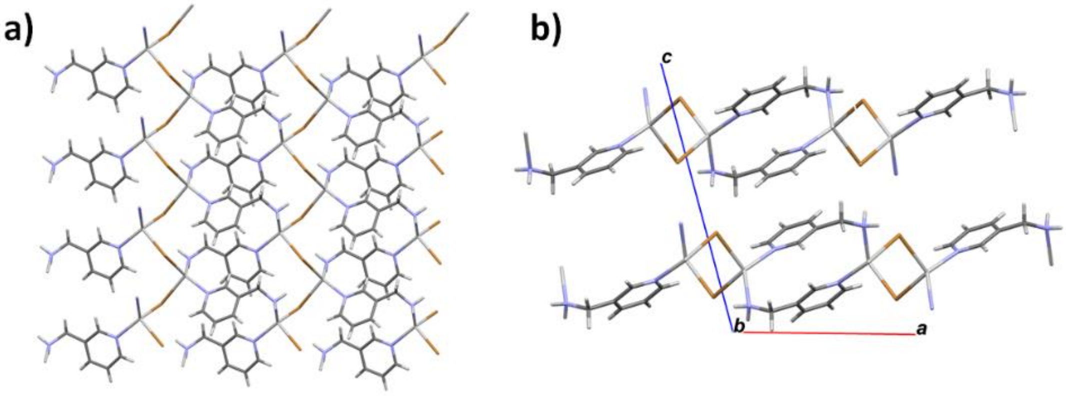

Figure 6. a) single chins of AgBr; b)crystalline packing along b axis.

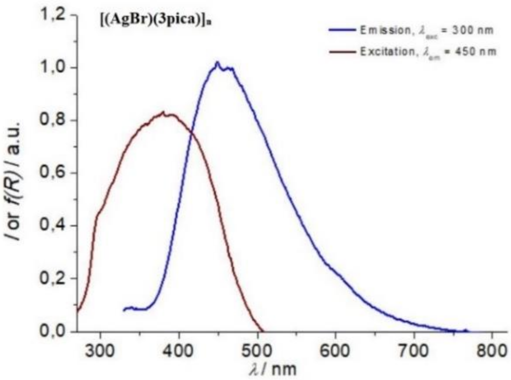

Figure 7. Photophysical charazterization of *[AgBr(3pica)]ₙ*: in blue is reported the emission (λ_{exc}=300 nm), in red the excitation (λ_{em}=450 nm).

Crystal structure of [$(AgBr)_2$(3pica)$]_n$

The crystalline structure of [$(AgBr)_2$(3pica)$]_n$ was determined by SCXRD. The structure is formed by infinite AgBr chains connected by the bridging ligands.

The chains are very peculiar and already described in literature in a coordination complex of AgX (X=Br, Cl) and quinoline[14] where the AgBr conformation is called "Saddle polymer".[15] The inorganic chain presents two different silver atoms with distinctive coordinations (figure 8c). Ag1 completes its tetrahedral coordination with two bromine and two ligands; while Ag2 and Ag3 coordinates only with bromine atoms so they have a pure inorganic character. Moreover Ag2 and Ag3 lays on the 2-fold axis with very short Ag-Ag distances (3.214 Å and 3.071 Å) forming an infinite and linear wire of silver atoms.

The presence of a silver wire could give rise to conductive properties, for the future we have planned to do electrical conduction measurements for testing their application as molecular conductive wires.[16,17]

[$(AgBr)_2$(3pica)$]_n$ is luminescent as reported in figure 9, but further studies should be done to determine the nature of the emissive state.

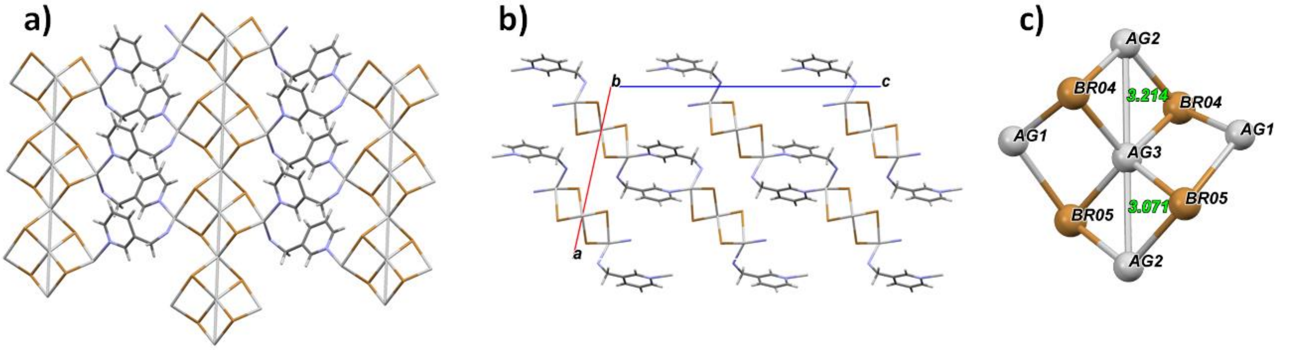

Figure 8. a) “saddle” chains of AgBr; b)crystalline packing along b axis; c) detail of Ag-Ag distances.

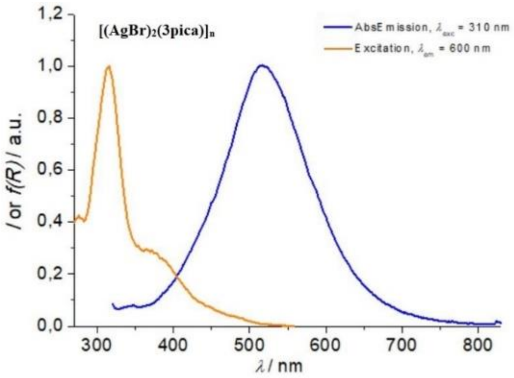

Figure 9. Photophysical charazterization of *$[(AgBr)_2(3pica)]_n$*: in blue is reported the emission (λ_{exc}=310 nm), in yellow the excitation (λ_{em}=600 nm).

Crystal structure of $[AgBr(4pica)]_n$

The crystalline structure of $[AgBr(4pica)]_n$ was determined by SCXRD. The structure presents a different arrangement with respect all the previous obtained coordination polymers since it is characterized by the presence of AgBr dimers (figure 10). The two silver atoms in the dimer present a short Ag-Ag distance (3.193(7) Å), consistent with an argentophilic interaction.[11] The tetrahedral coordination of the silver is completed by two bromine atoms and two ligands, the bridge ligands connected each dimer to other four different dimers creating a two-dimensional coordination polymer. The material is luminescent under UV light (figure 11).

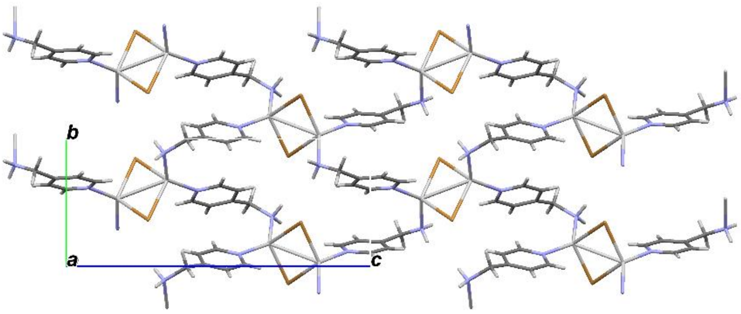

Figure 10. Crystalline packing of $[AgBr(4pica)]_n$ along a axis

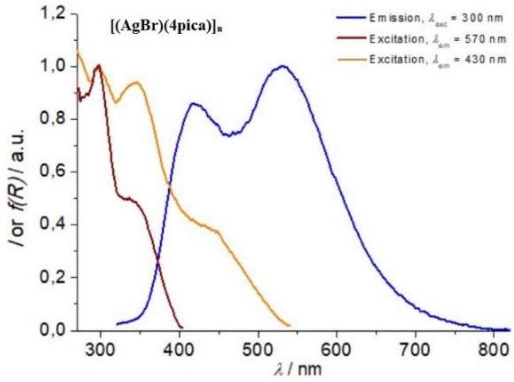

Figure 11. Photophysical characterization of *$[AgBr(4pica)]_n$*: in blue is reported the emission (λ_{exc}=300 nm), in red the excitation in the first emission maximum (λ_{em}=570 nm); in yellow the excitation in the second emission maximum (λ_{em}=430 nm).

Crystal structure of $[(AgBr)_2(4pica)]$

In this case it was impossible to obtain single crystals suitable for SCXRD. Normal solid-liquid reaction always given the $[AgBr(4pica)]_n$, while the solvothermic reaction caused the protonation of the pica and the precipitation of the hydrobromide ligand. The only way to synthesized the material is via mechanochemistry, using AgBr and 4-picolylamine in 2:1 ratio.

Due to the necessary excess of AgBr, the products always contained some unreacted salt, that can be easily exclude during the treatment of the pattern. The diffractogram was indexed using TOPAS5 in the $C222_1$ space group (Table SI2). The crystal cell was then refined with a Pawley refinement (R_{wp}=4.98%). The obtained cell is very similar to $[(AgBr)_2(4pica)]$ and the cell volume is consistent with the stoichiometry of AgBr:4pica 2:1 (considering the multiplicity of the space group). Every attempt to resolve the structure from powder diffraction failed. All the solution obtained, performed with different software (TOPAS, EXPO, DASH) clearly define an area with the high eletron density, due to the presence of heavy atoms, but the position of the atoms is not clearly defined suggesting the presence of some internal disorder in the organic fraction. Other efforts will be performed in the future in order to solve the crystal structure. As the rest of AgBr coordination polymers, [$(AgBr)_2$(4pica)] presents a luminescence under UV light (figure 12).

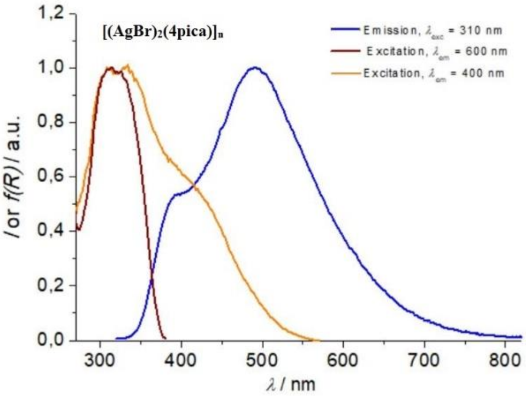

Figure 12. Photophysical characterization of *[$(AgBr)_2$(4pica)]*: in blue is reported the emission (λ_{exc}=310 nm), in red the excitation in the first emission maximum (λ_{em}=600 nm); in yellow the excitation in the second emission maximum (λ_{em}=400 nm).

EXPERIMENTAL SECTION

General

All glassware was dried in an oven set to a temperature of 80°C for 24h prior to use. All reagents were purchased from Sigma Aldrich. In order to minimises the granulometry of AgI and AgBr, and therefore maximise the contact surface iof the reagents, the AgX salts were dissolved in a saturated solution of KI (KBr in the case of AgBr) and than quickly precipitated adding pure water in the solution.

Due to the photosenbility of the AgI and AgBr, all the reactions and measurements have been performed in the dark, to avoid the oxidation of Ag(I) to Ag(0) and the degradation of the products.

Synthetic procedures (silver iodide)

Synthesis of [AgI(4pica)]$_n$: The ligand 4pica (1 mmol; 0.1 mL) was poured into a 5 mL vial with AgI (0.5 mmol; 0.1179 g).After fifteen days needle-like, yellow crystals were obtained and analyzed by Single Crystal Xray Diffraction. AgI (0.5 mmol; 0,1169 g) and 4pica (0,5 mmol; 0,05 mL) were mixed in a 5mL ballmilling jar and grinded for 120 min. The sticky powder obtained was washed with a saturated aqueous solution of KI to remove the possible unreacted AgI and water, dried with vacuum and analyzed by Xray Powder Diffraction.

Synthesis of $[AgI(3pica)]_n$: The ligand 3pica (1 mmol; 0.1 mL) was poured into a 5mL vial with AgI (0,5 mmol; 0.1171 g). After five days colourless, needle-like crystals were obtained and and analyzed by single Crystal X-ray Diffraction. AgI (0.5 mmol; 0,1169 g) and 3pica (0,5 mmol; 0,05 mL) were mixed in a 5mL ballmilling jar and grinded for 120 min. The sticky powder obtained was washed with a saturated aqueous solution of KI to remove the possible unreacted AgI and water, dried with vacuum and analyzed by Xray Powder Diffraction.

Synthesis of $[AgI(2pica)]_n$: The ligand 2pica (1 mmol; 0.1 mL) was poured into a 5 mL vial with di AgI (0.5 mmol; 0.1178 g). After five days little colourless, needle-like crystals were obtained unsuitable for Single Crystal Xray Diffraction. The analysis was performed by Xray Powder Diffraction technique. AgI (0.5 mmol; 0,1169 g) and 2pica (0,5 mmol; 0,05 mL) were mixed in a 5mL ballmilling jar and grinded for 120 min. The sticky powder obtained was washed with a saturated aqueous solution of KI to remove the possible unreacted AgI and water, dried with vacuum and analyzed by Xray Powder Diffraction.

Synthetic procedures (silver bromide)

Synthesis of $[AgBr(2pica)]_n$: The ligand 2pica (1 mmol; 0.1 mL) was poured into a 5 mL vial with AgBr (0.5 mmol; 0.1179 g). After about seven days needle-like, colourless crystals were obtained and analyzed by Single Crystal Xray Diffraction. AgBr (1 mmol; 0.188 g) and 4pica (1 mmol; 1 mL) were mixed in a 7mL ballmilling jar and grinded for 120 min. The obtained powder appeared dry and it was analyzed by XRPD without any further purification.

Synthesis of $[AgBr(3pica)]_n$: The ligand 3pica (2 mmol; 0.2 mL) was poured into a 5mL vial with AgBr (1 mmol; 0.188 g). After about seven days colourless, needle-like crystals were obtained and and analyzed by single Crystal Xray Diffraction. AgBr (1 mmol; 0,188 g) and 3pica (2 mmol; 0,2 mL) were mixed in a 7mL ballmilling jar and grinded for 120 min. The sticky powder obtained was washed with acetonitrile to remove the possible unreacted 3pica, and then analyzed by X-ray Powder Diffraction.

Synthesis of $[(AgBr)_2(3pica)]_n$: AgBr (2 mmol; 0,376 g) and 3pica (1 mmol; 0,1 mL) were mixed in a 7mL ballmilling jar and grinded for 120 min. The obtained product was dry enough for the analysis without further purificaton and then analyzed by X-ray Powder Diffraction, the diffractograms showed residues of unreacted AgBr. The ligand 3pica (1 mmol; 0.1 mL) was poured into a 5mL vial with AgBr (0.5 mmol; 0.094 g) and 2 mL of a solvent (THF or acetonitrile), the vial was insert in a teflon jar and the into a solvothermic reactor. The sealed reactor was put into the oven at 90°C for 24h, after the reaction time the temperature has been lowered by 9°C/h until room temeprature. The obtained crystals were washed with acetonitrile and then analyzed by SCXRD.

Synthesis of $[AgBr(4pica)]_n$: The ligand 4pica (1 mmol; 0.1 mL) was poured into a 5mL vial with AgBr (0.5 mmol; 0.094 g). After fifteen days some small colourless crystal has been formed in the vial, the crystals were washed vith acetonitrile and then analyzed by SCXRD. AgBr (1 mmol; 0,188 g) and 4pica (2 mmol; 0,2 mL) were mixed in a 7mL ballmilling jar and grinded for 120 min. The obtained product was washed with acetonitrle and then analyzed by X-ray Powder Diffraction, the diffractograms showed residues of unreacted AgBr.

Synthesis of $[(AgBr)_2(4pica)]$: AgBr (2 mmol; 0,376 g) and 4pica (1 mmol; 0,1 mL) were mixed in a 7mL ballmilling jar and grinded for 120 min. The obtained product analyzed by X-ray Powder Diffraction without further purification, the diffractograms showed residues of unreacted AgBr.

Crystal structure determination from single-crystal X-ray diffraction

Crystal data from single crystals were collected on an Oxford Xcalibur S with MoKα radiation, λ 0.71073 Å, monochromator graphite.

Crystal data and details of for $[AgI(3pica)]_n$ and $[AgI(4pica)]_n$ are summarized in Table SI1. SHELX97[18] was used for the structure solution and refinement based on F2. Non-hydrogen atoms were refined anisotropically.

Crystal data and details of $[AgBr(2pica)]_n$, $[AgBr(3pica)]_n$, $[(AgBr)_2(3pica)]_n$ and $[AgBr(4pica)]_n$ are summarized in Table SI2. SHELXT[19] was used for the structure solution and refinement based on F2. Non-hydrogen atoms were refined anisotropically.

Crystal cell determination from powder diffraction

The diffraction pattern of $[AgI(3pica)]_n$ and $[AgI(4pica)]$ were collected with a Panalytical X'Pert PRO diffractometer equipped with a Pixcel detector in trasmission geometry using CuKα radiation, λ= 1,541874 Å, without monochromator. The sample was loaded in a 0.5 mm glass capillary; strumental parameters: step size 0.0167°, time per step 100 sec, VxA 40x40, four consecutive collections were recorded and than merged togheter.

The data analysys was performed by the software TOPAS 5[20], a Chebyshev function and a pseudo Voigt (TCHZ type) were used to fit the background and the peak shape respectively.

In the case of [AgI(3pica)]$_n$, we performed a complete the structure determination in direct space and a final Rietveld refinement (figure 13). All the hydrogen atoms were fixed in calculated position.

For [AgI(4pica)] we performed the pattern indexing and the Pawley refinement (figure 14).

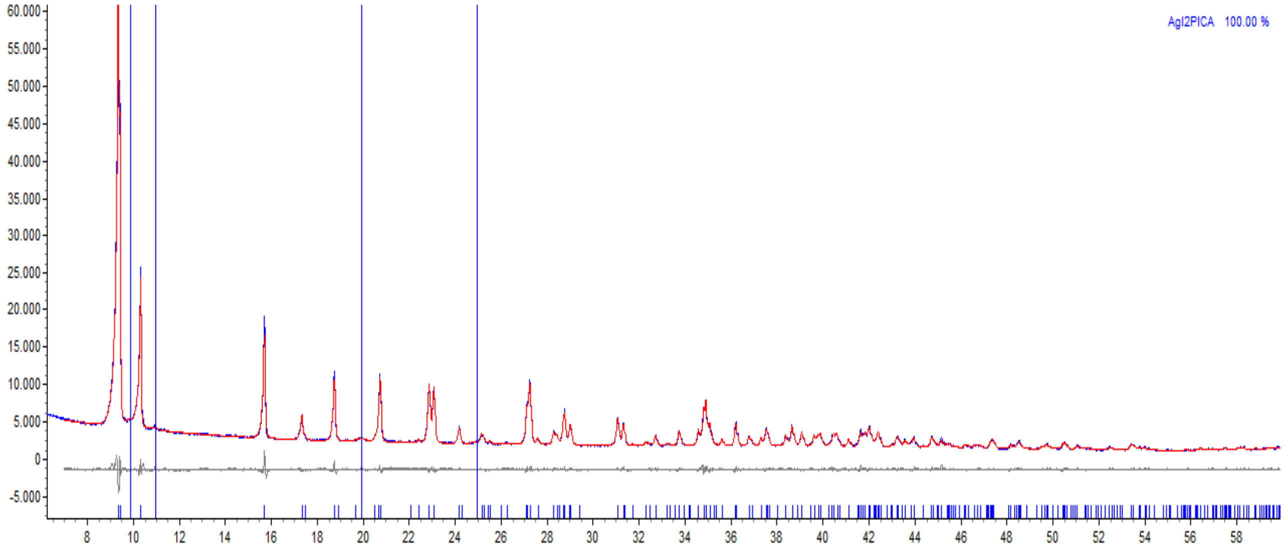

Figure 13. Rietveld refinement of the [AgI(2pica)]$_n$ structure (2θ range= 3-60°)

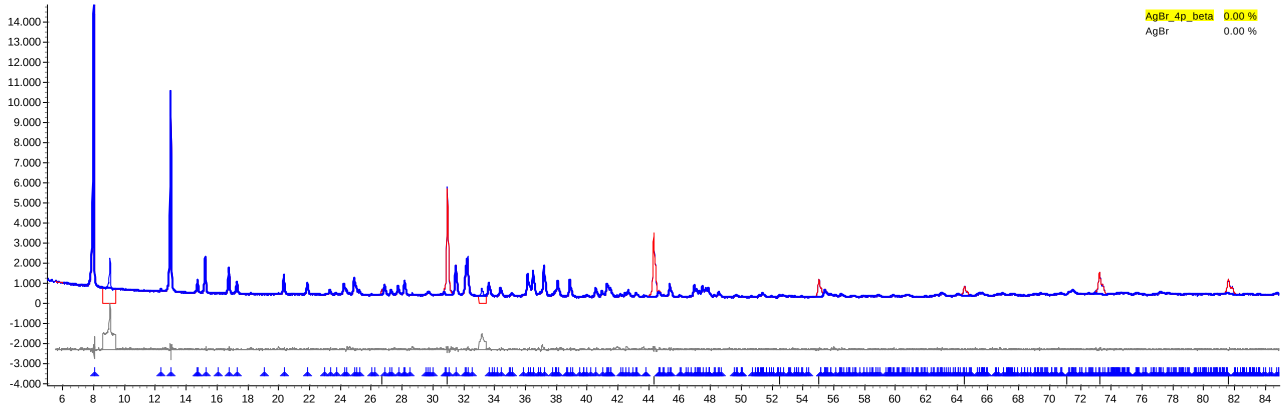

Figure 14. Pawley refinement of the [(AgBr)$_2$(4pica)]$_n$ structure. The blue line represents the [(AgBr)$_2$(4pica)]$_n$ phase, while the red line the unreacted AgBr (2θ range= 3-85°)

Photophysical characterization

Measurements were performed on uncrushed powder samples placed inside two quartz slides. Reflectance spectra were acquired with a PerkinElmer Lambda 950 UV/Vis/NIR spectrophotometer equipped with a 100 mm integrating sphere and converted in absorption spectra using the Kubelka–Munk function.[21]

Steady-state emission and excitation spectra were collected in front-face mode with an Edinburgh FLS920 fluorimeter equipped with a Peltier-cooled Hamamatsu R928 PMT (200–850 nm) and corrected for the wavelength dependent phototube response.

CONCLUSIONS

The mechanochemistry has proved to be a valuable method for the synthesis of coordination polymers based on silver halides and picolylamine, some of the discovered structure cannot be obtained *via* the common solution techniques.

Starting from the silver iodide we obtained three new compounds: $[AgI(2Pica)]_n$, $[AgI(3Pica)]_n$ and $[AgI(4Pica)]_n$; all three share the same type of crystal structure characterized by an 1-D infinite double chain of AgBr with the ligand that coordinates the silver only through the ammino group. Despite the presence of Ag(I) and shorts Ag-Ag distances (often associated to a emittive behaviour), no one of the new compounds present a detectable luminescence, neither any electrical conductivity ability.

The silver bromide displayed a higher versatility, showing the ability to react in different ratio with the 3pica and 4pica. The crystal structures obtained are characterized by the presence of very different arrangement of the inorganic part: $[AgBr(2Pica)]_n$ is characterized by the presence of the double chain as observed for the silver iodide compunds, while for 3pica and 4pica there were identified different structural arrangement characterized by a polymer expansion with the bridging ligand. Single chain and dimer stricture have been obtained, arrangement previously observed in complexes of CuI and 3pica; the “saddle chain” structure has also been found, this configuration possesses a strong inorganic character, with the remarkable presence of a linear wire of silver atoms.In addition, another compound based on AgBr and 4pica was synthesized, the structural resolution from powder diffraction is in progress. All the AgBr structure are luminescent, and a more detailed photophysical characterization is planned for the future, as well as an electrical conductivity characterization.In order to complete the silver halides screening with picolylamine, more experiment will be performed using AgCl as reagent.

SUPPORTING INFORMATION

Silver Iodide

The crystallographic data

Table SI1. Crystallographic data of the structures obtained with AgI and the three isomers of pica

	$[AgI(2Pica)]_n$	$[AgI(3Pica)]_n$	$[AgI(4Pica)]_n$
Chemical formula		$AgIC_6H_8N_2$	
Formula Mass		342.91	
Crystal System	Triclinic	Monoclinic	Monoclinic
a/Å	4.57940(11)	16.916(5)	4.4664(3)
b/Å	10.32350(17)	4.568(5)	19.2155(11)
c/Å	10.26317(17)	22.719(5)	10.5788(6)
α/°	112.5425(13)	90	90
β/°	83.8617(19)	90.447(5)	96.346(5)
γ/°	85.593(2)	90	90
Volume/ Å^3	441.9	1756(2)	902.353
Temperature	RT	RT	RT
Space group	P-1	$P2_1/c$	$P2_1/c$
Rwp	0.0373	0.062	0.0398

Thermal characterization

Thermogravimetric analysis (TGA)

TGA measurements were performed using a Perkin Elmer TGA7 in the temperature range 35-400°C under N^2 gas flow and heating was carried out at 5°C min^{-1}.

$[AgI(4pica)]_n$

The TGA analysis of the complex $[AgI(4Pica)]_n$ shows progressive weight loss that start from approximately at 36°C, associated to the 4pica release. The the remaining residue of 56.76% is lower that the theoretical AgBr content (68.46%) probabely due to some unreacted pica present in the initial sample.

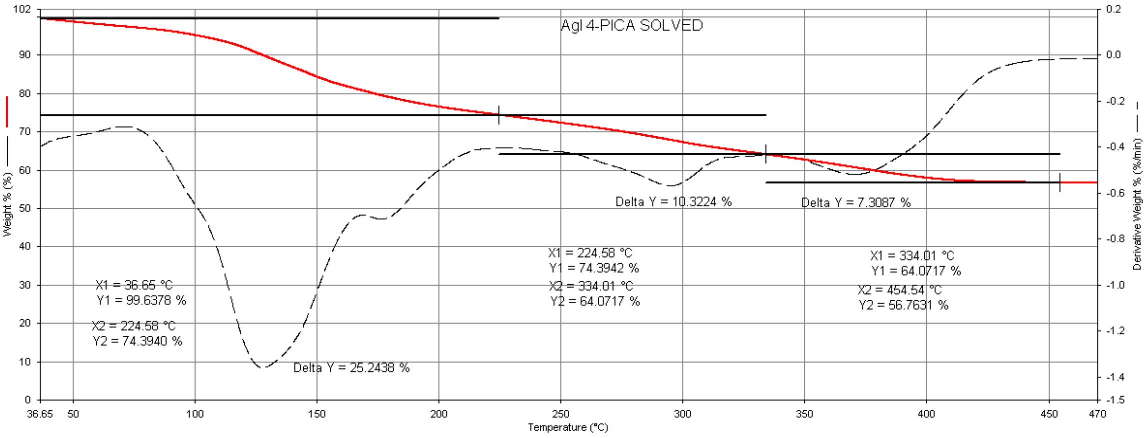

Figure SI1. TGA analysis for *[AgI(2pica)]*$_n$, the red line represents the trend of the weight loss-%, while the black line represents the derivative weight loss.

[AgI(3pica)]$_n$

The TGA analysis of the complex [AgI(3Pica)]$_n$ shows a single step of weight loss (of 44.92%) before the The total value associated to the pica release is higher than the thoretical one (31.54%) due to an excess of unreacted pica in the sample.

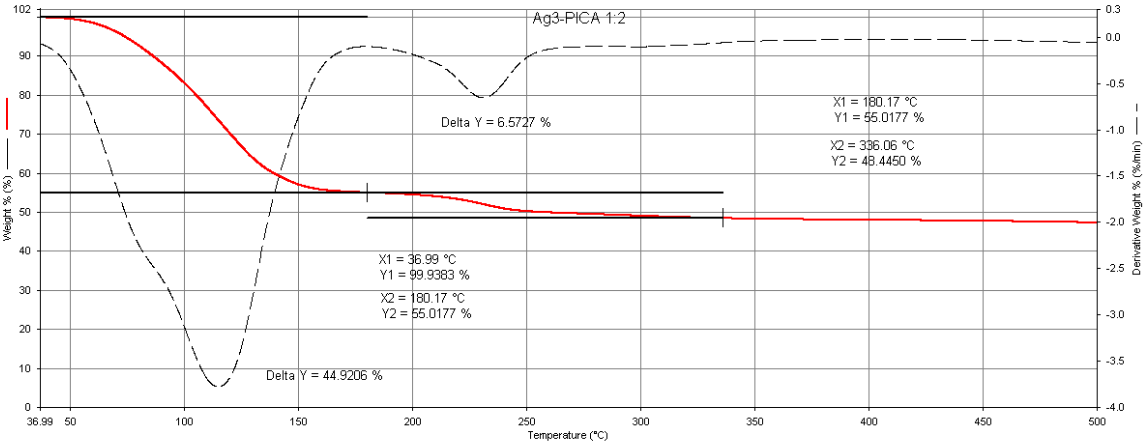

Figure SI2. TGA analysis for *[AgI(2pica)]*$_n$, the red line represents the trend of the weight loss-%, while the black line represents the derivative weight loss.

[AgI(2pica)]$_n$

The TGA analysis of the complex [AgI(2Pica)]n shows a first step of weight loss, of 31.2%, followed by a progressive second small step, which corresponds to the release of one ligand molecule. The residue of 60.05%, corresponding to the AgBr, is lower than the thoretical value (68.46%) probabely due to the presence of unreacted pica in the sample.

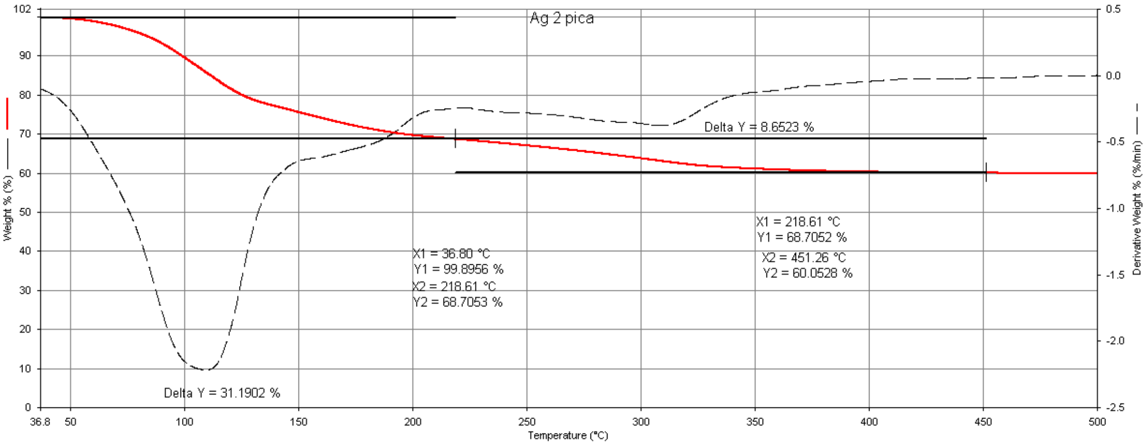

Figure SI3. TGA analysis for *[AgI(2pica)]ₙ*, the red line represents the trend of the weight loss-%, while the black line represents the derivative weight loss.

Silver Bromide

The crystallographic data

Table SI2. Crystallographic data of the structures obtained with AgBr and the three isomers of pica.

	$[(AgBr)(2pica)]_n$	$[(AgBr)(3pica)]_n$	$[(AgBr)_2(3pica)]_n$	$[(AgBr)(4pica)]_n$	$[(AgBr)_2(4pica)]_n$
Chemical formula	$AgBrC_6H_8N_2$	$AgBrC_6H_8N_2$	$Ag_2Br_2C_6H_8N_2$	$AgBrC_6H_8N_2$	$Ag_2Br_2C_6H_8N_2$
Formula Mass	295.92 g/mol	295.92 g/mol	483.69 g/mol	295.92 g/mol	483.69 g/mol
Crystal System	Triclinic	Monoclinic	Moniclinic	Monoclinic	Orthorombic
a/Å	4.3871(5)	9.4518(6)	14.305(1)	6.296(1)	14.276(3)
b/Å	10.1081(12)	6.1880(3)	6.2851(5)	7.3478(13)	6.622(1)
c/Å	10.2510(18)	14.3981(9)	23.633(2)	17.763(4)	22.997(5)
α/°	113.498(14)	90	90	90	90
β/°	97.081(12)	105.712(6)	103.488(9)	80.954(19)	90
γ/°	93.535(9)	90	90	90	90
Volume/ Å3	410.629	810.647	2066.2	811.578	2079.679
Temperature	RT	RT	RT	RT	RT
Space group	P-1	$P2_1/c$	I2/a	$P2_1$	$C222_1$
R_1	0.048	0.045	0.073	0.163	/
R_{wp}	/	/	/	/	0.0498

Thermal characterization

Thermogravimetric analysis (TGA)

TGA measurements were performed using a Perkin Elmer TGA7 in the temperature range 35-400°C under N^2 gas flow and heating was carried out at 5°C min^{-1}.

Differential scanning calorimetry (DSC)

The analisys was performed with an instrument Perkin-Elmer PyrisDiamond DSC, in N_2 atmosphere and a scanning speed of 5°/min.

[AgBr(2pica)]$_n$

From the TGA analysis we observed that the 2pica release happens in two different steps. The first loss takes place around 50°C and the second at 104°C. Due to the complex multi-step weight loss mechanism it was also performed a DSC to observed possibly solid-state transition, due to the partial pica release, in new metastable phase with a different AgBr:pica ratio. From the DSC (figure SI) it obeserved that the first pica loss is concomitant to the melting point (at 64.25°C), this behaviour is peculiar since coordination polymers usuallt tend to degradate before the melting, whereas in this case the melting take place at relative low temperature, before the complete ligand loss.

Around 120°C the second step starts, and the remaining ligand is released, leaving a residue attributable to the pure AgBr. The presence of AgBr and ligand in the ratio 1:1 was confirmed by weight% calculations (AgBr weight% theoretical= 63.45%, observed= 67.08%), with minor differences due to some unreacted AgBr.

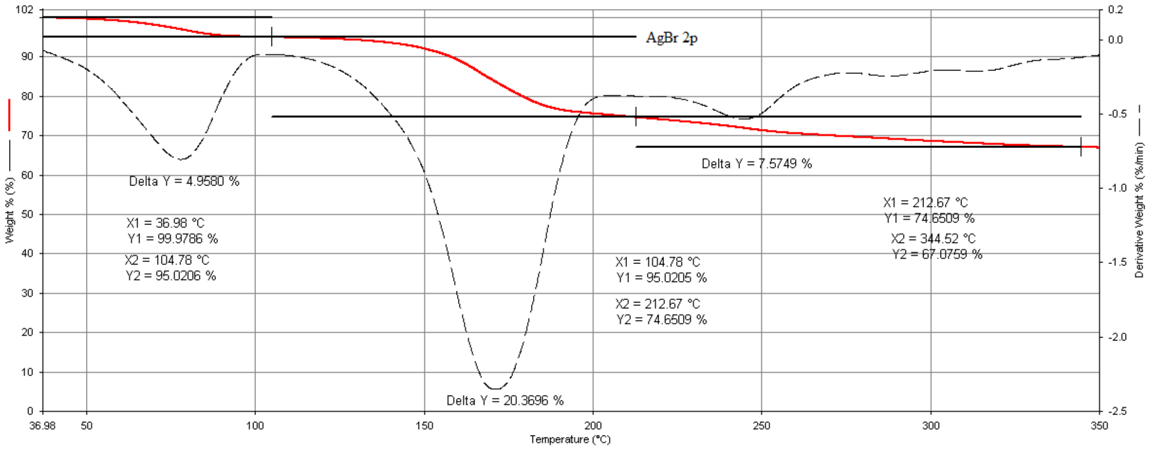

Figure SI4. TGA analysis for *[AgBr(2pica)]$_n$*, the red line represents the trend of the weight loss-%, while the black line represents the derivative weight loss.

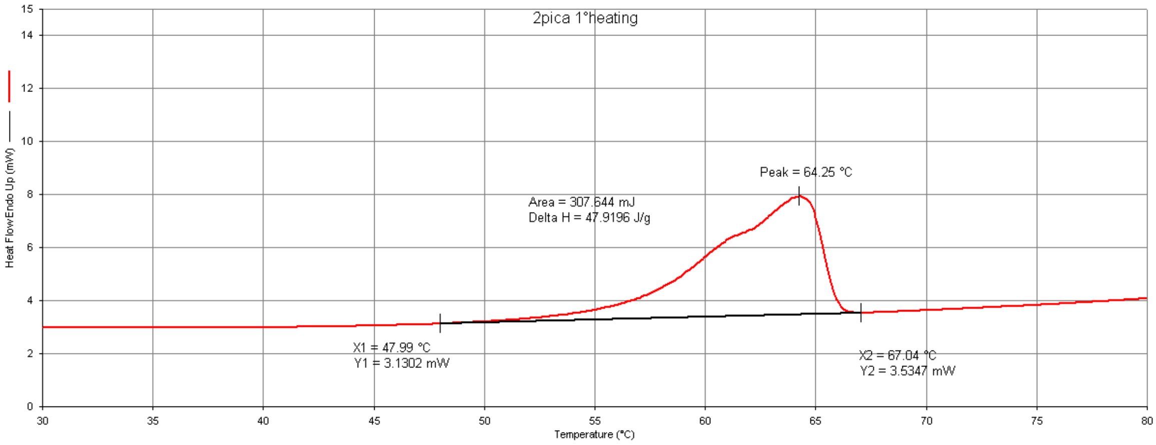

Figure SI5. DSC analysis for *[AgBr(2pica)]$_n$*, is visible the double maximun in the peak, due to the presence of the melting event and the pica release.

[AgBr(3pica)]$_n$

The TGA curve shows a progressive ligand loss, in a complex three-steps mechanism. It starts around 37°C and finished at 250°C, with a residue of 62.23 weight%, consistent with the contained AgBr (weight% theoretical=63.45%). As in the previous case a DSC has been performed and it was discovered that the first ligand loss is associated with the melting point (figure SI).

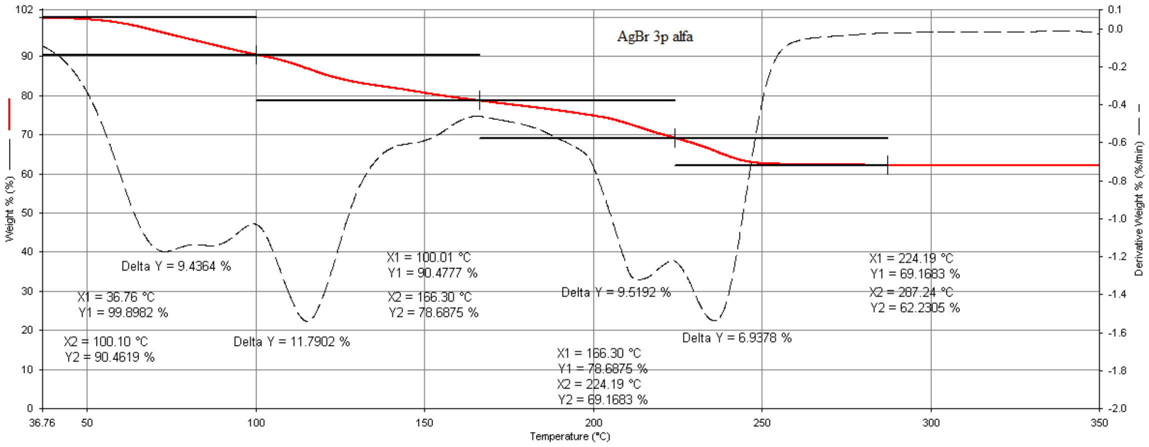

Figure SI6. TGA analysis for *[AgBr(3pica)]ₙ*, the red line represents the trend of the weight loss-%, while the black line represents the derivative weight loss.

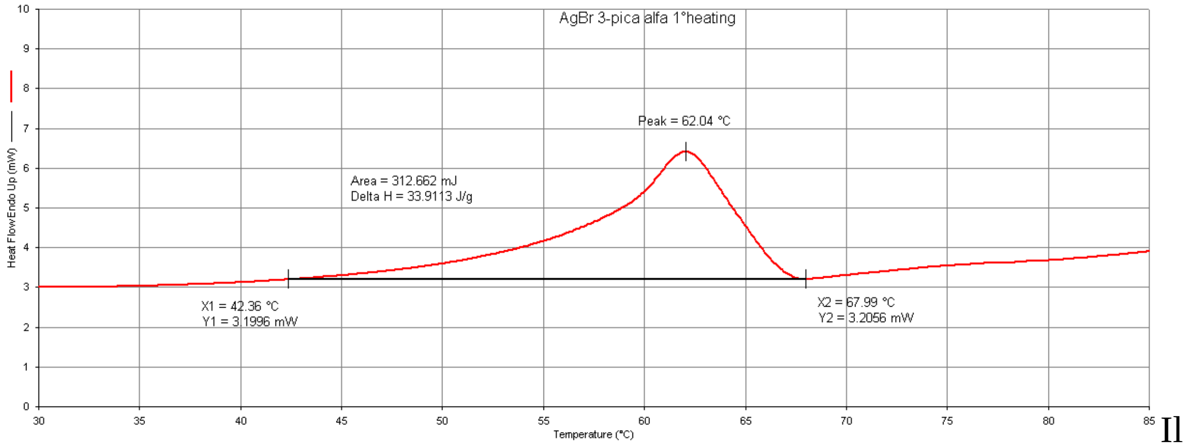

Figure SI7. DSC analysis for *[AgBr(3pica)]ₙ*, the broad peaks is due to the overlap of the fusion peak and the pica release peak.

[(AgBr)₂(3pica)]ₙ

The TGA shows a weight loss in two distinctive and resoolved steps, the first starts around 51°C while the second at 147°C. The residue is the 78.55% weight%, consistent with the contained AgBr (weight% theoretical=77.64%). From the DSC can be noticed that the melting point occurs around 106°C, during the first pica release step (figure SI19).

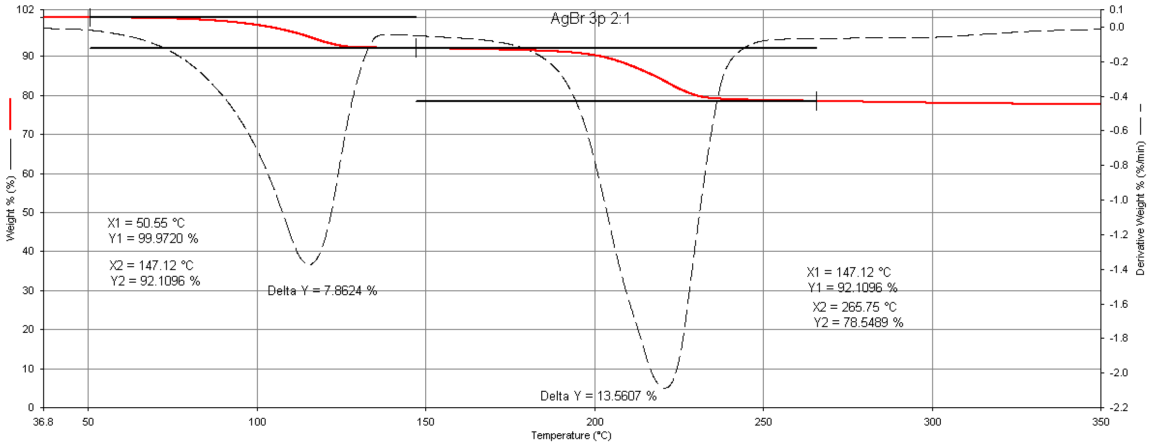

Figure SI8. TGA analysis for *[(AgBr)$_2$(2pica)]$_n$*, the red line represents the trend of the weight loss-%, while the black line represents the derivative weight loss.

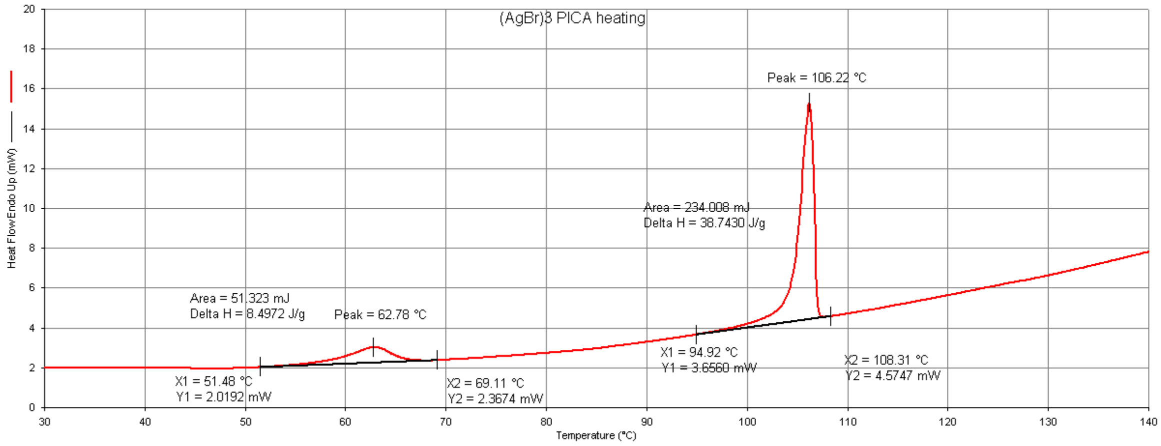

Figure SI9. DSC analysis for *[(AgBr)$_2$(3pica)]$_n$*, the first peak at 62.78°C is probably due to an impurity in the sample, the second peak represents to the melting point.

[AgBr(4pica)]$_n$

The TGA shows only one step of weight loss, compatible with the release of the contained 4pica. In respect to the compounds with 2pica and 3pica, the loss starts at higher temperature. The initial pica release is concomitant to the melting point, that occurs at 104°C (figure SI).

The residual part corresponding to 70.14 weight% and corresponding to the AgBr; the value is higher than the theoretical content (63.45%) due to the presence of some unreacted AgBr in the sample.

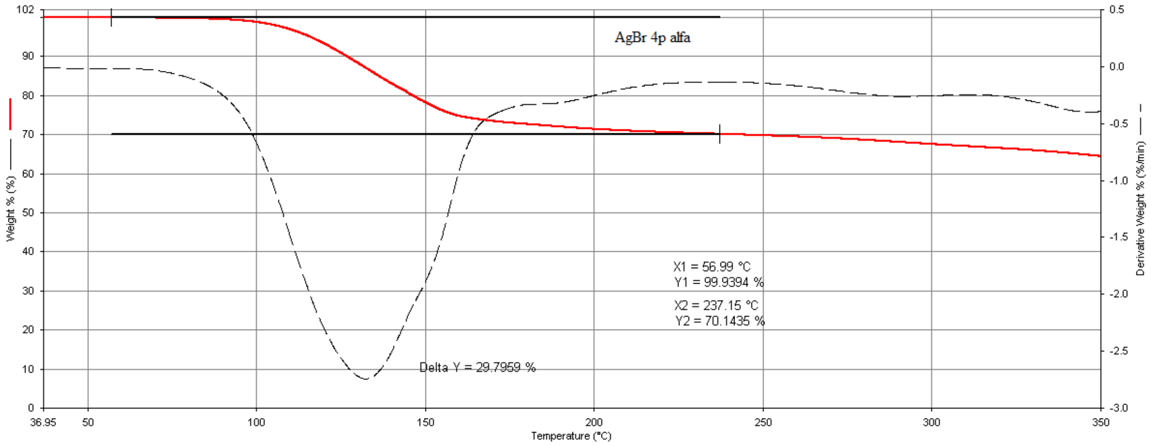

Figure SI10. TGA analysis for *[AgBr(4pica)]$_n$*, the red line represents the trend of the weight loss-%, while the black line represents the derivative weight loss.

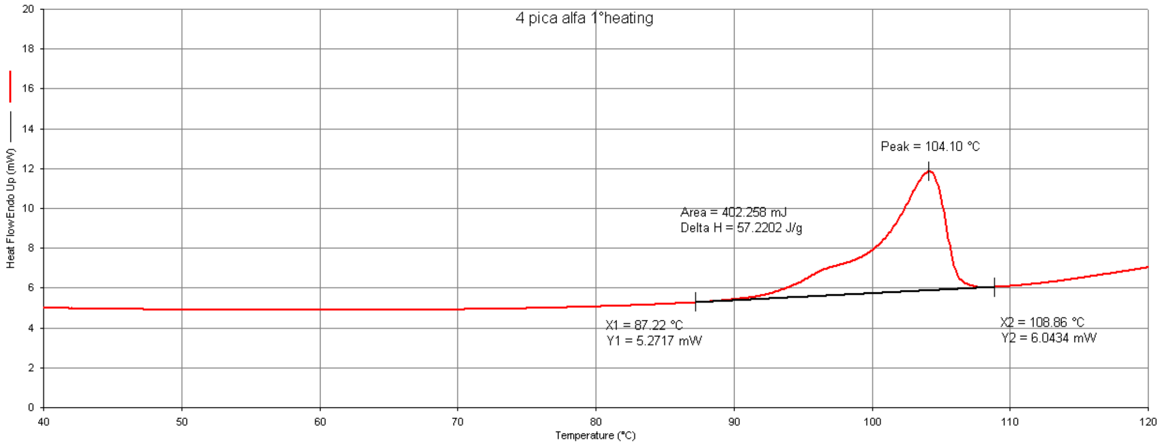

Figure SI11. DSC analysis for *[AgBr(4pica)]$_n$*, is visible the double maximun in the peak, due to the presence of the melting event and the pica release.

[(AgBr)$_2$(4pica)]

Similar to the previous case, the weight loss occurs in one step that starts around 55°C and finished at 190°C, and it is compatible with the release of the contained 4pica; the ligand release is concomitant to the melting point (102.8°C), as can be seen in the DSC curve (figure SI).

The residual weight% is consistent with the AgBr content (AgBr weight% theoretical= 77.64%, observed= 79.18%), with minor differences due to some unreacted AgBr.

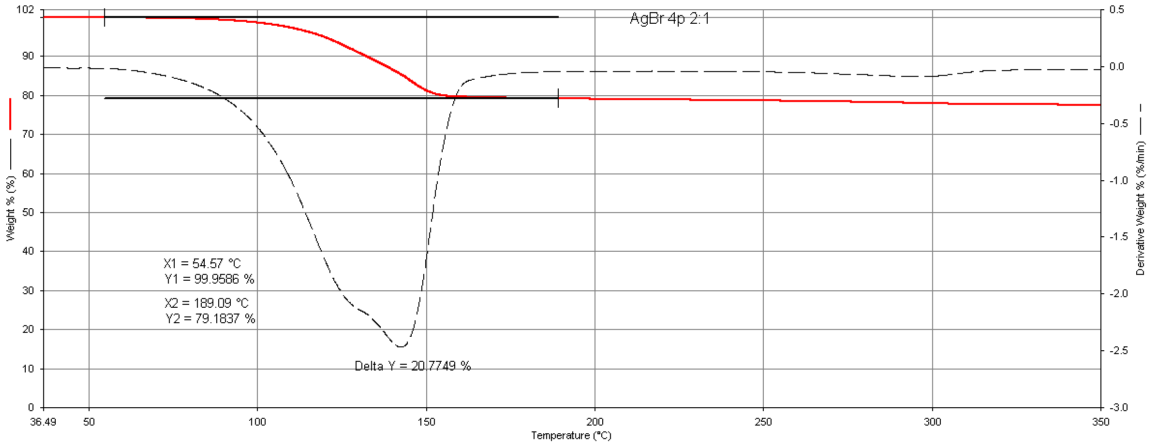

Figure SI12. TGA analysis for *$[(AgBr)_2(4pica)]$*, the red line represents the trend of the weight loss-%, while the black line represents the derivative weight loss.

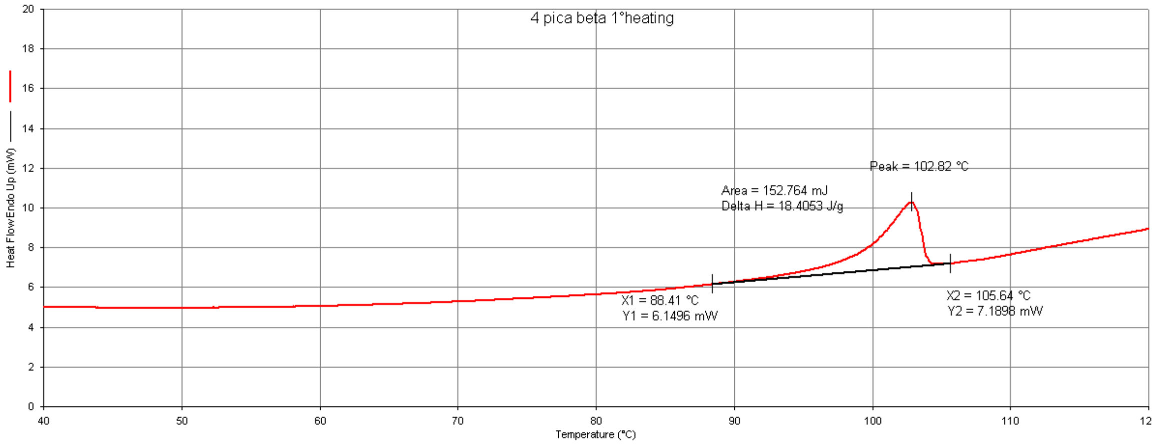

Figure SI13. DSC analysis for *$[(AgBr)_2(4pica)]$*, the broad peaks is due to the overlap of the fusion peak and the pica release peak.

REFERENCES

(1) Cariati, E.; Lucenti, E.; Botta, C.; Giovanella, U.; Marinotto, D.; Righetto, S. Cu(I) Hybrid Inorganic-Organic Materials with Intriguing Stimuli Responsive and Optoelectronic Properties. *Coordination Chemistry Reviews*. Elsevier, **2016**, pp 566–614.

(2) Janiak, C. Engineering Coordination Polymers towards Applications. *Dalt. Trans.* **2003**, *0* (14), 2781–2804.

(3) Batten, S. R.; Champness, N. R.; Chen, X.-M.; Garcia-Martinez, J.; Kitagawa, S.; Öhrström, L.; O'keeffe, M.; Suh, M. P.; Reedijk, J. Terminology of Metal-Organic Frameworks and Coordination Polymers (IUPAC Recommendations 2013). *Pure Appl. Chem* **2013**, *85* (8), 1715–1724.

(4) Wang, G.-E.; Xu, G.; Wang, M.-S.; Sun, J.; Xu, Z.-N.; Guo, G.-C.; Huang, J.-S. A Novel Inorganic–organic Hybrid for Detection of Nitrite Anions with Extremely High Sensitivity and Selectivity. *J. Mater. Chem.*

2012, *22* (33), 16742.

(5) Li, H. H.; Chen, Z. R.; Cheng, L. C.; Feng, M.; Zheng, H. D.; Li, J. Q. Three Silver Iodides with Zero and One-Dimensional Hybrid Structures Directed by Conjugated Organic Templates: Synthesis and Theoretical Study. *Dalt. Trans* **2009**, No. 25, 4888–4895.

(6) Chen, A.; Meng, S.; Zhang, J.; Zhang, C. Two Interesting Tetranuclear Ag(I) Complexes Based on Dipyrido[3,2-f:2,3-h] -Quinoxaline: Synthesis, Structural, Luminescence and Theoretical Studies. *Inorg. Chem. Commun.* **2013**, *35*, 276–280.

(7) Kagan, C. R.; Mitzi, D. B.; Dimitrakopoulos, C. D. Organic-Inorganic Hybrid Materials as Semiconducting Channels in Thin-Film Field-Effect Transistors. *Science* **1999**, *286* (5441), 945–947.

(8) Liu, G.; Liu, L.; Chu, Y.; Sun, Y. Different Contributions of Aliphatic and Conjugated Organic Cations to Both the Crystal and Electronic Structures : Three Hybrid Iodoargentates Showing Two Isomers of the $(AgI_2)^-$ Chain. *Eur J. Inorg. Chem*. **2015**, 478–487.

(9) Meijboom, R.; Bowen, R. J.; Berners-Price, S. J. Coordination Complexes of Silver(I) with Tertiary Phosphine and Related Ligands. *Coordination Chemistry Reviews*. Elsevier, **2009**, pp 325–342.

(10) Zhang, R.-C.; Wang, J.-J.; Zhang, J.-C.; Wang, M.-Q.; Sun, M.; Ding, F.; Zhang, D.-J.; An, Y.-L. Coordination-Induced Syntheses of Two Hybrid Framework Iodides: A Thermochromic Luminescent Thermometer. *Inorg. Chem* **2016**, *55*, 47.

(11) Shen, J.; Zhang, C.; Yu, T.; An, L.; Fu, Y. Structural and Functional Modulation of Five 4-Cyanopyridinium Iodoargentates Built up from Cubane-like Ag_4I_4 Nodes. *Cryst. Growth Des.* **2014**, *14* (12), 6337–6342.

(12) Yu, T.; An, L.; Zhang, L.; Shen, J.; Fu, Y.; Fu, Y. Two Thermochromic Layered Iodoargentate Hybrids Directed by 4-and 3-Cyanopyridinium Cations. *Cryst. Growth Des.* **2014**, *14*, 3875-3879.

(13) Wang, S.; Mitzi, D. B.; Feild, C. A.; Guloys, A. Synthesis and Characterization of $[NH_2C(I)=NH_2]_3MI_5$ (M = Sn, Pb): Stereochemical Activity in Divalent Tin and Lead Halides Containing Single (110) Perovskite Sheets. *J. Am. Chem. SOC* **1995**, *117*, 5297–5302.

(14) Schmidbaur, H.; Schier, A. Argentophilic Interactions. *Angewandte Chemie - International Edition*. Wiley-Blackwell, **2015**, pp 746–784.

(15) Zhang, R. C.; Zhang, Y. J.; Yuan, B. Q.; Miao, J. P.; Pei, B. H.; Liu, P. P.; Wang, J. J.; Zhang, D. J. Transformation of Dense AgI into a Silver-Rich Framework Iodide Using Thiophenol as Mineralizer. *J. Solid State Chem.* **2014**, *220*, 185–190.

(16) Farinella, F.; Maini, L.; Mazzeo, P. P.; Fattori, V.; Monti, F.; Braga, D. White Luminescence Achieved by a Multiple Thermochromic Emission in a Hybrid Organic-Inorganic Compound Based on 3-Picolylamine and Copper(I) Iodide. *Dalt. Trans.* **2016**, *45*, 17939–17947.

(17) Mills, N. K.; White, A. H. Lewis-Base Adducts of Group 1B Metal(I) Compounds. Part 4. Synthesis and Crystal Structure of the 1 : 1 Adduct of Silver(I) Chloride with Quinoline. *J. Chem. Soc. Dalt. Trans.* **1984**, *0* (2), 225.

(18) Meijboom, R.; Bowen, R. J.; Berners-Price, S. J. Coordination Complexes of Silver(I) with Tertiary Phosphine and Related Ligands. *Coordination Chemistry Reviews*. **2009**, pp 325–342.

(19) Mitsumi, M. Crystal Structures and Properties of MMX-Chain Compounds Based on Dithiocarboxylato-Bridged Dinuclear Complexes. *Material Designs and New Physical Properties in MX- and MMX-Chain Compounds*; Springer Vienna: Vienna, **2013**; pp 151–205.

(20) Hassanein, K.; Conesa-Egea, J.; Delgado, S.; Castillo, O.; Benmansour, S.; Martínez, J. I.; Abellán, G.; Gõmez-García, C. J.; Zamora, F.; Amo-Ochoa, P. Electrical Conductivity and Strong Luminescence in Copper Iodide Double Chains with Isonicotinato Derivatives. *Chem. - A Eur. J.* **2015**, *21* (48), 17282–17292.

(21) Herbst-Irmer, R.; Sheldrick, G. M. Refinement of Twinned Structures with SHELXL97. *Acta Crystallogr. B* **1998**, *54* (4), 443–449.

(22) Sheldrick, G. M. SHELXT - Integrated Space-Group and Crystal-Structure Determination. *Acta Crystallogr. Sect. A Found. Crystallogr.* **2015**, *71* (1), 3–8.

(23) Coelho, A. A. *TOPAS* and *TOPAS-Academic* : An Optimization Program Integrating Computer Algebra and Crystallographic Objects Written in C++. *J. Appl. Crystallogr.* **2018**, *51* (1), 210–218.

(24) Gates, B. C.; Knözinger, H.; Jentoft, F. C. *Advances in Catalysis Vol. 52*; Academic Press, **2009**.

AKNOWLEDGMENTS

First of all I would like to thanks my awesome supervisor, prof. Lucia Maini, that with great patience led me during the PhD, teaching and, mostly, correcting my mistakes. I was very lucky to have the possibility to work with a scientist (but also a woman) like her.

I certanly would like to express my gratitude to all the Molecular Crystal Engineering group, the ones who are currently part of the group but also the people that were part of the group and now are following new paths.

I should like to express my warmest and sincerest gratitude to prof. Tsunehisa Kimura and his wife Dr. Fumiko Kimura, and also all the Fibrous Biomaterials group, that welcomed me in Kyoto and gave to me the opportunity to spend four incredible months in their laboratory. My Japan stay was certanly one of the most wonderfull experience in my entire life that made me to grow up as a scientist and as a person.

A big thanks goes also to Dr. Manuela Melucci and all the other people from CNR with whom I have worked, for the possibility of exchanging knowledges and expertises, learning always something new.

Finally I can't forget my family, specially my father, for the endless supporting and my boyfriend, we started togheter our academic journey achieving this goal thanks to the reciprocal encouragement.